GHASP : An Halpha kinematic survey of spiral and irregular galaxies - VI. New Halpha data cubes for 108 galaxies

B. Epinat, P. Amram, M. Marcelin, C. Balkowski, O. Daigle, O. Hernandez, L. Chemin, C. Carignan, J. -L. Gach, P. Balard

GHASP: an Hα kinematic survey of spiral and irregular galaxies – VI. New Hα data cubes for 108 galaxies

B. Epinat,[1]★ P. Amram,[1] M. Marcelin,[1] C. Balkowski,[2] O. Daigle,[1,3] O. Hernandez,[1,3] L. Chemin,[2] C. Carignan,[3] J.-L. Gach[1] and P. Balard[1]

[1]*Laboratoire d'Astrophysique de Marseille, OAMP, Université de Provence & CNRS, 38 rue F. Joliot - Curie, 13388 Marseille, Cedex 13, France*
[2]*GEPI, Observatoire de Paris-Meudon, Université Paris VII, 5 Place Jules Janssen, 92195 Meudon, France*
[3]*LAE et Observatoire du mont Mégantic, Université de Montréal, C. P. 6128 succ. centre ville, Montréal, Québec, Canada H3C 3J7*

ABSTRACT

We present the Fabry–Perot observations obtained for a new set of 108 galaxies in the frame of the Gassendi Hα survey of SPirals (GHASP). The GHASP survey consists of 3D Hα data cubes for 203 spiral and irregular galaxies, covering a large range in morphological types and absolute magnitudes, for kinematics analysis. The new set of data presented here completes the survey. The GHASP sample is by now the largest sample of Fabry–Perot data ever published. The analysis of the whole GHASP sample will be done in forthcoming papers. Using adaptive binning techniques based on Voronoi tessellations, we have derived Hα data cubes from which are computed Hα maps, radial velocity fields as well as residual velocity fields, position–velocity diagrams, rotation curves and the kinematical parameters for almost all galaxies. Original improvements in the determination of the kinematical parameters, rotation curves and their uncertainties have been implemented in the reduction procedure. This new method is based on the whole 2D velocity field and on the power spectrum of the residual velocity field rather than the classical method using successive crowns in the velocity field. Among the results, we point out that morphological position angles have systematically higher uncertainties than kinematical ones, especially for galaxies with low inclination. The morphological inclination of galaxies having no robust determination of their morphological position angle cannot be constrained correctly. Galaxies with high inclination show a better agreement between their kinematical inclination and their morphological inclination computed assuming a thin disc. The consistency of the velocity amplitude of our rotation curves has been checked using the Tully–Fisher relationship. Our data are in good agreement with previous determinations found in the literature. Nevertheless, galaxies with low inclination have statistically higher velocities than expected and fast rotators are less luminous than expected.

Key words: galaxies: dwarf – galaxies: irregular – galaxies: kinematics and dynamics – galaxies: spiral.

1 INTRODUCTION

As it is nowadays largely admitted, 2D velocity fields allow the computation of 1D rotation curves in a more robust way than long-slit spectrography. Indeed, first of all, the spatial coverage is larger and moreover, the kinematical parameters are determined a posteriori instead of a priori in long-slit spectrography. In that context, we have undertaken the kinematical 3D Gassendi Hα survey of SPirals

(GHASP). The GHASP survey consists of a sample of 203 spiral and irregular galaxies, mostly located in nearby low density environments, observed with a scanning Fabry–Perot for studying their kinematical and dynamical properties through the ionized hydrogen component.

Studying the links between parameters reflecting the dynamical state of a galaxy will help us to have a better understanding of the evolution of galaxies. This sample has been constituted in order:

(i) to compute the local Tully–Fisher relation;
(ii) to compare the kinematics of galaxies in different environments (field, pairs, compact groups, galaxies in cluster) for

discriminating secular evolution from an external origin (e.g. Garrido et al. 2005);

(iii) to study the distribution of luminous and dark halo components along the Hubble sequence for high and low surface brightness galaxies, for a wide range of luminosities in combining the optical data with the radio ones (e.g. Barnes, Sellwood & Kosowsky 2004; Spano et al. 2008);

(iv) to model the effect of non-axisymmetric structures like bars, spiral arms, oval distortions, lopsidedness in the mass distribution using both *N*-body and hydrodynamic numerical simulations (e.g. Hernandez et al., in preparation), kinematic analysis (e.g. Krajnović et al. 2006) and the Tremaine–Weinberg method to measure the bar, spiral and inner structure pattern speeds (Hernandez et al. 2005a);

(v) to analyse the gaseous velocity dispersion and to link it with the stellar one;

(vi) to create template rotation curves (e.g. Persic & Salucci 1991; Persic, Salucci & Stel 1996; Catinella, Giovanelli & Haynes 2006) and template velocity fields;

(vii) to map the 2D mass distribution using 2D velocity field, broad-band imagery and spectrophotometric evolutionary models;

(viii) to search for links between the kinematics (shape of rotation curves, angular momentum, etc.) and the other physical properties of galaxies like star formation rate (e.g. comparison with star-forming galaxies like blue compact galaxies, etc.); and

(ix) to produce a reference sample of nearby galaxies to compare to the kinematics of high-redshift galaxies (Puech et al. 2006; Epinat, Amram & Balkowski 2007). Indeed, it is necessary to disentangle the effects of galaxy evolution from spatial (beam smearing) and spectral resolution effects.

This paper is the sixth of a series called hereafter Paper I–V (Garrido et al. 2002, 2003; Garrido, Marcelin & Amram 2004; Garrido et al. 2005; Spano et al. 2008) presenting the data obtained in the frame of the GHASP survey. The data gathered with the seven first observing runs have been published from Paper I to IV. Dark matter distribution in a subsample of 36 spiral galaxies has been presented in Paper V. This paper presents the last unpublished 101 Hα data cubes of the GHASP survey. It includes 108 galaxies (seven data cubes contain two galaxies), providing 106 velocity fields and 93 rotation curves resulting from observational runs eight to fourteen. This represents the largest set of galaxies observed with Fabry–Perot techniques ever published in the same paper (Schommer et al. 1993 sample consists of 75 cluster galaxies in the Southern hemisphere observed with Fabry–Perot techniques and was the largest sample published to date). Including the previous papers (Paper I–IV), the GHASP survey totalizes Fabry–Perot data for 203 galaxies observed from 1998 to 2004. The GHASP sample is by now the largest sample of Fabry–Perot data ever published.

In Section 2, the selection criteria of the GHASP sample, the instrumental set-up of the instrument and the data reduction procedure are described. In Section 3, different momenta of the data cubes are presented as well as the new method to build the rotation curves and to determine the uncertainties. An analysis of the residual velocity fields and of the kinematical parameters is thus given. In Section 4, the Tully–Fisher relation is plotted for the GHASP galaxies presented in this paper. In Section 5, we give the summary and conclusions. In Appendix A, we present some details on the method used to compute the rotation curves. In Appendix B, the comments for each individual galaxy are given. In Appendix C, the different tables are given, while in Appendix D the individual maps and position–velocity diagrams are shown. The rotation curves are finally displayed in Appendix E, while the numerical tables corresponding to the rotation curves are given in Appendix F.

When the distances of the galaxies are not known, a Hubble constant $H_0 = 75 \, \text{km s}^{-1} \, \text{Mpc}^{-1}$ is used throughout this paper.

2 OBSERVATIONS AND DATA REDUCTION

2.1 The GHASP sample

The GHASP survey was originally selected to be a subsample complementing the radio survey Westerbork survey of H I in SPirals galaxies (WHISP) providing H I distribution and velocity maps for about 400 galaxies (http://www.astro.rug.nl/ whisp). The first set of GHASP galaxies was selected from the first WHISP website list but some of them have never been observed by WHISP. Thus, only 130 galaxies have finally been observed in both surveys. The comparison between the kinematics of neutral and ionized gas coming from the GHASP and the WHISP data sets is possible for a subsample of 31 dwarf galaxies studied by Swaters et al. (2002) and for another subsample of 19 early-type galaxies analysed by Noordermeer et al. (2005), the remaining part of the WHISP sample being yet unpublished but most of the H I maps are nevertheless available in the WHISP website.

Most of the GHASP targets were chosen in nearby low-density environments. Nevertheless, some galaxies in pairs or in low density groups have been observed mainly when they were selected by WHISP (see individual comments in Appendix B). Seven galaxies of the GHASP sample are located in nearby clusters (UGC 1437 in the cluster Abell 262, UGC 4422 and 4456 in the Cancer cluster, UGC 6702 in the cluster Abell 1367, UGC 7021, 7901 and 7985 in the Virgo cluster). More Virgo cluster galaxies observed with the same instrument have been published elsewhere (Chemin et al. 2006).

Fig. 1 displays the distribution of the whole GHASP survey in the magnitude–morphological type plane. We have found in the literature measurements for both M_B and Hubble type for 198 galaxies (out of 203 galaxies). Among the sample of 203 galaxies, 83 are strongly barred galaxies (SB or IB) and 53 are moderately barred galaxies (SAB or IAB). The GHASP sample provides a wide coverage in galaxy luminosities ($-16 \le M_B \le -22$), thus in galaxy masses from (10^9 to $5 \times 10^{11} \, \text{M}_\odot$) and in morphological types (from Sa to Irregular). The well-known relation for spiral and irregular galaxies between the morphological type and the absolute magnitude is observed through the GHASP sample. Within the dispersion of this relation, the 203 GHASP galaxies are reasonably distributed through the plane down to low-magnitude (≥ -16) and to early-type spirals (≤ 0, Sa). The whole GHASP data set of galaxies is reasonably representative of the LEDA sample (see Paper IV).

The journal of the observations for the 107 new galaxies is given in Table C1. The 108th galaxy, UGC 11300 has been observed for the third time in order to check the consistency of the new data reduction method (the second observation published in Paper IV was already done in order to compare the new GaAs camera with the 'S20' photocathode). Note that the right ascension and the declination given in Table C1 are the coordinates of the kinematical centre (and not the morphological ones given in HyperLeda or in LEDA, except if stated otherwise).

2.2 The instrumental set-up

In order to map the flux distribution and the velocity fields of the sample of galaxies, high spectral resolution 3D data cubes in the Hα
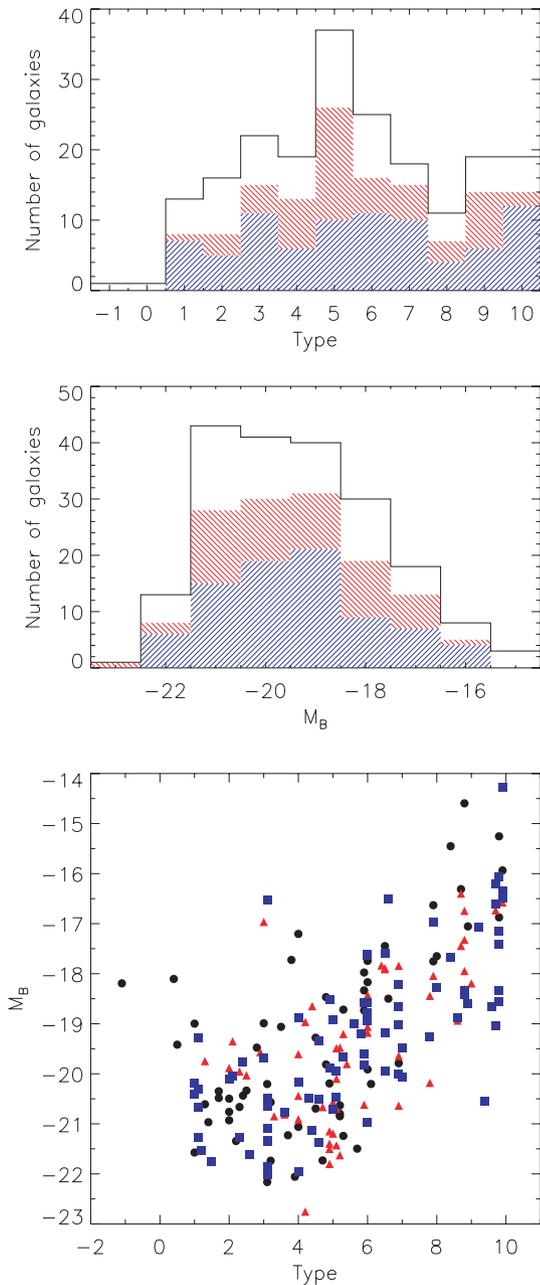
Figure 1. Top panel: distribution of morphological type for almost all of the GHASP sample (201 out of 203 galaxies). Middle panel: distribution of the absolute *B*-band magnitude for almost all of the GHASP sample (198 out of 203 galaxies). For both the top and middle panels: the blue hash, red hash and residual white represent, respectively, the strongly barred, the moderately barred and the non-barred galaxies. Bottom panel: distribution for almost all of the GHASP sample (198 out of 203 galaxies) in the 'magnitude–morphological type' plane distinguishing strongly barred (blue squares), moderately barred (red triangles) and unbarred galaxies (black circles).

line have been obtained. This has been achieved using a focal re-ducer containing the scanning Fabry–Perot interferometer attached at the Cassegrain focus of the 1.93-m OHP telescope (Observatoire de Haute Provence). The instrument principles and characteristics are the same as for Papers I–V. The detector, a new generation im-age photon counting system (IPCS), is the same as the one used in Paper IV (with a GaAs photocathode). The pixel size is 0.68 arcsec

(however, the angular resolution of our data is limited by the see-ing, about $\sim$3 arcsec e.g. Table C1), the field-of-view is 5.8 arcmin^2 and the velocity sampling is $\sim$5 km s^{-1} (for a resolution of $\sim$10 km s^{-1}).

2.3 The data reduction

The Fabry–Perot technique provides an Hα profile inside each pixel, so that a typical velocity field of a GHASP galaxy contains thou-sands of velocity points. For most of the galaxies observed with GHASP, the velocity field is not limited to the H II regions but cov-ers most of the diffuse emission of the disc, as can be seen in the figures. The detection limit of our device is about 10^{-18} erg cm^{-2} s^{-1} arcsec^{-2}, with a signal-to-noise ratio between 1 and 2 for a typical 2 h exposure time according to fig. 2 of Gach et al. (2002). This insures a good detection of the Hα diffuse emission of the disc for most of the galaxies since most of the Hα emission found below 1.6 10^{-16} erg cm^{-2} s^{-1} arcsec^{-2} may be considered as filamen-tary and/or diffuse according to Ferguson et al. (1996). The way to derive the different moment maps of the 3D data cube (Hα line maps and Hα velocity fields) are explained in Daigle et al. (2006b) (hereafter D2006). The Hα image is a pure monochromatic image of the galaxy (continuum and [N II] free).

In a few cases, when the velocity amplitude is comparable to or higher than the width of the interference filter, its transmission is not necessarily centred on the systemic velocity and one side of the galaxy may be better transmitted than the other side, leading to an artificial asymmetry in the intensity of the Hα emission (see Paper IV for additional explanations as well as in individual com-ments on each galaxy in Appendix B).

The data processing and the measurements of the kinematical parameters are different from those used in Paper I–V. The data processing used in this paper is basically the same as the one de-scribed by D2006. One of the main improvements implemented in this data processing is the use of adaptive spatial binning, based on the 2D Voronoi tessellations method applied to the 3D data cubes, allowing to optimize the spatial resolution to the signal-to-noise ratio. Let us also mention that when enough stars or bright H II regions were available in the field-of-view, we corrected the observation from telescope drift (or instrumental flexures) when necessary. Hereafter, we just point out the main difference between the method described in D2006 and the method used in this paper.

The main difference is the criterion used to fix the size of the bins. Indeed, with the spatial adaptive binning technique, a bin is accreting new pixels until it has reached a given criterion given a priori. In D2006, the criterion is the signal-to-noise ratio of the emission line within the bin. For each bin, the noise is determined from the r.m.s of the continuum (the line free region of the whole spectrum). The signal-to-noise ratio is thus the ratio between the flux in the line and the rms in the continuum. While for the data described in D2006, the number of channels scanned is large enough (36 channels) to determine properly the noise in the continuum, this is not anymore the case here where the number of channels scanned is smaller (24 channels). For the same given spectral resolution (fixed by the interference order and the Finesse of the Fabry–Perot interferometer used), the ratio between the number of channels containing the continuum and the number of channels containing the line is thus larger (by a factor of 3/2) in D2006 than here. Furthermore, the criterion in D2006 is not relevant anymore for the GHASP data. Instead of the signal-to-noise ratio, the criterion used here is simply the square root of the flux in the line, that is an estimate of the Poisson noise in the line flux.

A second major improvement is the suppression of the ghosts due to reflection at the air–glass interfaces of the interferometer (Georgelin 1970). The reduction routine takes into account the front reflection (between the interference filter and the interferometer) and the back reflection (between the interferometer and the camera detector window). The ghosts are calibrated and then subtracted, thanks to bright stars.

Another major improvement is an automatic cleaning of the velocity fields. The outskirts of a galaxy, where there is no more diffuse Hα emission, has to be delimited. Due to residual night sky lines and background emissions (after subtraction), adaptive binning produces large sky bins with a given signal-to-noise ratio or given flux. These bins containing only sky emission are separated from the bins of the galaxy, thanks to a velocity continuity process. The velocity field is divided in several regions where the velocity difference between contiguous bins is lower than a given cut-off value. The regions with too low monochromatic flux and too large bins are erased. The given cut-off fixed a priori is about one-tenth of the total amplitude of the velocity field (let us say $30 \, \mathrm{km \, s^{-1}}$ for a velocity field with an overall amplitude of $\sim 300 \, \mathrm{km \, s^{-1}}$).

KARMA (Gooch 1996) and its routine KOORDS have been used to compute the astrometry. XDSS blue-band images or XDSS Red band images when blue image was not available are displayed (see individual captions of Figs D1–D106). Systematic comparison between these broad-band images and the field stars in high-resolution continuum images (with no adaptive binning) were made in order to find the correct World Coordinate System for each image.

3 DATA ANALYSIS

3.1 Different maps from the 3D data cube

For each galaxy, in Appendix D, from Figs D1 to D106, we present up to five frames per figure: the XDSS blue (or red) image (top left-hand panel), the Hα velocity field (top right-hand panel), the Hα monochromatic image (middle left-hand panel), eventually the Hα residual velocity field (middle right-hand panel) and finally the position–velocity diagram along the major-axis (bottom panel) when it can be computed. The white and black cross indicates the centre used for the kinematic analysis (given in Table C1 e.g. Appendix A for determination) while the black line traces the kinematical major-axis deduced from the velocity field analysis (e.g. Section 3.2) or the morphological one (taken from HyperLeda) when no position angle (PA) of the kinematical major-axis could be derived using the kinematic (e.g. Table C2). This line ends at the radius $D_{25}/2$ corresponding to the isophotal level 25 mag arcsec^{-2} in the B band (given in Table C3) in order to compare the velocity field extent with the optical disc of the galaxies. Position–velocity diagrams are computed along the axis defined by this black line, using a virtual slit width of seven pixels, and the red line in the position–velocity diagram is the rotation curve deduced from the model velocity field (see the next section) along this virtual slit. When no fit is satisfying (generally because of poor signal-to-noise ratio), we used the real velocity field instead of the model (see individual captions in Figs D1–D106). The rotation curves are found in Appendices E (figures) and F (tables). The colour version of the rotation curves in Appendix E is only available online. Rotation curves are computed and displayed following the method described in Section 3.2. These figures are also available in the website of GHASP: http://FabryPerot.oamp.fr.

In order to illustrate the printed version of the paper we have chosen to display the diversity through four galaxies having different morphological types, see Appendices D19 [UGC 3740, SAB(r)c pec], D31 [UGC 4820, S(r)ab], D45 [UGC 5786, SAB(r)b], D56 (UGC 7154, SBcd). Appendix D maps of the other galaxies are only available online.

Only the first page of Appendix F that contains the tables corresponding to the rotation curves of the two first galaxies is displayed in the printed version of the paper, the remaining part of Appendix F being available online.

3.2 Construction of the rotation curves and determination of the uncertainties

A new automatic fitting method has been developed to derive automatically a rotation curve from the 2D velocity field. This method makes the synthesis between (i) the method used in Paper I–IV, (ii) the method based on tilted-ring models found, for instance, in the ROTCUR routine of GIPSY (Begeman 1987) and (iii) the method used by Barnes & Sellwood (2003).

Warps are mainly seen in galactic discs at radii $R > R_{\mathrm{opt}}$. Tilted-ring models have been developed to model the distribution of neutral hydrogen for which warps of the H I disc may be more or less severe. In case of a warp, a monotonic change of the major-axis PA and of the inclination (i) is observed.

On the other hand, within the optical disc, the kinematic parameters PA and i do not vary significantly and change monotonically with the radius (Paper I–IV and Hernandez et al. 2005b). The variation in PA and i with the radius is more likely due to non-circular motions in the plane of the disc (e.g. bars) than to motions out of the plane (like warps) and looks like oscillations around a median value. Thus, we do not allow PA nor i to vary with the radius.

Using tilted-ring models, the errors in the parameters are the dispersion of the kinematical parameters over the rings. The method developed here uses the whole residual velocity field to estimate the dispersion induced by non-circular motions and not only the segmented information within each ring as it is the case in tilted-ring models.

Our fitting method is similar to the Barnes & Sellwood (2003) method. Two differences may nevertheless be pointed out. A minor difference is that they use a non-parametric profile, while we fit an analytic function (more details on the building of the rotation curve are given in Appendix A). The major improvement is the computation of the kinematic uncertainties. Indeed, the statistical uncertainty on the fit is unrealistically small (Barnes & Sellwood 2003), because the noise in the data is considered as a blank random noise. That is not the case because the noise in the residual velocity field is mainly due to non-circular motions (bar, oval distortions, spiral arms, local inflows and outflows, etc.) and to the intrinsic turbulence of the gas that have characteristic correlation lengths. In order to take it into account, we compute the errors with the power spectrum of the residual velocity field, applying a Monte Carlo method (see Appendix A).

Rotation curves for the barred galaxies of our sample have been plotted without correction for non-circular motions along the bar.

The rotation curves are sampled with rings. Within the transition radius (defined in Appendix A), the width of the rings is set to match half the seeing. Beyond that radius, each ring contains from 16 to 25 velocity bins.

The curves are plotted with both sides superimposed in the same quadrant, using different symbols for the receding (crosses) and approaching (dots) side (with respect to the centre). The black vertical

arrow in the *x*-axis represents the radius $D_{25}/2$ while the smaller grey arrow in the *x*-axis represents the transition radius, always smaller than $D_{25}/2$ by definition.

For galaxies seen almost edge-on (inclination higher than 75°) our model does not describe accurately the rotation of a galaxy since the thickness and the opacity of the disc cannot be neglected anymore. Indeed, on the one hand, it is well known that, due to inner galactic absorption, edge-on galaxies tend to display smoother inner velocity field and rotation curve gradients than galaxies with low or intermediate inclinations and, on the other hand, due to the actual thickness of the disc, using a simple rotation model in the plane of the galaxy disc, motion out of the disc are wrongly interpreted as circular motions in the disc. As a consequence, for most of highly inclined galaxies, the fit converges towards unrealistic low inclination values, leading to modelled velocity fields and rotation curves having too high velocity amplitudes. Thus, for NGC 542, UGC 5279, UGC 5351, UGC 7699, UGC 9219, UGC 10713 and UGC 11332, no rotation curve has been plotted. For them, the position–velocity diagram gives a more suitable information than the rotation curve and allows to follow the peak-to-peak or peak-to-valley velocity distribution along the major-axis.

3.3 Residual velocity fields

As detailed in the previous paragraph and in Appendix A, the main assumption necessary to derive a rotation curve from the observed velocity field is that rotation is dominant and that all non-circular motions are not part of a large-scale pattern. The five kinematical parameters computed from the velocity field to draw the rotation curve are determined from different symmetry properties of the radial velocity field. The influence of small errors in these parameters is to produce patterns with characteristic symmetries in the residual velocity field. This was first illustrated by Warner, Wright & Baldwin (1973) and by van der Kruit & Allen (1978). In their schematic representation of the residual motions in disc galaxies (the modelled velocity field computed from the rotation curve has been subtracted to the observed velocity field), a bad determination of one or several kinematical parameters leads to typical signatures in the residual velocity field (e.g. velocity asymmetry around the major-axis in case of a bad PA determination, etc.). The residual velocity fields plotted for each galaxy in Appendix D clearly show that these typical signatures are not seen, this means that the best determination of the kinematical parameters has been achieved.

The deviation from purely circular velocity can be large. In a forthcoming paper, these residual velocity fields will be analysed in terms of bars and oval distortions, warps, spiral arms (streaming motions), outflows and inflows, etc. (e.g. Fathi et al. 2007).

The mean velocity dispersion on each residual velocity field has been computed for each galaxy and tabulated in Table C2, they range from 4 to 54 km s^{-1} with a mean value around 13 km s^{-1}. Fig. 2 shows that the residual velocity dispersion is correlated with the maximum amplitude of the velocity field (shown by the dashed linear regression), this trend remains if we display the residual velocity dispersion versus the maximum circular velocity (not plotted). Surprisingly, barred galaxies do not have, on average, a higher mean residual velocity dispersion than unbarred galaxies (not plotted). This may be explained by the fact that the number of bins contaminated by the bar is usually rather low with respect to the total bins of the disc. Indeed, this is not the case for discs dominated by a bar. Compared to the general trend, we observe a set of about a dozen of galaxies with a high residual velocity dispersion (points above the dotted line in Fig. 2). These points correspond to galaxies
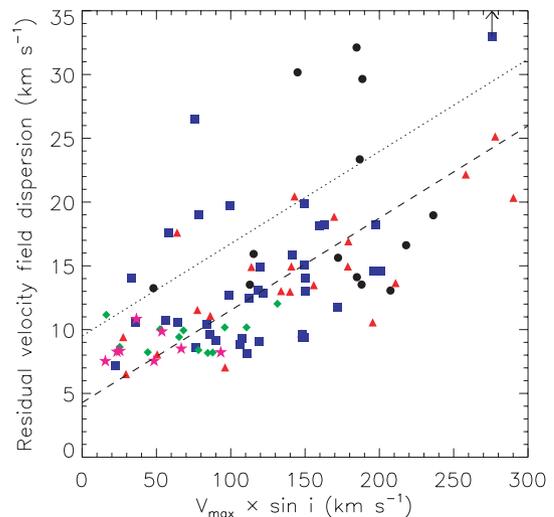

Figure 2. Dispersion in residual velocity field versus maximum velocity, sorted by Hubble morphological type: black circles $0 \leq t < 2$, red triangles $2 \leq t < 4$, blue squares $4 \leq t < 6$, green rhombuses $6 \leq t < 8$ and pink stars $8 \leq t < 10$. The dashed line represents the linear regression in the data. The points above the dotted line are discussed in Section 3.3. UGC 3334 labelled with an arrow has actually a residual velocity dispersion of 54 km s^{-1} (see Table C2).

having strong bar or spiral structure and to data of lower quality: (i) galaxies dominated by strong bars (UGC 89 and UGC 11407), or strong spiral structures (UGC 5786 and UGC 3334) are not correctly described by our model which does not take into account non-axisymmetric motions; (ii) the velocity field of the lower quality data (UGC 1655, UGC 3528, IC 476, UGC 4256, UGC 4456, IC 2542, UGC 6277, UGC 9406 and UGC 11269) presents a mean size of the bins greater than 25 pixels and an integrated total Hα flux lower than 4.5 W m^{-2} (a rough calibration of the total Hα flux of GHASP galaxies using the 26 galaxies we have in common with James et al. 2004 has been made, assuming a spectral ratio of Hα to [N II] of 3:1). Fig. 2 also shows that, for a given velocity amplitude, this correlation does not clearly depend on the morphological type. We note the well-known fact that late-type galaxies have on average a lower velocity amplitude than early-type ones.

For most of the galaxies seen almost edge-on (*i* higher than 75°), due to the thickness of the disc, no model has been fitted (see previous subsection) thus no residual velocity fields can be plotted.

3.4 Kinematical parameters

Table C2 gives the input (morphological) parameters of the fits and the results of the fits (output parameters, χ^2, and parameters of the residual maps). Table C3 gives some fundamental parameters of the galaxies compiled in the literature (morphological and Hubble type, distance, M_B, $D_{25}/2$, axial ratio, H I maps available in the literature), together with maximum velocity parameters computed from the rotation curves (V_{max}, quality flag on V_{max}). The four galaxies larger than our field-of-view are flagged in Table C3. For some galaxies for which the signal-to-noise ratio or the spatial coverage is too low, the fit could not converge correctly and one or two parameters (*i* and PA) were usually fixed to the morphological values to achieve the fit. These galaxies are flagged with an asterisk (*) in Table C2. When it is the case, parameter determinations are discussed in Appendix B. For some extreme cases, even when *i* and PA were fixed, the fit does
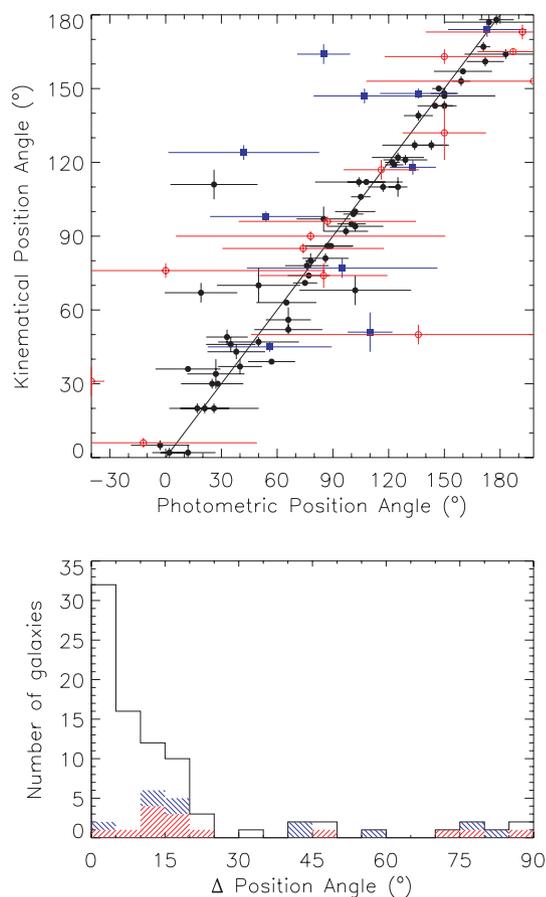
Figure 3. Top panel: kinematical versus morphological (HyperLeda) PAs of the major-axis. Galaxies for which no accurate morphological PA has been computed are shown by the red open circles; galaxies having an inclination lower than 25° are displayed by the blue squares; the other galaxies are represented by the black circles. Bottom panel: histogram of the variation between kinematical and morphological PAs. The red hash, blue hash and residual white represent, respectively, the galaxies for which no accurate PA has been measured, for which inclination is lower than 25° and the other galaxies of the sample.

circle and their common centre is thus defined. The angle formed between the major-axis of the ellipse and the previously defined line represents the 1σ uncertainty on the PA.

For all galaxies, HyperLeda references a list of PAs from which they often computed one PA value. HyperLeda does not compute a value when the dispersion or the uncertainty is too large. Indeed, the PA may be quite different from a study to another, depending on (i) the method, (ii) the size of the disc and (iii) the broad-band colours considered by the different authors (non-homogeneity in radius and colour measurements). When no value is computed in HyperLeda, we put the whole list in Table C2. Moreover, to make it readable and to minimize the dispersion on Fig. 3, we only plot the morphological value found closest from the kinematical PA. In Fig. 3, we have distinguished the bulk of galaxies (black circles) for which the agreement is rather good (lower than 20° see Fig. 3, bottom panel) from (i) the galaxies for which no accurate morphological PA has been computed (red open circles) and (ii) the galaxies having an inclination lower than 25° (blue squares). Indeed, some galaxies present a disagreement between kinematical and photometric PAs larger than 20°. Most of these galaxies have (i) a bad morphological determination of the PA or (ii) have kinematical inclinations lower than 25° or (iii) are specific cases (namely UGC 3740, IC 476, UGC 4256, UGC 4422) and are discussed in Appendix B. On the other hand, Fig. 3 shows that morphological PAs have systematically higher uncertainties than kinematical ones; this is specially true for galaxies with low inclination. Quantitatively, for kinematical inclinations greater than 25°, the mean error on morphological PAs is $\sim 3°$, while the mean error on kinematical PAs is $\sim 2°$. For inclinations lower than 25°, the difference in the methods is even larger: the mean error on morphological PAs is $\sim 27°$, while the mean error on kinematical PAs is $\sim 3°$. For comparison, Barnes & Sellwood (2003), using the difference between morphological and kinematical parameters, estimated that non-axisymmetric features introduce inclination and PA uncertainties of 5° on average.

The histogram of the variation between kinematical and morphological PAs given in Fig. 3 (bottom panel) indicates that (i) for more than 60 per cent of these galaxies, the agreement is better than 10°; (ii) for more than 83 per cent, the agreement is better than 20°; and (iii) the disagreement is larger than 30° for 15 per cent of these galaxies.

In other words, the position of the slit in long-slit spectroscopy (which is usually based on the major-axis determined from broad-band imagery) with respect to the actual PA may be not negligible, highlighting the strength of the integral field spectroscopy methods to determine the PAs (see also illustrations in Paper IV, Chemin et al. 2006; Daigle et al. 2006a).

In Fig. 4, the inclinations obtained by GHASP are compared with the photometric inclinations. On the top panel, the photometric inclination is the one computed using a correction factor depending on the morphological type (Hubble 1926):

$$\sin^2 i = \frac{1 - 10^{-2 \log r_{25}}}{1 - 10^{-2 \log r_0}}$$

where r_{25} is the apparent flattening, and $\log r_0 = 0.43 + 0.053t$ for the de Vaucouleurs type t ranging from -5 to 7, and $\log r_0 = 0.38$ for t higher than 7 (Paturel et al. 1997).

In the middle panel, the photometric inclination i is derived from the axial ratio b/a without any correction ($\cos i = b/a$). As for the PAs, the red open circles are the galaxies for which the morphological PA could not be determined accurately. The blue squares are the galaxies for which the difference between morphological and kinematical PAs exceeds 20°.

not converge. In particular for galaxies having high inclinations, then no model was computed (see Section 3.2).

As underlined in Paper I, Garrido (2003) and Paper IV, due to the difference in wavelength between the calibration and the redshifted Hα lines, the coating of the Fabry–Perot interferometer induces a small systematic bias (phase shift effect) to the absolute systemic velocities. We tabulate the systemic velocities without correcting them from this phase shift because the dispersion by the phase effect is typically of the same order of magnitude than the dispersion of the systemic velocities found in HyperLeda (Paper IV) and also because the forthcoming analysis and in particular the rotation curves do not depend on this effect.

In Fig. 3, the kinematical PAs obtained by GHASP are compared with the photometric PAs (found in HyperLeda). The error bar on the morphological PA, which is generally not homogenously given in the literature (or not given at all), has been estimated using the axial ratio and optical radius uncertainties. The galaxy disc in the sky plane is modelled by an ellipse of axial ratio b/a where a is equal to D_{25}. Given the uncertainty on D_{25}, ΔD_{25}, a circle of diameter $D_{25} - \Delta D_{25}/2$ having the same centre as the ellipse is considered. A line passing through the intersection between the ellipse and the

The dispersion around the $y = x$ line (equality between the morphological and kinematical inclinations) decreases with the inclination. The main discrepancy is found for low inclinations. The corresponding galaxies are discussed in Appendix B (notes on individual galaxies). On the one hand, the morphological inclination of the galaxies having no robust determination of their morphological PA cannot be constrained correctly. On the other hand, galaxies for which the PA disagreement is relatively high have a high dispersion and their morphological inclination is statistically overestimated.

Excluding these galaxies which have a bad PA estimation, for low inclination systems, kinematical methods may underestimate the inclination or alternatively, morphological estimations may be overestimated. On average, the errors on morphological inclinations ($\sim6°$) and on kinematical inclinations ($\sim8°$) are comparable. Whatever be the method used, the determination of the inclination of galaxies having a low inclination remains less accurate than for more inclined galaxies.

The comparison of the two plots in Fig. 4 (top and middle panels) shows that galaxies with high inclination have a better agreement between their kinematical inclination and their morphological inclination computed considering a thin disc. The actual thickness of the disc may not be reproduced by our simple thin disc velocity field modelling. If it is the case, the kinematical inclination may be systematically underestimated. Alternatively, the good agreement between the thin disc morphological inclination and kinematical inclination may mean that the morphological thickness corrections are overestimated.

The histogram of the difference between morphological and kinematical inclinations (Fig. 4, bottom panel) shows that a difference of inclination larger than $10°$ is found for 40 per cent of the sample.

4 THE TULLY–FISHER RELATION

Among the present sample of 108 galaxies, we have plotted the Tully–Fisher relation (Tully & Fisher 1977, M_B as a function of $\log 2 V_{max}$) for a subsample of 94 galaxies in Fig. 5. The 14 other galaxies are not considered in the present discussion because (i) for five galaxies the rotation curve does not reach the maximum rotation velocity (UGC 1655, UGC 4393, UGC 6523, UGC 8898 and UGC 9406); (ii) no B magnitude is available for one galaxy (UGC 3685); and (iii) no velocity measurement either on the rotation curve or in the position–velocity diagram is possible for eight other galaxies (see Table C3).

The maximum velocity V_{max} has been obtained from the fit to the velocity field. The error on V_{max} is the quadratic combination of the error due to the uncertainty in the inclination (the product $V_{max} \times \sin i$ is constant) and the median dispersion in the rings of the rotation curve beyond $D_{25}/10$. In the cases where the rotation curve has no point beyond that radius, we replace this term by the intrinsic uncertainty on the velocity determination due to the spectral resolution ($8 \, km \, s^{-1}$). For the highly inclined galaxies for which no correct fit was possible with our method (because it does not take into account the thickness of the disc, see Section 3.2), we computed V_{max} from the Hα position–velocity diagram corrected from the photometric inclination. For them, the error on V_{max} is simply the intrinsic uncertainty on the velocity determination. For the particular case of UGC 5786, the fit is not good enough to use it to compute V_{max} because of the long blue northern tail and because of the strong bar. We estimated V_{max} to $80 \, km \, s^{-1}$ by eye inspection of the rotation curve. These galaxies are flagged in Table C3.
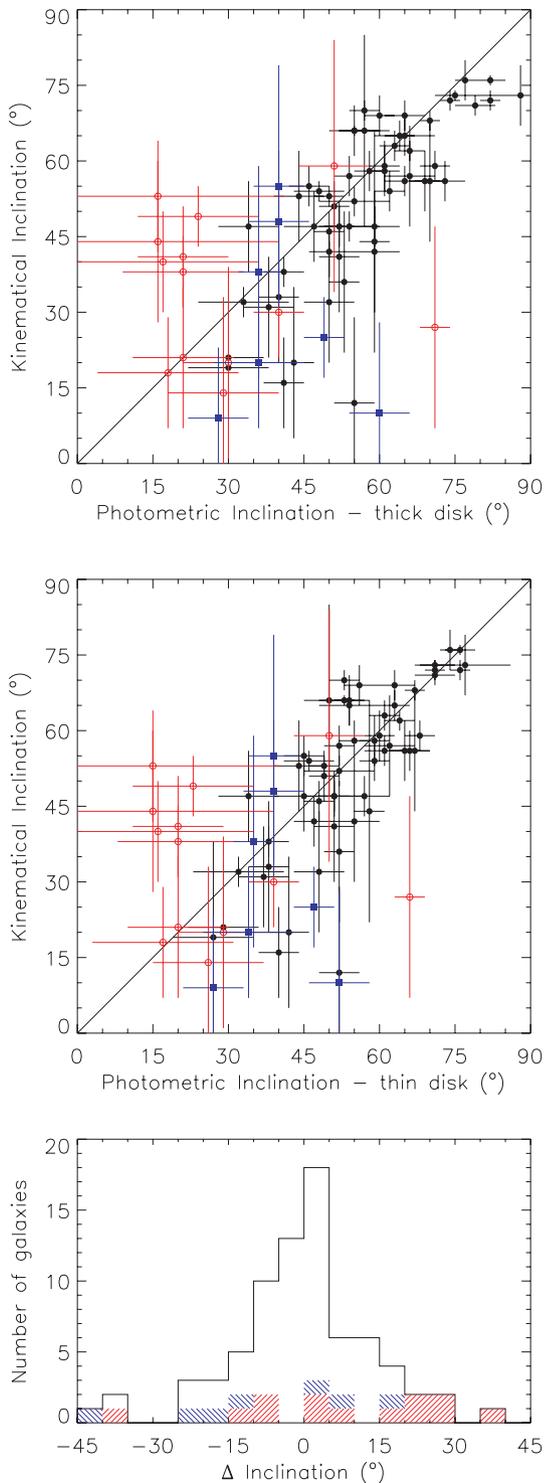
Figure 4. Top panel: kinematical versus thick disc morphological inclinations. Middle panel: kinematical versus thin disc morphological inclinations. Top and middle panels: galaxies for which no accurate morphological PA has been computed are shown by the red open circles; galaxies with a difference between the kinematical and morphological PAs larger than $20°$ are displayed with the blue squares; the other galaxies are represented by the black circles. Bottom: histogram of the variation between kinematical and morphological inclinations. The red hash, blue hash and residual white represent, respectively, the galaxies for which no accurate PA has been measured, for which the difference between the kinematical and morphological PAs is larger than $20°$ and the other galaxies of the sample.
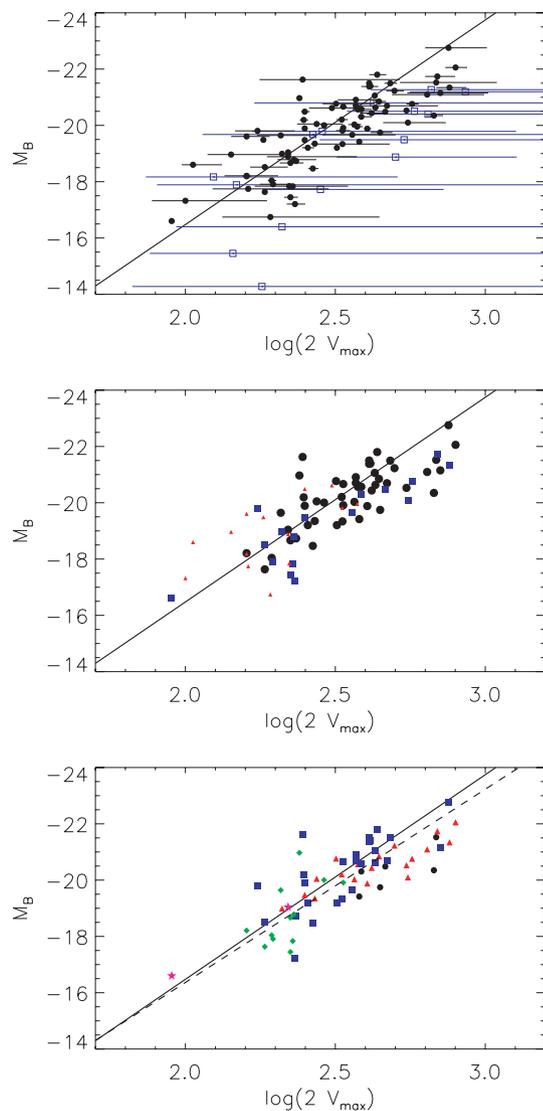
Figure 5. Tully–Fisher relation for our sample of galaxies. The solid line represents the B magnitude Tully–Fisher relation determined by Tully & Pierce (2000) from nearby galaxies in clusters (Ursa Major, Pisces filament, Coma). Top panel: sorted by inclination – low-inclination galaxies ($i < 25°$): blue squares; other galaxies ($i \geq 25°$): black circles. Middle panel: sorted by V_{max} flags – V_{max} reached: black dots, large size; V_{max} probably reached: blue squares, medium size; V_{max} probably not reached: red triangles, small size. Bottom panel: sorted by morphological type – black circles from 0 to 2; red triangles from 2 to 4; blue squares from 4 to 6; green rhombuses from 6 to 8; pink stars from 8 to 10; the dotted line represents the best linear fit in the data.

The solid line in Fig. 5 is the relation found by Tully & Pierce (2000):

$$M_B = -7.3(\log 2V_{max} - 2.5) - 20.1.$$

In Fig. 5 (top panel), the error bars on the velocity are displayed and galaxies with inclination lower than 25° are distinguished (blue open squares). We clearly note that these galaxies have statistically higher velocities than expected from the Tully & Pierce (2000) relation. This effect is due to the link between the inclination and velocity determination. Indeed, in the velocity fields, we observe the projected velocity in the line-of-sight: $V_{rot} \times \sin i$. A given underestimate of the inclination thus leads to a higher overestimate

on maximum velocity for low inclination galaxies than for high inclination galaxies. This also explains the strong trend for low inclination galaxies to exhibit large error bars. Considering this effect, we choose to exclude the 15 galaxies with inclinations lower than 25° from the Tully–Fisher analysis.

Among the 79 remaining galaxies, the maximum velocity V_{max} is reached for 48 of them (black dots, large size), probably reached for 17 of them (blue squares, medium size) and probably not reached for 14 of them (red triangles, small size). They are distinguished in Fig. 5 (middle panel) and flagged in Table C3. The quality flag on the maximum velocity is deduced (i) from the inspection of the shape of the Hα rotation curves and position–velocity diagrams; (ii) from the comparison with H I velocity fields and rotation curves when available (see Table C3); and (iii) from the comparison of the Hα velocity fields amplitudes with H I linewidths (see individual comments in Appendix B). It appears from this last point that the H I linewidth at 20 per cent has most often the best agreement with the Hα velocity field amplitude (better than the linewidth at 50 per cent). Fig. 5 (middle panel) confirms the two classifications 'V_{max} probably reached' and 'V_{max} probably not reached' since for the majority of each class the points are, respectively, in agreement and above the Tully & Pierce (2000) relation. From the two classes 'V_{max} reached' and 'V_{max} probably reached', we find the following relation:

$$M_B = (-6.9 \pm 1.6)[\log 2V_{max} - 2.5] - (19.8 \pm 0.1). \tag{1}$$

This relation is displayed as a dotted line in Fig. 5, in which morphological types are distinguished for the two best classes (black circles from 0 to 2, red triangles from 2 to 4, blue squares from 4 to 6, green rhombuses from 6 to 8 and pink stars from 8 to 10). Coefficients have been computed using the mean of the coefficients obtained (i) using a fit on the absolute magnitudes (as dependent variables) and (ii) using a fit on the velocities (as dependent variables). The difference in the slope determination by these two methods is quite large due to a strong scatter in our data [the error on the parameter in equation (1) is half that difference]. Indeed, usually one uses local calibrators for which distance measurements are accurate (based on Cepheids, red giants branch, members of a same cluster, etc.) leading to a small scatter in the data. From our data, the main difficulty is that the distance determination is mostly based on the systemic velocity corrected from Virgo infall (see Table C3), and that no error bar on the magnitude can be easily estimated. Thus, we have no reason to be more confident on the velocity measurements (mainly affected by inclination determination) than on absolute magnitude measurements. However, despite the dispersion in our data, the resulting parameters using the mean of the two fits are in good agreement with Tully & Pierce (2000), even if our slope is a bit lower. A lower slope had already been observed in H I (Yasuda, Fukugita & Okamura 1997; Federspiel, Tammann & Sandage 1998) and more systematically in optical studies (e.g. Courteau 1997; Rubin, Waterman & Kenney 1999; Márquez et al. 2002; Papers III and IV).

For the Tully–Fisher relation we derived, on the one hand, we observe that fast rotators ($V_{max} > 300 \, \text{km s}^{-1}$: UGC 89, UGC 4422, UGC 4820, UGC 5532, UGC 8900, UGC 8937 and UGC 11470) are less luminous than expected, except maybe for UGC 3334 which is one of the fastest disc rotators (Rubin, Roberts & Ford 1979) (see discussion in Appendix B). This trend can also be observed in several optical studies (Márquez et al. 2002; Papers III and IV). Interestingly, these fast rotators are not observed in H I samples (Tully & Pierce 2000; Federspiel et al. 1998). This may be explained by the shape of the rotation curves of fast rotators: except for UGC 8900,

the rotation curve always reaches the maximum velocity within the first 5 arcsec (i.e. within our seeing). This inner maximum may be missed in H I because of beam smearing, averaging the maximum velocity reached at the centre. Note that the rotation curve of UGC 5532 is clearly decreasing, while the other ones are flat. On the other hand, slow rotators have a small velocity gradient and within the optical regions the maximum could not be reached, whereas H I observations would be able to measure it without any doubt. These two effects could explain the trend observed in optical Tully–Fisher relations.

The result obtained for the Tully–Fisher relation is in agreement with the one obtained with the previous samples (Papers III and IV). The analysis of the whole GHASP sample will be done in a forthcoming paper (Epinat et al., in preparation).

5 SUMMARY AND PERSPECTIVES

The knowledge of the links between the kinematical and dynamical state of galaxies will help us to have a better understanding of the physics and evolution of galaxies. The GHASP sample, which consists of 203 spiral and irregular galaxies covering a wide range of morphological types and absolute magnitudes, has been constituted in order to provide a kinematical reference sample of nearby galaxies. The GHASP galaxies have been observed in the Hα line with a scanning Fabry–Perot, providing data cubes.

We present in this paper the last set of 108 galaxies leading to 106 velocity fields and 93 rotation curves. By now, this work consists of the largest sample of galaxies observed with Fabry–Perot techniques ever presented in the same publication. Added to the four previous sets already obtained in the frame of this survey (Paper I–IV), GHASP represents the largest sample of 2D velocity fields of galaxies observed at Hα wavelength. For each galaxy, we have presented the Hα velocity field, the Hα monochromatic image and eventually the Hα residual velocity field, the position–velocity diagram along the major-axis and the rotation curve when available.

The following major improvements in the reduction and in the analysis have been developed and implemented.

(i) In order to optimize the spatial resolution for a given signal-to-noise ratio, adaptive binning method, based on the 2D Voronoi tessellations, was used to derive the 3D Hα data cubes and to extract from it the line maps and the radial velocity fields.

(ii) The ghosts due to reflections at the air–glass interfaces of the interferometer have been removed in the data cubes.

(iii) The analysis of the faint outskirts or diffuse regions is made automatic.

(iv) The kinematical parameters and their error bars are directly derived from the velocity field.

(v) The uncertainties are estimated from the analysis of the residual velocity field power spectrum.

(vi) The whole 2D velocity field has been used rather than successive crowns in tilted-ring models to compute the rotation curve and the error bars.

The main results of this paper are summarized by the following items.

(i) The absence of typical and well-known bias in the residual velocity fields means that the best determination of the kinematical parameters has been achieved.

(ii) The mean velocity dispersion on each residual velocity field ranges from 6 to 23 km s^{-1} with a mean value around 13 km s^{-1} and is strongly correlated with the maximum amplitude of the velocity field. For a given velocity amplitude, this correlation does not clearly depend on the morphological type. Only strongly barred galaxies have a higher residual velocity dispersion than mild-barred or non-barred galaxies. Peculiar galaxies also show a high residual velocity dispersion.

(iii) The kinematical PAs obtained by GHASP are compared with the photometric PAs. Morphological PAs have systematically higher uncertainties than kinematical ones, this is specially true for galaxies with low inclination. When using long-slit spectroscopy, the PA should be known a priori. This is usually done using morphological determinations based on broad-band imagery. We have shown that in some cases the difference between the PA determined using 2D kinematics and morphologies may be as large as 90° and that in any case the PAs are better determined by 2D kinematics. Thus, large differences between morphological and kinematical PAs may lead us to incorrect rotation curve and maximum velocity determination when using long-slit spectroscopy. This may strongly bias mass distribution models and Tully–Fisher studies, highlighting the strength of integral field spectroscopy with a Fabry–Perot.

(iv) The morphological inclination of the galaxies having no robust determination of their morphological PA cannot be constrained correctly. Galaxies for which the PA disagreement is relatively high have a high dispersion and their morphological inclination is statistically overestimated. Galaxies with high inclination have a better agreement between their kinematical inclination and their morphological inclination computed assuming a thin disc. For galaxies with intermediate disc inclinations (higher than 25° and lower than 75°), to reduce the degrees of freedom in kinematical models, the inclination could be fixed to the morphological value. This is specially true when only low-quality kinematical data are available as it is the case for high-redshift galaxies.

(v) The Tully–Fisher relation found with this new set of data is in good agreement with Tully & Pierce (2000), even if our slope is a bit lower. This trend for a lower slope has already been observed in H I by Yasuda et al. (1997) and Federspiel et al. (1998). Galaxies with inclination lower than 25° have statistically higher velocities than expected from the Tully–Fisher relation derived by Tully & Pierce (2000). Fast rotators ($V_{max} > 300$ km s^{-1}) are less luminous than expected. This may be explained by the shape of the rotation curves of fast rotators.

were processed into the present compressed digital form with the permission of these institutions.

REFERENCES

Amram P., Le Coarer E., Marcelin M., Balkowski C., Sullivan W. T., III, Cayatte V., 1992, A&AS, 94, 175

Amram P., Marcelin M., Balkowski C., Cayatte V., Sullivan W. T., III, Le Coarer E., 1994, A&AS, 103, 5

Arp H., 1966, Atlas of Peculiar Galaxies. California Inst. Technology, Pasadena

Balick B., Heckman T., 1981, A&A, 96, 271

Barnes E. I., Sellwood J. A., 2003, AJ, 125, 1164

Barnes E. I., Sellwood J. A., Kosowsky A., 2004, AJ, 128, 2724

Battaglia G., Fraternali F., Oosterloo T., Sancisi R., 2006, A&A, 447, 49

Begeman K. G., 1987, PhD thesis, Kapteyn Institute

Bottema R., 1989, A&A, 221, 236

Bottinelli L., Gouguenheim L., Fouque P., Paturel G., 1990, A&AS, 82, 391

Braine J., Combes F., Casoli F., Dupraz C., Gerin M., Klein U., Wielebinski R., Brouillet N., 1993, A&AS, 97, 887

Braun R., Thilker D., Walterbos R. A. M., 2003, A&A, 406, 829

Bravo-Alfaro H., Szomoru A., Cayatte V., Balkowski C., Sancisi R., 1997, A&AS, 126, 537

Broeils A. H., van Woerden H., 1994, A&AS, 107, 129

Carollo C. M., Stiavelli M., Mack J., 1998, AJ, 116, 68

Carozzi N., 1976, A&A, 49, 431

Catinella B., Haynes M. P., Giovanelli R., 2005, AJ, 130, 1037

Catinella B., Giovanelli R., Haynes M. P., 2006, ApJ, 640, 751

Chemin L. et al., 2006, MNRAS, 366, 812

Cote S., Carignan C., Sancisi R., 1991, AJ, 102, 904

Courteau S., 1997, AJ, 114, 2402

Daigle O., Carignan C., Amram P., Hernandez O., Chemin L., Balkowski C., Kennicutt R., 2006a, MNRAS, 367, 469

Daigle O., Carignan C., Hernandez O., Chemin L., Amram P., 2006b, MNRAS, 368, 1016 (D2006)

de Vaucouleurs G., 1979, ApJ, 227, 380

de Vaucouleurs G., Caulet A., 1982, ApJS, 49, 515

Doyle M. T. et al., 2005, MNRAS, 361, 34

Elfhag T., Booth R. S., Hoeglund B., Johansson L. E. B., Sandqvist A., 1996, A&AS, 115, 439

Epinat B., Amram P., Balkowski C., 2007, in Combes F., Palous J., eds, IAU Symp. Vol. 235, Galaxy Evolution Across the Hubble Time. Cambridge University Press, Cambridge, p. 401

Eskridge P. B. et al., 2002, ApJS, 143, 73

Fathi K. et al., 2008, ApJ, 645, L17

Federspiel M., Tammann G. A., Sandage A., 1998, ApJ, 495, 115

Ferguson A. M. N., Wyse R. F. G., Gallagher J. S. III, Hunter D. A., 1996, AJ, 111, 2265

Fridman A. M., Afanasiev V. L., Dodonov S. N., Khoruzhii O. V., Moiseev A. V., Sil'chenko O. K., Zasov A. V., 2005, A&A, 430, 67

Gach, J.-L. et al., 2002, PASP, 114, 1043

García-Barreto J. A., Franco J., Carrillo R., Venegas S., Escalante-Ramírez B., 1996, Rev. Mex. Astron. Astrofis., 32, 89

Garrido O., 2003, PhD thesis, Université de Provence (France)

Garrido O., Marcelin M., Amram P., Boulesteix J., 2002, A&A, 387, 821

Garrido O., Marcelin M., Amram P., Boissin O., 2003, A&A, 399, 51

Garrido O., Marcelin M., Amram P., 2004, MNRAS, 349, 225

Garrido O., Marcelin M., Amram P., Balkowski C., Gach J. L., Boulesteix J., 2005, MNRAS, 362, 127

Gavazzi G., Catinella B., Carrasco L., Boselli A., Contursi A., 1998, AJ, 115, 1745

Gavazzi G., Boselli A., Donati A., Franzetti P., Scodeggio M., 2003, A&A, 400, 451

Georgelin Y. P., 1970, A&A, 9, 441

Giovanardi C., Salpeter E. E., 1985, ApJS, 58, 623

Giovanelli R., Haynes M. P., 1993, AJ, 105, 1271

Gooch R., 1996, in Jacoby G. H., Barnes J., eds, ASP Conf. Ser. Vol. 101, Astronomical Data Analysis Software and Systems V. Astron. Soc. Pac. San Francisco, p. 80

Hameed S., Devereux N., 2005, AJ, 129, 2597

Hattori T. et al., 2004, AJ, 127, 736

Haynes M. P., van Zee L., Hogg D. E., Roberts M. S., Maddalena R. J., 1998, AJ, 115, 62

Haynes M. P., Giovanelli R., Salzer J. J., Wegner G., Freudling W., da Costa L. N., Herter T., Vogt N. P., 1999, AJ, 117, 1668

Héraudeau P., Simien F., Maubon G., Prugniel P., 1999, A&AS, 136, 509

Hernandez O., Wozniak H., Carignan C., Amram P., Chemin L., Daigle O., 2005a, ApJ, 632, 253

Hernandez O., Carignan C., Amram P., Chemin L., Daigle O., 2005b, MNRAS, 360, 1201

Hickson P., Kindl E., Auman J. R., 1989, ApJS, 70, 687

Hoffman G. L., Salpeter E. E., Farhat B., Roos T., Williams H., Helou G., 1996, ApJS, 105, 269

Hubble E. P., 1926, ApJ, 64, 321

Huchtmeier W. K., Witzel A., 1979, A&A, 74, 138

Hunter D. A., Elmegreen B. G., 2004, AJ, 128, 2170

Irwin J. A., 1994, ApJ, 429, 618

James P. A. et al., 2004, A&A, 414, 23

Jiménez-Vicente J., Battaner E., 2000, A&A, 358, 812

Kamphuis J. J., Sijbring D., van Albada T. S., 1996, A&AS, 116, 15

Karachentsev I. D., 1972, Astrofizicheskie Issledovaniia Izvestiya Spetsial'noj Astrofizicheskoj Observatorii, 7, 3

Karachentsev I. D., Mineva V. A., 1984a, Sov. Astron. Lett., 10, 105

Karachentsev I. D., Petit M., 1990, A&AS, 86, 1

Karachentsev I. D., Myneva V. A., 1984b, Sov. Astron. Lett., 10, 235

Karachentsev I. D., Karachentseva V. E., Huchtmeier W. K., Makarov D. I., 2004, AJ, 127, 2031

Kaufman M., Brinks E., Elmegreen B. G., Elmegreen D. M., Klarić M., Struck C., Thomasson M., Vogel S., 1999, AJ, 118, 1577

Kaufman M., Sheth K., Struck C., Elmegreen B. G., Thomasson M., Elmegreen D. M., Brinks E., 2002, AJ, 123, 702

Knapen J. H., Stedman S., Bramich D. M., Folkes S. L., Bradley T. R., 2004, A&A, 426, 1135

Koopmann R. A., Kenney J. D. P., Young J., 2001, ApJS, 135, 125

Koopmann R. A., Haynes M. P., Catinella B., 2006, AJ, 131, 716

Kornreich D. A., Haynes M. P., Lovelace R. V. E., van Zee L., 2000, AJ, 120, 139

Krajnović D., Cappellari M., de Zeeuw P. T., Copin Y., 2006, MNRAS, 366, 787

Kregel M., van der Kruit P. C., Freeman K. C., 2005, MNRAS, 358, 503

Krumm N., Salpeter E. E., 1979, AJ, 84, 1138

Lang R. H. et al., 2003, MNRAS, 342, 738

Lewis B. M., 1987, ApJS, 63, L515

Márquez I., Moles M., 1996, A&AS, 120, 1

Márquez I., Masegosa J., Moles M., Varela J., Bettoni D., Galletta G., 2002, A&A, 393, 389

Martin C. L., 1998, ApJ, 506, 222

Meyssonnier N., 1984, A&AS, 58, 351

Moustakas J., Kennicutt R. C., Jr, 2006, ApJS, 164, 81

Nilson P., 1973, Uppsala General Catalogue of Galaxies, Nova Acta Regiae Soc. Sci. Upsaliensis Ser. V

Noordermeer E., van der Hulst J. M., Sancisi R., Swaters R. A., van Albada T. S., 2005, A&A, 442, 137

O'Connell R. W., Gallagher J. S., III, Hunter D. A., 1994, ApJ, 433, 65

Paturel G., Garcia A. M., Fouque P., Buta R., 1991, A&A, 243, 319

Paturel G. et al., 1997, A&AS, 124, 109

Paturel G., Fang Y., Petit C., Garnier R., Rousseau J., 2000, A&AS, 146, 19

Persic M., Salucci P., 1991, ApJ, 368, 60

Persic M., Salucci P., Stel F., 1996, MNRAS, 281, 27

Pignatelli E. et al., 2001, MNRAS, 323, 188

Pisano D. J., Wilcots E. M., Liu C. T., 2002, ApJS, 142, 161

Puech M., Hammer F., Flores H., Östlin G., Marquart T., 2006, A&A, 455, 119

Rampazzo R., Reduzzi L., Sulentic J. W., Madejsky R., 1995, A&AS, 110, 131

Rasmussen J., Ponman T. J., Mulchaey J. S., 2006, MNRAS, 370, 453

Rhee M.-H., van Albada T. S., 1996, A&AS, 115, 407

Richter O.-G., Huchtmeier W. K., 1991, A&AS, 87, 425

Rossa J., Dettmar R.-J., 2003, A&A, 406, 505

Rownd B. K., Dickey J. M., Helou G., 1994, AJ, 108, 1638

Rubin V. C., Roberts M. S., Ford W. K., Jr, 1979, ApJ, 230, 35

Rubin V. C., Thonnard N., Ford W. K., Jr, 1980, ApJ, 238, 471

Rubin V. C., Thonnard N. T., Ford W. K., Jr, 1982, AJ, 87, 477

Rubin V. C., Waterman A. H., Kenney J. D. P., 1999, AJ, 118, 236

Sandage A., Bedke J., 1994, The Carnegie Atlas of Galaxies. Carnegie Institution of Washington with The Flintridge Foundation, Washington, DC

Sauty S. et al., 2003, A&A, 411, 381

Schneider S. E., Thuan T. X., Magri C., Wadiak J. E., 1990, ApJS, 72, 245

Schommer R. A., Bothun G. D., Williams T. B., Mould J. R., 1993, AJ, 105, 97

Schulman E., Bregman J. N., Brinks E., Roberts M. S., 1996, AJ, 112, 960

Schwartz C. M., Martin C. L., Chandar R., Leitherer C., Heckman T. M., Oey M. S., 2006, ApJ, 646, 858

Sengupta C., Balasubramanyam R., 2006, MNRAS, 369, 360

Shapley A., Fabbiano G., Eskridge P. B., 2001, ApJS, 137, 139

Shostak G. S., van der Kruit P. C., Hummel E., Shaver P. A., van der Hulst J. M., 1982, A&A, 115, 293

Sofue Y., Tomita A., Tutui Y., Honma M., Takeda Y., 1998, PASJ, 50, 427

Spano M., Marcelin M., Amram P., Carignan C., Epinat B., Hernandez O., 2008, MNRAS, 383, 297

Springob C. M., Haynes M. P., Giovanelli R., Kent B. R., 2005, ApJS, 160, 149

Stil J. M., Israel F. P., 2002, A&A, 392, 473

Strickland D. K., Heckman T. M., Colbert E. J. M., Hoopes C. G., Weaver K. A., 2004, ApJS, 151, 193

Swaters R. A., van Albada T. S., van der Hulst J. M., Sancisi R., 2002, A&A, 390, 829

Takase B., Miyauchi-Isobe N., 1991, Publications of the National Astronomical Observatory of Japan, 2, 7

Theureau G., Bottinelli L., Coudreau-Durand N., Gouguenheim L., Hallet N., Loulergue M., Paturel G., Teerikorpi P., 1998, A&AS, 130, 333

Tift W. G., Cocke W. J., 1988, ApJS, 67, 1

Tomita A., Ohta K., Saito M., 1994, PASJ, 46, 335

Tully R. B., Fisher J. R., 1977, A&A, 54, 661

Tully R. B., Pierce M. J., 2000, ApJ, 533, 744

Usui T., Saitō M., Tomita A., 2001, AJ, 121, 2483

van der Hulst J. M., Huchtmeier W. K., 1979, A&A, 78, 82

van der Kruit P. C., Allen R. J., 1978, ARA&A, 16, 103

van Driel W., Marcum P., Gallagher J. S., III, Wilcots E., Guidoux C., Monnier Ragaigne D., 2001, A&A, 378, 370

van Moorsel G. A., 1983, A&AS, 54, 19

van Zee L., 2000, AJ, 119, 2757

Vauglin I. et al., 1999, A&AS, 135, 133

Vetterling W. T., Flannery B. P., Press W. H., Teukolski S. A., 1989, Numerical Recipes in FORTRAN - The Art of Scientific Computing, 2nd edn. Cambridge Univ. Press, Cambridge

Vogt N. P., Haynes M. P., Herter T., Giovanelli R., 2004, AJ, 127, 3273

Vorontsov-Velyaminov B. A., Krasnogorskaya A. A., 1994, VizieR Online Data Catalog, 7062, 0

Walter F., Weiss A., Martin C., Scoville N., 2002, AJ, 123, 225

Wang Z., Scoville N. Z., Sanders D. B., 1991, ApJ, 368, 112

Warmels R. H., 1988, A&AS, 73, 453

Warner P. J., Wright M. C. H., Baldwin J. E., 1973, MNRAS, 163, 163

Wehner E. H., Gallagher J. S. III, 2005, ApJ, 618, L21

Wilcots E. M., Prescott M. K. M., 2004, AJ, 127, 1900

Wilcots E. M., Turnbull M. C., Brinks E., 2001, ApJ, 560, 110

Yasuda N., Fukugita M., Okamura S., 1997, ApJS, 108, 417

APPENDIX A: BUILDING A ROTATION CURVE

A1 The model

For each of the N independent bins covering the field-of-view of the galaxy, the vector velocity in the frame of the galactic plane is described by the following two components lying in the plane of the galaxy.

(i) $V_{rot}(R)$: the rotation velocity; and
(ii) $V_{exp}(R)$: the expansion velocity.

There is one component perpendicular to this plane:

(i) $V_z(R)$: the vertical motion velocity.

The observed radial velocities $V_{obs}(R)$ is linked to $V_{rot}(R)$, $V_{exp}(R)$ and $V_z(R)$ through the following five additional parameters.

(i) PA: the PA of the major-axis of the galaxy (measured counterclockwise from the north to the direction of the receding side of the galaxy).
(ii) i: the inclination of the galactic disc with respect to the sky plane.
(iii) V_{sys}: the systemic velocity of the galaxy.
(iv) α: the right ascension of the rotation centre.
(v) δ: the declination of the rotation centre.

through the following equation:

$$\begin{aligned} V_{obs} = {} & V_{sys} + V_{rot}(R) \cos \theta \sin i \\ & + V_{exp}(R) \sin \theta \sin i \\ & + V_z(R) \cos i. \end{aligned} \tag{A1}$$

R and θ being the polar coordinates in the plane of the galaxy. The angle in the plane of the galaxy, θ, is linked to the PA, the inclination i, the position x, y and centre x_c, y_c in the sky by the set of equations (A2)–(A7):

$$\cos \theta = R \cos \psi, \tag{A2}$$

$$\sin \theta = R \frac{\sin \psi}{\cos i}, \tag{A3}$$

$$\cos \psi = \frac{(y - y_c) \cos(PA) - (x - x_c) \sin(PA)}{r}, \tag{A4}$$

$$\sin \psi = -\frac{(x - x_c) \cos(PA) + (y - y_c) \sin(PA)}{r}, \tag{A5}$$

$$r = \sqrt{(x - x_c)^2 + (y - y_c)^2}, \tag{A6}$$

$$R = r \sqrt{\cos^2 \psi + \frac{\sin^2 \psi}{\cos^2 i}}, \tag{A7}$$

where ψ is the counterclockwise angle in the plane of the sky from the north.

Formally, one has to solve a system of N equations (as many equations as the number N of pixels taken into account) with $8N$ unknowns.

If one makes the assumption that, at the first order, for spiral galaxies, the expansion and vertical motions are negligible with respect to the rotation velocity, equation (A1) becomes

$$V_{obs}(R) = V_{sys}(R) + V_{rot}(R) \cos \theta \sin i.$$

This leads us to solve a system of N equations with $6N$ unknowns.

A usual solution to solve this degenerate system is to fix V_{sys} to a unique value for a given galaxy, and to consider that i, PA, x_c and y_c only depend on the galactic radius (to take warps into account), as it is the case for $V_{rot}(R)$. The field is decomposed into a certain number of elliptical rings (at given radii, with a given width) for which a set of parameters is computed for the corresponding radii (Begeman 1987). The number of rings being at least one order of magnitude less than N, the system of equations is no more degenerate. The physical width of the rings is typically ranging from 3 to 6 pixels ($\sim$2–4 arcsec).

We decided to use a new method. To solve this degenerate system of equations, the number of unknowns is reduced by introducing physical constraints: V_{sys}, i, PA, x_c and y_c are fixed to a unique value for a given galaxy as warps are hardly observed within optical radius.

Moreover, the rotation velocity is approximated by a function with only four parameters:

$$V_{rot}(R) = V_t \frac{(R/r_t)^g}{1 + (R/r_t)^a}. \tag{A8}$$

A2 Method

The method implemented is a χ^2-minimization method in the velocity field, using the IDL routine LMFIT. This routine, based on the Levenberg–Marquardt method (as described in section 15.5 of Vetterling et al. 1989), quickly converges towards the best model.

The starting set of parameters is chosen as follows: the rotation centre (x_c, y_c) is supposed to be the nucleus identified in our continuum image (when no nucleus can be seen, either in our images or in other bands, it is chosen as the centre of symmetry of our velocity field), i is derived from the axial ratio found in the literature, the PA is computed from the photometry (or eye-defined by the outer parts of our velocity field when not available), and the systemic velocity is taken from the literature.

In order to have a pretty good estimate of the analytical function parameters (A8), we fit them on this preliminary rotation curve.

We then let free all the parameters. We compute an iterative 3.5σ clipping on the velocity field to reject points that have not been cleaned.

For well-behaved galaxies, the iterative process was quite easy and rapidly converged. However, for some irregular galaxies with asymmetric rotation curves it was hard to converge and we had a strong uncertainty on the kinematical parameters, more especially the inclination which is the less constrained. In some specific cases, marked in Table C2 with an asterisk (*), we then fixed i and/or PA during the fit process.

The rotation curves are computed from the velocity fields, using the previously found projection parameters i, PA, x_c and y_c. A sector of $22\overset{\circ}{.}5$ in the plane of the galaxy around the minor-axis is excluded, and the points are weighted according to their corresponding $|\cos\theta|$. The rotation curves are sampled with rings.

In the inner parts, the width of the rings is set to match half the seeing, in order to respect Shannon sampling criteria. The transition radius r_t is defined by the first ring that contains more than 25 uncorrelated bins. If r_t is not reached before $D_{25}/10$, r_t is set to $D_{25}/10$. In the outer parts, the rotation curve is computed in successive rings containing the same number of uncorrelated bins, except eventually for the last ring of each side. The number of bins in the rings of the outer parts is set to the number between 16 and 25 that maximizes the number of uncorrelated bins of the last rings of each side. This range (16–25) is found to be the best compromise between the

signal-to-noise ratio and the spatial coverage in each ring. Thus, the width in each ring is variable. The velocity computed for each ring is then always the average of the same number of velocity points.

In the plots of rotation curve, for each individual ring, the vertical error bars are given by the dispersion of the rotation velocities inside the ring, normalized to the number of uncorrelated points inside the ring; the horizontal error bars represent the $\pm 1\sigma$ radius dispersion weighted by $\cos(\theta)$.

A3 Error estimation of the parameters

This method provides a determination of parameters errors, by associating a random noise to the data for which the amplitude can be fixed. However, this error seems unrealistically small. Indeed, the residual velocity field (difference between model and real velocity field) does not appear to be uniformly randomized. It contains the effects of non-axisymmetric motions such as expansion, spiral arms, bars or gas bubble expansion (local expansions), etc., that is to say real physical effects that cannot be described by our simple model. To be more realistic in parameter error determination, we simulate residual velocity fields from the real residual velocity field. We compute its power spectrum and put a random phase. As a result, the new residual field contains the same kind of structure, but placed differently. We then use a Monte Carlo method to estimate the errors: we compute the standard deviation in the parameters found over 250 simulated velocity fields. The advantage of this method is that it is completely automatic, and that it enables to use the whole information to compute global parameters and their errors. We also add $0\overset{\circ}{.}5$ to the PA uncertainty because of the uncertainty on the astrometry.

The typical accuracy we reach is about 1 arcsec for the position of the rotation centre, 2–3 km s^{-1} for the systemic velocity, 2° for the PA of the major-axis, but only 5°–10° for the inclination.

APPENDIX B: NOTES ON INDIVIDUAL GALAXIES

(i) *UGC 12893*. The Hα emission is very weak, as confirmed by James et al. (2004) who find a total surface brightness of 0.4 10^{-16} W m^{-2}. The quality of our rotation curve is thus rather poor, anyway a maximum rotation velocity ($\sim$72 km s^{-1}) seems to be reached within the optical limit, adopting the inclination of 19° deduced from our velocity field (HyperLeda gives 30° from the photometry). The width of the H I profile at 20 per cent (75 km s^{-1} from Giovanelli & Haynes 1993 and $\sim$90 km s^{-1} from Schneider et al. 1990) is in agreement with the amplitude of our Hα velocity field and suggests that we actually reach the maximum rotation velocity with our Hα rotation curve.

(ii) *UGC 89* (*NGC 23*). Because of the presence of a strong bar in this galaxy, the kinematics method used to determine the inclination is biased. Nevertheless, our kinematical inclination (33° ± 13°) is compatible with the photometric inclination (40° ± 4°) and with the value of 45° from Fridman et al. (2005) (Hα Fabry–Perot observations) as well as with the value of 50° from Noordermeer et al. (2005) (H I data from WHISP). Our Hα rotation curve reaches a plateau at $\sim$350 km s^{-1}, compatible with its morphological type (SBa) and with the position–velocity diagram from Noordermeer et al. (2005). The steep rise of the Hα rotation curve is also in agreement with the H I observation of Noordermeer et al. (2005) and in very good agreement with the Hα velocity field

of Fridman et al. (2005). Our Hα velocity field does not show any obvious evidence for interaction with its companion, UGC 94.

(iii) *UGC 94 (NGC 26)*. The steep rise of the Hα rotation curve is in agreement with the H I observation (Noordermeer et al. 2005). The Hα rotation curve reaches a plateau at ∼210 km s^{-1}, compatible with its morphological type (Sab). No Hα emission can be seen as a counter part of the H I extension to the south-east (Noordermeer et al. 2005). There is no obvious evidence for interaction with its companion, UGC 89, in our Hα velocity field.

(iv) *UGC 1013 (NGC 536 and NGC 542)*. An optical rotation curve has been obtained by Vogt et al. (2004) for UGC 1013. Because of bad weather, we could not get a sufficient signal-to-noise ratio when observing that galaxy with GHASP. On the other hand, we have detected, in the same field-of-view, Hα emission from its companion NGC 542 (systemic velocity around 4660 km s^{-1} from HyperLeda) with enough signal to get a reliable velocity field.

(v) *UGC 1317 (NGC 697)*. It is the brightest galaxy of the group NGC 677–NGC 697. H I data have been obtained by Giovanardi & Salpeter (1985), by Rhee & van Albada (1996) and by WHISP (website). A good agreement with H I observations within the first 2 arcmin is observed. Outside 2 arcmin, the H I rotation velocities of the receding side increase but we have no Hα emission there to check that. There is no obvious evidence for interaction with its companion, NGC 677, in our Hα velocity field.

(vi) *UGC 1437 (NGC 753)*. Relatively close to the centre of the A262 cluster, it is not H I deficient, however. It has been already observed in the optical by Rubin, Thonnard & Ford (1980), Amram et al. (1994) (Fabry–Perot data), Courteau (1997) and by Vogt et al. (2004) who found roughly the same kinematical parameters and rotation curves. From their H I rotation curve, Bravo-Alfaro et al. (1997) confirm the flatness of the Hα rotation curve even beyond the optical radius ($D_{25}/2$). Although less extended, our Hα velocity field is in good agreement with the H I observations by Broeils & van Woerden (1994) and by WHISP (website).

(vii) *UGC 1655 (NGC 828)*. Hα emission is detected only in its very centre, so that only the rising part of the Hα rotation curve can be plotted. The Hα image by Hattori et al. (2004) shows two bright patches on each side of the nucleus. Because of the limited extension of the rotation curve, we could not determine the inclination from the kinematics and adopted the value found in HyperLeda. Anyway, a plateau seems to be reached at ∼20 arcsec from the centre with a velocity ∼205 km s^{-1}. The rotation curve derived by Márquez et al. (2002) is in agreement with ours and extends a bit further but with a strong dispersion beyond 20 arcsec. Wang, Scoville & Sanders (1991) provide a CO rotation curve limited to a 10 arcsec radius, also in agreement with our Hα rotation curve. No H I map is available in the literature but the width of the H I profile at 20 per cent (427 km s^{-1} from Bottinelli et al. 1990; 556 km s^{-1} from Springob et al. 2005) is about twice our Hα velocity field amplitude, showing that our Hα rotation curve is far from reaching the maximum of the rotation velocity.

(viii) *UGC 1810 and UGC 1813*. Faint Hα detection in UGC 1810 despite two hours of integration in good conditions, while a strong Hα emitting blob is found in the central region of UGC 1813. Interestingly, two compact Hα emitters are detected away from the two galaxies in the eastern and western edges of our field-of-view (02^{h}21^{m}38^s, 39°21′35″ and 02^{h}21^{m}20^s, 39 deg 21′35″, respectively). These two objects are related with the two galaxies for which we estimate a systemic velocity around 7550 ± 100 km s^{-1}, in agreement with WHISP (website), whereas Hyper-Leda gives a systemic velocity of 7356 km s^{-1} ± 57. They may be intergalactic H II regions. A faint velocity gradient (∼30 km s^{-1})

is observed in the velocity field of the western object, suggesting that it may by a tidal dwarf galaxy candidate with a systemic velocity around 7680 km s^{-1} (modulo 378 km s^{-1} which is the free spectral range). At the opposite, no velocity gradient is seen in the eastern object having a systemic velocity of 7400 km s^{-1} (modulo 378 km s^{-1}).

(ix) *UGC 3056 (NGC 1569, Arp 210)*. Magellanic irregular starburst galaxy (Seyfert I type). We detect a strong Hα emission at the centre, causing ghosts in the southern outskirts of the galaxy in our data. This prevented us from computing an accurate velocity field in that region, even though there is some real emission there, as confirmed by the Hunter & Elmegreen (2004) line map. Also, we miss some extended filaments, being too faint or out of our field-of-view. Our Hα velocity field is almost uniform and does not show any evidence for rotation. Thus, we could not fit any rotation model to this velocity field and do not show any rotation curve here. However, the velocity field and the position–velocity diagram shows markedly higher velocities at the centre and lower velocities on the north-western side, a feature not clearly seen in previous studies of the ionized gas with long-slit spectroscopy (Tomita, Ohta & Saito 1994; Martin 1998) mostly focused on the filamentary structures. Our position–velocity diagram is compatible with the H I rotation curve of Stil & Israel (2002) that does not show any clearly rising part until 50 arcsec radius.

(x) *UGC 3334 (NGC 1961, Arp 184)*. NGC 1961 is a very bright and massive distorted LINER 2 SAB(rs)b galaxy showing highly irregular outer spiral arms and a pathological disc (Arp 1966). It does not show any nearby companion and no clear double nucleus indicates a merger in progress. Nevertheless, NGC 1961 is the central member of the small group of nine galaxies located in the same velocity interval with a projected separation of 1 Mpc. Two long straight arms tangent to the north-following side of galaxy point towards an extended H I counterpart (Shostak et al. 1982). The amplitude of the WHISP velocity field (website) as well as the width of the H I profile at 20 per cent (∼700 km s^{-1} from the WHISP website and 690 km s^{-1} from Bottinelli et al. 1990) are fully compatible with the Hα velocity field amplitude. The overall resemblance between Hα velocity field and H I velocity field is pretty good within the optical disc taking into account the low spatial resolution in the H I data. However, Hα kinematics present perturbations all over the disc leading to an asymmetric and wavy rotation curve. The southern spiral arm and the knotty regions in the northern arm present unexpected velocities leading to a model of rotation curve with strong residuals for which it was necessary to constrain the inclination. Our rotation curve is in reasonable agreement with the rotation curve along the major-axis from Rubin et al. (1979) but our rotation curve is almost twice extended on the receding side. Rubin et al. (1979) claimed that NGC 1961, with its total mass greater than 10^{12} M$_{\odot}$, was the most massive spiral known. Due to the uncertainties on the inclination and to waves in the rotation curve, the maximum rotation velocity (377 ± 85 km s^{-1}) could even be higher. From their optically derived spectra, they concluded to unexplained motions within the system. The Hα lines continuously display a double profile (not resolved by Rubin et al. 1979) from the centre to the outermost points of the approaching side (as it can be seen in the Hα position–velocity diagram, the most external velocities reach, respectively, ∼3500 and 3720 km s^{-1}). The maximum velocity has been chosen as the mean external velocity. These double profiles in the disc are an additional evidence for the complex history of this galaxy (merging, interaction, stripping) which still needs to be modelled taking into account its disturbed and asymmetric H I distribution and X-ray emission.

(xi) *UGC 3382*. This early-type SBa galaxy presents a lack of Hα emission at the centre, we thus miss the inner part of the velocity field within the first 3 kpc. Due to faint Hα signal-to-noise ratio in the rest of the disc, our rotation curve is based on a limited number of velocity bins. Despite of this, both sides of the rotation curve agree fairly well. We excluded from the analysis the outermost part of the approaching side because it has no counterpart on the receding side. An inner velocity gradient is well seen in the H I position–velocity diagram (Noordermeer et al. 2005), not in the Hα one. Their diagram shows that the rotation curve rises steeply at the centre and suggests that the maximum velocity is rapidly reached, at about 1 arcmin. The amplitude of the H I velocities is in good agreement with that of our Hα velocity field, suggesting that we actually reach the maximum rotation velocity within the optical radius, at the end of our Hα rotation curve. The morphological and Hα kinematical inclinations are the same ($21°$), while $16°$ is found from H I data.

(xii) *UGC 3463 (KIG 168)*. Our Hα map is in agreement with James et al. (2004) but suffers from bad seeing conditions leading to the confusion of several H II regions. Our rotation curve shows a bump at $\sim$10 arcsec likely due to a bar. No H I rotation curve is available. The width of the H I profile at 20 per cent ($341\,\mathrm{km\,s^{-1}}$ from Springob et al. 2005 and $334\,\mathrm{km\,s^{-1}}$ from Bottinelli et al. 1990) is in agreement with the amplitude of our Hα velocity field, confirming that the maximum velocity is reached before the optical radius $D_{25}/2$.

(xiii) *UGC 3521*. The Hα rotation curve is poorly defined at the centre because of the faint Hα emission. It rises slowly up to $\sim$165 $\mathrm{km\,s^{-1}}$ and extends up to about two-third of the optical radius ($D_{25}/2$) without being certain to reach the maximum rotation velocity. No H I rotation curve is available but the width of the H I profile at 20 per cent ($381\,\mathrm{km\,s^{-1}}$ from Springob et al. 2005) is higher (by $\sim$50 $\mathrm{km\,s^{-1}}$) than that of our Hα velocity field, suggesting that the plateau is almost reached but not yet.

(xiv) *UGC 3528*. The Hα emission is faint. It is sufficient, however, to derive a rotation curve apparently reaching a maximum although it barely reaches half the optical radius. The width of the H I profile at 20 per cent ($344\,\mathrm{km\,s^{-1}}$ from Springob et al. 2005) is in good agreement with the amplitude of our Hα velocity field, confirming that we do reach the maximum rotation velocity ($D_{25}/2$).

(xv) *UGC 3618 (NGC2308)*. No Hα emission is detected thus no image is displayed.

(xvi) *UGC 3685*. Flocculent SBb galaxy whose bar terminates at a well-defined circular ring. The bar is aligned with the kinematic major-axis and there is no clear signature of it in the Hα velocity field although a bump can be seen in the Hα rotation curve at about 1 kpc. Hα emission is mainly seen in a wide ring and in short spiral arms. No Hα emission can be seen at the centre except along the bar, in agreement with the James et al. (2004) Hα image, but we miss some faint emitting region to the south-east. As seen in the position–velocity diagram, a large velocity dispersion is observed in the nucleus of the galaxy. The photometric inclination is $55°$ from HyperLeda, $32°$ from NED and $33°$ from James et al. (2004). We agree with James et al. (2004) measurement, but we may estimate the uncertainty at $\sim$10°. Furthermore, if we take into account the very faint outer arms, the disc is rounder. On the other hand, the H I disc, which is about five times more extended than the optical one, is rather circular. It is possible that the inclination should vary with the radius, this should be done on the H I data (not yet published). Moreover, the Hα ring is also almost circular. This probably means that the inclination of the galaxy may still be lower. We fit a kinematical inclination of $12° \pm 16°$. Within the error bars, the kinematical

inclination is compatible with the morphological one ($\sim$33° $\pm$ 10°). The rotation curve rises rapidly within the first 2 kpc as expected for early-type galaxies despite the fact that the bar, aligned with the kinematical major-axis, should lower the inner gradient (Hernandez et al., in preparation). If we exclude this inner structure, the rotation curve seems to grow with a solid body behaviour. The outermost Hα regions disconnected from the main body of the disc extend beyond the optical radius $D_{25}/2$. The amplitude of the WHISP velocity field (website) as well as the width of the H I profile at 20 per cent ($\sim$100 $\mathrm{km\,s^{-1}}$ from the WHISP website, 118 $\mathrm{km\,s^{-1}}$ from Springob et al. 2005 and 103 $\mathrm{km\,s^{-1}}$ from Bottinelli et al. 1990) are almost twice the Hα velocity field amplitude. Moreover, regarding the H I velocity gradient, slowly growing up to the H I outskirts, our Hα rotation curve probably does not reach the maximum velocity.

(xvii) *UGC 3708 (NGC 2341)*. It forms a pair with UGC 3709. Its Hα distribution is asymmetric, brighter on the eastern side. Our Hα velocity field suggests an inclination of $44° \pm 16°$, higher than the photometric inclination ($16° \pm 24°$) but compatible with the error bars. No H I velocity field is available. The width of the H I profile at 20 per cent ($324\,\mathrm{km\,s^{-1}}$, Bottinelli et al. 1990) is in agreement with our Hα velocity field amplitude, confirming that we reach the maximum rotation velocity.

(xviii) *UGC 3709 (NGC 2342)*. It forms a pair with UGC 3708. The Hα rotation curve reaches a plateau with a lower maximum rotation velocity than the one given by Karachentsev & Myneva (1984b), around 250 $\mathrm{km\,s^{-1}}$ instead of 292 $\mathrm{km\,s^{-1}}$. No H I velocity field is available. The width of the H I profile at 20 per cent ($396\,\mathrm{km\,s^{-1}}$, Bottinelli et al. 1990) is in agreement with our Hα velocity field amplitude, confirming that the maximum velocity is reached.

(xix) *UGC 3826 (KIG 188)*. It has a faint Hα emission, in agreement with the map presented by James et al. (2004). The rising part of the Hα rotation curve is ill-defined, but a plateau seems to be reached within the optical radius. The H I velocity field (WHISP website) shows a velocity amplitude in agreement with our Hα velocity field and gives the same overall orientation for the major-axis PA. However, the pattern of the H I isovelocity lines in the central part points at a quite different orientation compared with that suggested by our Hα velocity field. The width of the H I profile at 20 per cent given by Springob et al. (2005) ($101\,\mathrm{km\,s^{-1}}$) is significantly larger than the amplitude of our velocity field (almost double) and seems abnormally large when compared with the H I profile obtained by WHISP (website).

(xx) *UGC 3740 (NGC 2276, Arp 25)*. Its spiral pattern is unusual, perhaps because of a tidal encounter with the probable companion NGC 2300 (Karachentsev 1972) or more likely, due to tidal stripping. Indeed, it is a member of a group where stripping has been evidenced (Rasmussen, Ponman & Mulchaey 2006). The western side of our Hα image and the velocity field show compression due to stripping by the intragroup medium. Our Hα data also reveal low surface brightness filaments extending towards the east, in agreement with James et al. (2004). Our Hα rotation curve is very peculiar and asymmetric. A steep velocity rise is observed in the galaxy core. The width of the H I profile at 20 per cent ($167\,\mathrm{km\,s^{-1}}$ from Springob et al. 2005) is slightly larger than our Hα velocity field amplitude. Nevertheless, the shape of our Hα rotation curve suggests that the maximum is reached just after the optical radius ($D_{25}/2$). The CO emission (Elfhag et al. 1996) is distributed in a lopsided fashion, with more emission towards the north-western region.

(xxi) *UGC 3876 (KIG 193)*. Diffuse Hα emission can be seen all over the disc, in agreement with James et al. (2004). The Hα

rotation curve rises slowly beyond the optical radius ($D_{25}/2$) so that we are not sure to reach the maximum rotation velocity. No H I velocity field is available. However, the width of the H I profile at 20 per cent (208 km s^{-1}, Bottinelli et al. 1990) is in good agreement with our Hα velocity field amplitude, suggesting that the maximum rotation velocity is effectively reached with our Hα rotation curve.

(xxii) *UGC 3915.* Strong Hα emission can be seen all over the disc. Our Hα rotation curve rises steeply and reaches a plateau around 200 km s^{-1} at about $0.5D_{25}/2$. No strong signature of the bar (aligned with the major-axis) can be seen in our velocity field. A small bump, seen in our rotation curve in the 5 inner arcsec, could be due to the bar. No H I velocity field is available in the literature. The width of the H I profile at 20 per cent (323 km s^{-1}, Bottinelli et al. 1990) is in agreement with our Hα velocity field amplitude.

(xxiii) *IC 476.* We detected some Hα emission in IC 476, the small companion of UGC 402 (both observed in the same field-of-view). We derive its rotation curve up to about $0.5D_{25}/2$; thus, it is not sure that the maximum rotation velocity is reached. No H I data are available in the literature.

(xxiv) *UGC 4026 (NGC 2449).* We detected faint Hα emission in the low surface brightness galaxy UGC 4026. However, its Hα emission is sufficient to derive with confidence a rotation curve up to about $0.5D_{25}/2$. As it seems that we observe the plateau of the rotation curve, the maximum velocity may be reached. A kinematical inclination of $56° \pm 4°$ has been computed, lower than the morphological one of $73° \pm 4°$. The kinematical inclination is very uncertain due to the very low signal-to-noise ratio of our Hα data. No H I data are available in the literature.

(xxv) *UGC 4165 (NGC 2500, KIG 224).* This galaxy belongs to a quartet of galaxies (Sandage & Bedke 1994). Diffuse Hα emission is observed in our Hα map, in agreement with James et al. (2004). Its short bar is almost aligned with its minor kinematical axis. Within the error bar, a good agreement is observed between the kinematical and morphological inclination. Our Hα velocity field is in very good agreement with the WHISP data (website). The width of the H I profile at 20 per cent (101 km s^{-1} from Springob et al. 2005, 114 km s^{-1} from Bottinelli et al. 1990 and 100.9 km s^{-1} from Haynes et al. 1998) is in agreement with our Hα velocity field amplitude.

(xxvi) *UGC 4256 (NGC 2532, KIG 232).* It presents patchy Hα emission along its spiral arms. The general pattern of the Hα velocity field is in good agreement with the H I velocity field (WHISP website). The PA of the kinematical major-axis of the Hα velocity field (116°) is in agreement with the H I one, but is very different from the value given in HyperLeda (26°) and in the RC3 (10°) as already noted by Marquez & Moles (1996). Indeed it is clear that the outermost contours of the galaxy measured from broadband imaging are elongated along the minor kinematical axis. Furthermore, morphological and kinematical inclinations are determined using PAs separated by 90°. Nevertheless, the H I disc is elongated along its kinematical major-axis, leading to an inclination ~30°. Our Hα rotation curve rapidly reaches a plateau climbing up to a maximum velocity ~100 km s^{-1} around the optical radius ($D_{25}/2$) in agreement with Marquez & Moles (1996) from Hα slit spectroscopy.

(xxvii) *UGC 4393 (KIG 250).* A strong Hα emission can be seen along the bar (aligned with the kinematical major-axis) and in the southwestern spiral arm, in agreement with James et al. (2004) Hα map. Due to the bar, the Hα velocity field is strongly perturbed at the centre. As a consequence, the Hα rotation curve is strongly perturbed, with counter-rotation motions at the centre. No H I velocity field is available in the literature. The H I width at 20 per cent (160 km s^{-1} from Springob et al. 2005) is more than

twice our Hα velocity field amplitude (70 km s^{-1}). This means that the maximum velocity is not reached in Hα. Moreover, due to the presence of the strong bar, the inclination is probably overestimated. Indeed, the external axial ratio of the outermost isophotes leads to an inclination around 35°. However, even with this lower value of inclination, the H I maximum rotation velocity remains slightly lower than expected for such a galaxy, according to the Tully–Fisher relationship.

(xxviii) *UGC 4422 (NGC 2595).* Located in the Cancer cluster, this barred spiral exhibits a prominent nucleus and distorted outer regions extending up to 70 arcsec (~18 kpc). Hα emission is observed at the centre, in the ring and in the beginning of the bar, in agreement with Gavazzi et al. (1998). Our rotation curve rapidly rises and reaches a plateau at almost 350 km s^{-1} in the innermost 5 arcsec. The shape of the rotation curve is consistent with the Fabry–Perot observations from Amram et al. (1992) and we derive the same set of parameters within the uncertainties. There is a strong discrepancy between the photometric (49° ± 4°) and kinematic inclination (25° ± 8°). No H I velocity map is available. The corrected H I profile width of 321 km s^{-1} from Springob et al. (2005) is in agreement with our Hα velocity field amplitude.

(xxix) *UGC 4456 (KIG 260).* A difference of 82° is observed between the kinematical and morphological major-axis PAs. This difference is due to its low inclination leading to an uncertain morphological determination. Within the error bar, a good agreement is observed between the kinematical and morphological inclinations. No H I velocity map is available. The width of the H I profile at 20 per cent (110 km s^{-1} from Bottinelli et al. 1990 and 105 km s^{-1} from Lewis et al. 1987) is larger than our Hα velocity field amplitude although our Hα rotation curve rapidly reaches a plateau extending well beyond the optical limit.

(xxx) *UGC 4555 (NGC 2649, KIG 281).* No H I velocity map is available. The width of the H I profile at 20 per cent (251 km s^{-1} from Bottinelli et al. 1990 and 256 km s^{-1} from Lewis et al. 1987) is in agreement with our Hα velocity field amplitude.

(xxxi) *UGC 4770 (NGC 2746).* In agreement with its morphological type (SBa), it shows a weak and asymmetric Hα emission. In particular, no Hα is detected within the bar. The Hα position–velocity diagram and rotation curve are badly defined due to faint signal-to-noise ratio in the data, especially on the receding side. The maximum velocity $V_{CO} = 207$ km s^{-1} deduced from the molecular component (Sauty et al. 2003) is in agreement with our Hα velocity field amplitude. No H I velocity map is available. The width of the H I profile at 20 per cent (264 km s^{-1} from Bottinelli et al. 1990 and 270 km s^{-1} from Lewis et al. 1987) suggests that Hα and the CO rotation curves do not reach the maximum velocity.

(xxxii) *UGC 4820 (NGC 2775, KIG 309).* Hα imaging from Hameed & Devereux (2005) is comparable with our data, showing a flocculent ring of Hα emission. Stellar dynamics from Kregel, van der Kruit & Freeman (2005) suggest a maximum velocity of 283 km s^{-1} lower than that suggested by the Hα kinematics. No H I velocity map is available in the literature. The width of the H I profile at 20 per cent (435 km s^{-1} from Bottinelli et al. 1990) is in agreement with our Hα velocity field amplitude.

(xxxiii) *UGC 5045.* It is a triple-arm barred galaxy that suffers from global distortion and shows ultraviolet (UV) excess (KISO survey, Takase & Miyauchi-Isobe 1991). Its arms are knotty with many H II regions distributed asymmetrically in the disc and no Hα emission is detected in the very centre. The rising part of our Hα rotation curve is thus missing and the curve looks like a plateau around 400 km s^{-1}, which seems quite high for such an Sc-type

galaxy. Indeed, our Hα velocity field suggests a faint inclination (17° only, with an uncertainty of 10°), whereas the photometry suggests 41° ± 4° (HyperLeda). Adopting this last value would lower the plateau of our rotation curve around a more normal value of 200 km s^{-1}, thus casting a doubt on the inclination deduced from our kinematics. No H I velocity map is available but the width of the H I profile at 20 per cent (200 km s^{-1}, Springob et al. 2005) is in agreement with our Hα velocity field amplitude. Taking into account the methodology used, and the fact that the velocity field which presents a good signal-to-noise ratio is not strongly disturbed (no bar, symmetric rotation curve), we adopt the kinematic inclination.

(xxxiv) *UGC 5175 (NGC 2977, KIG 363)*. This galaxy shows a strong Hα emission. Our Hα rotation curve is flat, with a plateau at ∼190 km s^{-1}, suggesting a maximum velocity rotation lower than that found by Karachentsev & Mineva (1984a) in the optical. It has been observed in CO by Sauty et al. (2003) who find a linewidth at 50 per cent of 312 km s^{-1}. No H I velocity map is available but the linewidth at 20 per cent of 356 km s^{-1} (Theureau et al. 1998) is comparable with our Hα velocity field amplitude.

(xxxv) *UGC 5228*. The Hα rotation curve of this strong Hα emitter, rises up to a plateau at ∼125 km s^{-1}. The H I linewidth of ∼270 km s^{-1} measured by Doyle et al. (2005) is in good agreement with our Hα velocity field amplitude.

(xxxvi) *UGC 5251 (NGC 3003)*. As already noted by Rossa & Dettmar (2003), except in the nucleus and in several bright H II regions, the Hα emission is rather faint and its distribution asymmetric, like the spiral arms of the galaxy. Such an asymmetry suggests that this galaxy may be disturbed by a dwarf companion. The velocity field is also rather asymmetric. No H I velocity field is available. The width of the H I profile at 20 per cent (305 km s^{-1} from Springob et al. 2005 and 289 km s^{-1} from Bottinelli et al. 1990) is slightly higher (by ∼30 km s^{-1}) than the velocity amplitude of our Hα velocity field. Thus, the maximum rotation velocity is probably not reached with our Hα rotation curve.

(xxxvii) *UGC 5279 (NGC 3026, KIG 377)*. No H I velocity field is available. The width of the H I profile at 20 per cent (∼220 km s^{-1}, Bottinelli et al. 1990) is lower than our Hα velocity field amplitude, suggesting that the maximum velocity is reached in our Hα position–velocity diagram.

(xxxviii) *UGC 5319 (NGC 3061, KIG 382)*. Its bar, almost aligned with the major-axis, shows no significant signature in our Hα velocity field. Our Hα rotation curve shows an inclined plateau, continuously rising within the optical limits. The steep rising in the first kpc of the rotation curve for this relatively low mass galaxy may be the signature of a bar. No H I velocity field is available but the width of the H I profile at 20 per cent (233 km s^{-1} from Springob et al. 2005 and 272 km s^{-1} from Lang et al. 2003, HIJASS survey) is significantly higher than the amplitude of our Hα velocity field (∼180 km s^{-1}). However, the corrected velocity from Springob et al. (2005) is about 198 km s^{-1} and the width of the H I profile at 50 per cent from Lang et al. (2003) is 189 km s^{-1} which is in better agreement. This disagreement between H I and Hα data could indicate that the galaxy is embedded in an H I complex extending much farther out than the optical limit.

(xxxix) *UGC 5351 (NGC 3067)*. This galaxy has been studied in the optical by Rubin, Thonnard & Ford (1982), the PA of the major-axis and the outer velocity gradients agree with both sets of data. Taking into account the difference in distance adopted for that galaxy (28.3 versus 19.3 Mpc), the extensions of the rotation curves agree. The rotation curve in the inner parts from stellar kinematics (Héraudeau et al. 1999) is in very good agreement with the inner part of the Hα position–velocity diagram. The full-resolution H I velocity field (WHISP, Noordermeer et al. 2005) is still too low and does not allow a straightforward comparison with the Hα. In particular the bar is not seen in H I, while the signature of the bar is clearly seen in the inner region of the Hα velocity field. The H I and Hα velocity amplitudes and gas extension are similar but their behaviour along the major-axis seems different. The Hα position–velocity diagram suggests that a constant velocity is reached after radius ∼5 arcsec, whereas the H I position–velocity diagram does not show such a plateau. The outermost isophotes of the *HST* image (Carollo, Stiavelli & Mack 1998) suggest an almost edge-on galaxy. Due to its high inclination, to avoid contamination due to the thickness of the disc (outer regions along the minor-axis), we have fixed the inclination to 82° from the morphology. The maximum rotation velocity has been computed taking into account this inclination and no rotation curve has been plotted.

(xl) *UGC 5373 (Sextans B, KIG 388)*. This dwarf galaxy is part of the Local Group. Our Hα map is in good agreement with the Hα maps from Hunter & Elmegreen (2004) and James et al. (2004). The Hα velocity field presents a low amplitude velocity gradient (∼30 km s^{-1}) barely visible in the position–velocity diagram. Both major-axis orientation and inclination are difficult to determine; nevertheless, the kinematical major-axis seems to be quite different (∼30°) from the photometric major-axis probably due to non-circular motions. The Hα rotation curve is ill-defined in the central part, with a possible counter-rotation within 15 arcsec from the centre, but rises rapidly beyond 30 arcsec and seems to reach a plateau at about 50 arcsec, in agreement with the H I data from Hoffman et al. (1996) who miss the rising part because of their poor resolution (and possibly lack of H I at the centre). We also agree that this galaxy is almost face-on (from the kinematics we find 10°, with an uncertainty of 18° and (Hoffman et al. 1996) find 18°), whereas the photometry suggests 60° (HyperLeda). However, our very low inclination value may lead us to overestimate the rotation velocities.

(xli) *UGC 5398 (NGC 3077)*. As a member of the M81 group of galaxies it is strongly disrupted by the interaction with M81 and M82. As shown by Walter et al. (2002), its optical image is offset with respect to a prominent H I tidal arm lying at about 4 arcmin east of the galaxy. Our Hα map is in good agreement with the one from James et al. (2004). The Hα velocity field shows no evidence for rotation, although some velocity gradient can be seen at the edges of the disc, with the lowest velocities observed on the western side (in agreement with Walter et al. 2002 observations, in H I, Hα and CO). No Hα rotation curve could be derived from our data as one can see it in the velocity field and in the position–velocity diagram.

(xlii) *IC 2542 (KIG 399)*. Kinematic and photometric data lead to a major-axis PA in good agreement but a difference of 20° is observed on the inclination; nevertheless, the difference in the inclination is compatible with the error bars. Our Hα rotation curve seems to reach a plateau at almost 300 km s^{-1} within the optical radius ($D_{25}/2$). No H I data are available in the literature.

(xliii) *UGC 5510 (NGC 3162, NGC 3575)*. Our Hα rotation curve seems to reach a plateau just before the optical radius ($D_{25}/2$) although the velocities for the receding side are still increasing beyond. No H I velocity field is available. The width of the H I profile at 20 per cent (204 km s^{-1} from van Driel et al. 2001 and 187 km s^{-1} from Bottinelli et al. 1990) is in agreement with our Hα velocity field.

(xliv) *UGC 5532 (NGC 3147)*. The Hα emission is very weak in the nuclear region and does not allow us to plot the rising part of the Hα rotation curve which rapidly reaches (within 1 kpc) a slightly decreasing plateau starting at almost 400 km s^{-1}. No H I

velocity map is available. The width of the H I profile at 20 per cent (455 km s^{-1} from Richter & Huchtmeier 1991, and 403 km s^{-1} from Lang et al. 2003) is in agreement with our Hα velocity field.

(xlv) *UGC 5556 (NGC 3187, Arp 316, HCG 44D)*. It is a member of the famous compact group HCG 44 (Hickson, Kindl & Auman 1989) strongly interacting with NGC 3190 (Sandage & Bedke 1994). Hα emission is only observed along the lenticular central region (the bar) and in the inner arms. The arms are obviously driven by streaming motions due to the interaction with its companion. The PA of the kinematical major-axis of the galaxy is almost perpendicular to the bar. Thus, the velocity field traces the kinematics of the bar and of the streaming motions in the arms but not the kinematics of the disc. Furthermore, we cannot compute a rotation curve. The velocity amplitude perpendicular to the bar across the velocity field is ∼150 km s^{-1}, lower than the width of the H I profile at 20 per cent (296 km s^{-1} from van Driel et al. 2001 and 257 km s^{-1} from Bottinelli et al. 1990).

(xlvi) *UGC 5786 (NGC 3310, Arp 217)*. The unusual smooth outer plume on the western side of the galaxy is probably the result of a recent merger (Balick & Heckman 1981). The plume has a smaller radial velocity than the galaxy. Wehner & Gallagher (2005) evidenced a closed loop in the *V* and *R* band that may be tidal debris. Diffuse Hα emission, not visible by James et al. (2004), is detected in our Hα image all around the galaxy. A large portion of the star formation is located in a central ring surrounding an off-centred nucleus. The central region of the Hα velocity field displays an S-shape pattern encircling two velocity peaks leading to two severe bumps in the rotation curve. The bright nucleus exhibits a steep velocity rise. Outside the nuclear region, the velocity decreases and then remains flat along the galaxy major-axis. Despite the evidence for perturbations, the rotation curve is fairly symmetric although showing some oscillations. Outflows are observed in the central region of the galaxy (∼1 kpc) by Schwartz et al. (2006) where we measure large Hα linewidths. The width of the H I profile at 20 per cent (330 km s^{-1} from Springob et al. 2005) is significantly larger than the amplitude of our Hα velocity field, suggesting that we cannot reach the maximum rotation velocity with our Hα data. Indeed, our Hα rotation curve clearly reaches a maximum at about 120 km s^{-1} with its central bump at 0.5 kpc but the behaviour of the curve in the outer parts is too chaotic (with a total divergence between receding and approaching side beyond the optical limit) for concluding anything about the true maximum. The kinematical inclination has been determined by excluding the central spiral structure within the first kpc, leading to a rather high inclination of 53° ± 11°. This is significantly higher than the morphological inclination of 16° ± 25° (HyperLeda) but the difference remains compatible with the error bars. We finally choose the kinematical inclination.

(xlvii) *UGC 5840 (NGC 3344, KIG 435)*. The Hα map is in agreement with Knapen et al. (2004); however, we miss the outermost parts of the galaxy because of our field-of-view (limited to a 4 arcmin diameter in that case because of the use of a 2 inches circular filter). Also, the warp observed in H I (WHISP website) cannot be seen within our field-of-view. Despite the fact that this ringed spiral galaxy is fairly regular, the velocity field is not at all symmetric with respect to the minor-axis. The nuclear region shows a large velocity dispersion, as seen in the position–velocity diagram diagram. The Hα rotation curve exhibits a valley where the main spiral structure vanishes in the optical. The width of the H I profile at 20 per cent (166 km s^{-1} from Bottinelli et al. 1990) is in agreement with the amplitude of our Hα velocity field. The maximum velocity

found in our Hα rotation curve is rather high for such a small galaxy ($D_{25}/2\sim$ 6 kpc) of Sbc type.

(xlviii) *UGC 5842 (NGC 3346, KIG 436)*. The Hα emission seems relatively poor on the receding side because the interference filter we have used was not perfectly centred on the galaxy. Nevertheless, we were able to derive a quite acceptable rotation curve. The high dispersion of our rotation velocities at the centre is probably due to the bar, then (from 1 to 6 kpc) our rotation curve is slowly rising like a solid body. No H I velocity field is available. The width of the H I profile at 20 per cent (166 km s^{-1} from Bottinelli et al. 1990 and ∼180 km s^{-1} from Tift & Cocke 1988) is in agreement with our Hα velocity field suggesting that the maximum rotation velocity is reached. We conclude that a plateau (if any) must begin just beyond the optical radius ($D_{25}/2$) where our Hα rotation curve ends after an almost continuously rising tendency.

(xlix) *UGC 6118 (NGC 3504)*. This early-type galaxy presents an almost circular outer ring, and a thin bar (more visible in *JHK* band from NED) embedded in a rather oval structure (axial ratio ∼0.5). A bulge is visible in the near infrared images. The agreement between our Hα map and the one from Hameed & Devereux (2005) is very good. The main bar has a size ∼1.2 arcmin. A secondary bar may be suspected in the first ∼20 arcsec around the very bright Hα nuclei. An Hα spiral structure is observed within the oval structure starting at the end of the inner bar. We find the major kinematical axis to be almost parallel to the bar and the oval structure. Our Hα velocity field is almost limited to the central oval structure and the bar, with only a few points in the outer ring. A steep inner rise of the velocities is observed in the galaxy core, otherwise the Hα velocities remain roughly constant before 45 arcsec, radius beyond which they begin to increase slightly. This is not observed in the H I position–velocity diagram from WHISP (Noordermeer et al. 2005), and the H I rotation curve slightly increases all along the first arcminute. Their H I velocity field perfectly covers the outer ring and leads to an inclination of 39°. The morphological inclination deduced from the outer ring is ∼27°,, while the inclination of the oval structure is ∼45°. The kinematical inclination of 52° deduced from our Hα velocity field is consistent with the inclination of the oval distortion. Nevertheless, we computed the rotation curve using the H I inclination because our kinematical inclination mainly relies on velocities measured within the central oval structure. The central region of the velocity field within the bar displays an S-shape pattern encircling two symmetric velocity peaks leading to two strong bumps on the rotation curve (at ∼0.5–1 kpc). Our Hα rotation curve is in good agreement with the long-slit observations of Usui, Saitō & Tomita (2001).

(l) *UGC 6277 (NGC 3596, KG 472)*. Except for the first central 15 arcsec, it is a low surface brightness galaxy displaying everywhere weak Hα emission. As a result, our Hα rotation curve seems to be limited to its rising part. Nevertheless, the velocity amplitude is in agreement with the H I profile of Kornreich et al. (2000), suggesting that our Hα rotation curve probably reaches the maximal rotation velocity despite its limited extent (about half the optical radius).

(li) *UGC 6419 (NGC 3664, Arp 05)*. It is one of the prototypical strongly barred magellanic spirals and has a nearby companion, UGC 6418, at 6.2 arcmin. H I Very Large Array (VLA) observations (Wilcots & Prescott 2004) show that the current interactions affect the morphology and the kinematics of the main galaxy. The H I velocity fields of both galaxies are connected, with a large extension (∼10 arcmin) compared with the optical one (∼1 arcmin). The PA of the major-axis of our Hα velocity field is almost perpendicular to the H I one. Indeed, the gradient of our Hα velocity field is almost

aligned along the bar, which cannot be seen in the H I data due to the low spatial resolution. It is therefore possible that our Hα rotation curve does not reflect the rotation of the galaxy but more probably the kinematics of the bar, likely to be affected by non-circular motions. Anyway, the shape of our rotation curve (solid body type) is not surprising for a galaxy of this type, but we find a rather low rotation velocity considering the luminosity of that galaxy. This suggests that the kinematical inclination (66°) as well as the inclination determined from the disc shape when excluding the tidal tail (57°) are too high. Indeed, the axial ratio of the disc including the tidal tail is close to one, suggesting that the galaxy is seen almost face-on. We conclude that the velocities of our Hα rotation curve are probably underestimated. Furthermore, the H I velocity field amplitude observed by Wilcots & Prescott (2004) ($\sim$150 km s^{-1}) is about twice ours ($\sim$70 km s^{-1}), suggesting that we do not reach the maximum of the rotation velocity.

(lii) *UGC 6521 (NGC 3719)*. No evidence for interaction with its companion, UGC 6523, can be seen in our Hα velocity field which is fairly symmetric. The resulting rotation curve is slightly decreasing beyond 6 kpc. No H I velocity field is available. The width of the H I profile at 20 per cent (397 km s^{-1}, Theureau et al. 1998) is somewhat higher than the amplitude of our Hα velocity field but the shape of our rotation curve leaves no doubt that the maximum is effectively reached within the optical limits.

(liii) *UGC 6523 (NGC 3720)*. Nearby companion of UGC 6521. The Hα emission is limited to the central regions (about one third the optical radius), thus our Hα rotation curve only shows the central rising part of the curve and no clear sign of interaction can be seen. No H I velocity field is available. The width of the H I profile at 20 per cent (393 km s^{-1} from Bottinelli et al. 1990) is much larger (more than three times) than our Hα velocity field amplitude, indicating that we are far from reaching the maximum of the rotation velocity.

(liv) *UGC 6787 (NGC 3898)*. Because of the interference filter used for this observation, which was not perfectly centred on the systemic velocity of the galaxy, the Hα emission from the eastern side was not transmitted through the filter (a good Hα image could be found in Pignatelli et al. 2001). As a consequence, our Hα rotation curve is only traced with the approaching side but seems acceptable anyway. It reaches a plateau within the optical radius ($D_{25}/2$) and seems to decrease beyond, in agreement with the H I data from WHISP (Noordermeer et al. 2005). However, the H I data suggest that the rotation curve climbs again beyond 2 arcmin to recover the same velocity level. Also, the steep inner rise of the velocities seen in the H I position–velocity diagram from WHISP is not detected in our Hα position–velocity diagram, which is probably due to a too low signal-to-noise ratio of the optical observations. The Hα velocities remain constant in the approaching half of the diagram, whereas the H I velocities increase in the same region.

(lv) *UGC 7021 (NGC 4045, NGC 4046)*. The Hα emission of this barely barred galaxy is found along the inner ring and at the centre. No diffuse Hα is detected otherwise in the disc, which is not surprising for an SAB(r)a galaxy. Our Hα map is very similar to the one found in GOLD Mine (Gavazzi et al. 2003). Because Hα emission is only detected in the very central area of the optical disc, we use the photometric inclination (56°) rather than the kinematical one (34°). Indeed the kinematical inclination is based only on the inner ring which is supposed to be circular, thus biasing the inclination determination. Our Hα rotation curve shows a slowly decreasing plateau starting at $\sim$220 km s^{-1} and $\sim$2 kpc, corresponding to the tip of the bar. The core of the galaxy exhibits two different velocity components, one at $\sim$1920 km s^{-1} and another one at $\sim$2000 km s^{-1}.

No H I velocity field is available. The width of the H I profile at 20 per cent (337 km s^{-1}, Springob et al. 2005) is in agreement with our Hα velocity field amplitude, confirming that we actually reach the maximum of the velocity rotation although our Hα rotation curve is far from reaching the optical radius ($D_{25}/2$).

(lvi) *UGC 7045 (NGC 4062)*. This galaxy is a strong Hα emitter, as already reported by James et al. (2004). A perfect agreement between photometric and kinematical parameters is observed. Slit spectroscopy observations using Hα and [N II] (Sofue et al. 1998) are compatible with ours, showing an Hα rotation curve that reaches a slowly rising plateau after about 20 arcsec. The position–velocity diagram derived in H I by Broeils & van Woerden (1994) is affected by beam smearing effects, since the inner part shows a solid body rotation up to almost 1.5 arcmin. At larger radii, however, the optical and radio data are compatible. The velocity dispersion in the central region of our Hα rotation curve is rather high, probably due to the bar. The linewidth of the H I profile at 20 per cent (309 km s^{-1}, Springob et al. 2005) is in good agreement with our Hα velocity field amplitude.

(lvii) *UGC 7154 (NGC 4145)*. This galaxy, having a bar embedded in a large elliptical bulge, is one of the principal galaxies in the Ursa Major Cluster paired with A1208+40 (Holm 342b) located at 13 arcmin. The Hα rotation curve beyond the optical radius ($D_{25}/2$) is mainly traced from emission regions of the spiral arms, leading to large wiggles in the rotation curve. The grand design of the WHISP H I velocity field (website) is compatible with the Hα one. The H I maximum rotation velocity of 171 km s^{-1} (Warmels 1988), assuming a 42° inclination, is compatible with our Hα value (about 150 km s^{-1} assuming a 65° inclination). Due to beam smearing effects, the inner velocity gradient in H I is nevertheless much lower than in Hα and the H I position–velocity diagram suggests a solid body rotation curve up to 2 arcmin from the centre.

(lviii) *UGC 7429 (NGC 4319)*. A very faint Hα emission has been detected in two spots for this spiral galaxy, companion of NGC 4291. This detection needs to be confirmed. No H I emission has been detected by Sengupta & Balasubramanyam (2006).

(lix) *UGC 7699*. No H I velocity field is available in the literature. The linewidth of the H I profile at 20 per cent (205 km s^{-1}, Broeils & van Woerden 1994) is in agreement with our Hα velocity field amplitude; their position–velocity diagram shows a solid body rotation having the same velocity amplitude as ours but the higher spatial resolution of the Hα velocity field enables us to observe deviations from a pure solid body rotation.

(lx) *UGC 7766 (NGC 4559)*. The bar of this galaxy is almost aligned with the major-axis; its signature can be seen on the velocity field as well as on the rotation curve within the first 30 arcsec. Meyssonnier (1984) obtained a rotation curve from slit spectroscopy which is in agreement, although it has a much higher dispersion than our Hα rotation curve. Our rotation curve is more extended since our velocity field reaches more outer regions although our field-of-view is limited by the size of the interference filter. Krumm & Salpeter (1979) found a flat H I rotation curve from 2 to 7 arcmin. It has been observed more recently by WHISP (website), their position–velocity diagram confirms the flat behaviour of the rotation curve up to 9 arcmin together with the amplitude determined by the previous authors. The width of the H I profile at 20 per cent (254 km s^{-1}, Springob et al. 2005) is in agreement with our Hα velocity field amplitude.

(lxi) *UGC 7831 (NGC 4605)*. Diffuse Hα emission is observed in the outer disc of this galaxy. Our Hα velocity field and rotation curve exhibit a strong asymmetry likely to be explained by the bar. Such an asymmetry is confirmed by the Hα +[N II] rotation curve

from Rubin et al. (1980) and by Sofue et al. (1998). An *I*-band image (XDSS) clearly provides the morphological centre of the galaxy and leads to the rotation curve presented here. On the other hand, the kinematical centre for this galaxy appears to be shifted by about 10 arcsec eastward from the morphological one but none of them leads to a symmetric inner rotation curve. The receding side of the rotation curve displays a plateau after 40 arcsec, following a solid body shape at the centre, while the approaching side is continuously climbing (note also that the receding side is less luminous than the approaching one). The method described in the paper leads to the rotation curve presented here because it minimizes the dispersion. Nevertheless, this solution is unphysical since it leads to negative rotation velocities for the receding side in the innermost region. To avoid this, the systemic velocity should be somewhat lowered by $\sim$20 km s^{-1}, leading to a worst disagreement between both sides of the rotation curve. Another solution would be to consider another rotation centre but it does not solve the asymmetry problem as explained above. This galaxy has been observed in H I by WHISP (website), their position–velocity diagram is asymmetric, in agreement with our Hα position–velocity diagram and rotation curve, and the H I velocity field suggests a warp in the outer parts of the disc.

(lxii) *UGC 7853 (NGC 4618, Arp 23)*. It forms a physical pair with UGC 7861 (NGC 4625). Assuming a distance for both galaxies of 8.9 Mpc (Moustakas & Kennicutt 2006), their physical separation is only $\sim$22 kpc (8.5 arcmin). Indeed, these galaxies show obvious signs of interaction (e.g. strong tidal unique tail for both galaxies). Its bar is not centred on the nucleus (Eskridge et al. 2002). Due to the strong southern arm, the morphological centre is offset from the kinematical one. The Hα rotation curve displays a solid body shape up to its end ($\sim$150 arcsec) suggesting that the maximum rotation velocity is probably not reached. The H I rotation curve (van Moorsel 1983) decreases beyond 3 arcmin from the centre (note, however, that their beam is larger than 1 arcmin). H I has been also observed by WHISP (website), their position–velocity diagram displays a solid body rotation curve up to $\sim$1.5 arcmin for the approaching side and a plateau beyond 1 arcmin for the receding side. Their low-resolution velocity field shows a severely warped disc (the PA of the major-axis rotates by 90° between the inner regions and the outermost parts of the H I disc). Taking into account the beam smearing effect, the agreement between the H I and our Hα position–velocity diagram and rotation curve is quite acceptable.

(lxiii) *UGC 7861 (NGC 4625)*. This galaxy is the companion of UGC 7853 (see notes above). Here agaat the centre of the galaxy is offset from the centre of the velocity field due to the strong southern tidal arm. Our Hα rotation curve shows a strong dispersion in the central part (up to 10 arcsec from the centre) then rises slowly as a solid body up to the optical limit (of about 40 arcsec) suggesting that the maximum rotation velocity is probably not reached. Fabry–Perot observations of this galaxy, with the 3.6-m CFHT, have been published by Daigle et al. (2006a), their velocity field and rotation curve are in good agreement with ours. H I has been observed by WHISP (website), their position–velocity diagram suggests a rotation curve with a plateau extending beyond the optical limit, from 1 up to 4 arcmin.

(lxiv) *UGC 7876 (NGC 4635)*. This isolated galaxy is a member of the Coma1 Cloud (according to GOLD Mine, Gavazzi et al. 2003). The Hα rotation curve is asymmetric and the fitting method probably led to an underestimation of the systemic velocity $\sim$10 km s^{-1}. This may be caused by the bar. Its CO emission is very faint (Sauty et al. 2003) and no H I velocity field is available but

the linewidth of the H I profile at 20 per cent (173 km s^{-1}, Springob et al. 2005) is in agreement with our Hα velocity field amplitude.

(lxv) *UGC 7901 (NGC 4651, Arp 189)*. Member of the Virgo cluster, it is a strong Hα emitter, particularly in an inner ring from where start the arms. A very good agreement is observed between our Hα map and the ones of James et al. (2004), Koopmann, Kenney & Young (2001), and GOLD Mine (Gavazzi et al. 2003). A faint signature of a bar can be seen in the inner regions of our Hα velocity field. Our Hα rotation curve is in good agreement with that observed by Rubin et al. (1999) from long-slit spectroscopy except that we do not observe the rising trend they observe for the outermost part of the receding side. Such a behaviour seems suspect, all the more since our Hα rotation curve is perfectly symmetric and extends farther out, owing to velocities collected far from the major-axis. No H I velocity map is available. The width of the H I profile at 20 per cent (395 km s^{-1}, Springob et al. 2005) is in agreement with our Hα velocity field amplitude.

(lxvi) *UGC 7985 (NGC 4713)*. Member of the Virgo cluster showing a strong Hα emission as shown by the same authors as for UGC 7901. The signature of a bar is seen in the inner part of our Hα velocity field within a radius of $\sim$30 arcsec. Our Hα rotation curve extends farther out than the rotation curve observed by Rubin et al. (1999), beyond the optical radius ($D_{25}/2$). Our rotation curve is fairly symmetric and does not show the strong decrease observed by Rubin et al. (1999) for the receding part around 40 arcsec. No H I velocity map is available but the H I linewidth at 20 per cent (217 km s^{-1}, Springob et al. 2005) is in agreement with our Hα velocity field amplitude.

(lxvii) *UGC 8334 (NGC 5055, M 63)*. M 63 is a very well studied flocculent spiral galaxy. Our observations are fully compatible with the Hα Fabry–Perot data observed with the 1.6-m Mont Megantic Telescope (Daigle et al. 2006a). Their rotation curve is more extended, due to a larger field-of-view, but does not reach the optical radius ($\sim$6 arcmin). It possesses a huge H I disc ($\sim$36 arcmin diameter) strongly warped beyond the optical disc (Battaglia et al. 2006). The agreement between our Hα rotation curve and their H I rotation curve is very good but we find a better symmetry for receding and approaching sides from 2 to 10 kpc radius. The position–velocity diagram shows that the velocities steeply rise in the inner 10 arcsec.

(lxviii) *UGC 8403 (NGC 5112)*. Paired with NGC 5107 at 13.5 arcmin, its Hα map shows a very good agreement with that of James et al. (2004). The signature of a weak bar is visible in the inner region of our Hα velocity field but it is difficult to see the signature of an interaction with its companion in its velocity field. An attempt of CO detection proved dubious (Braine et al. 1993). It has been observed in H I by Springob et al. (2005), and by WHISP (website). There is a good agreement between the WHISP velocity field and ours and our Hα emission is almost as extended as the H I disc. The shape of the H I position–velocity diagram found by WHISP is in very good agreement with our Hα position–velocity diagram and rotation curve. Also, the H I linewidth at 20 per cent (226 km s^{-1}, Springob et al. 2005) is in good agreement with our Hα velocity field amplitude.

(lxix) *NGC 5296*. This galaxy has no UGC number. It is the small companion of UGC 8709 (discussed hereafter). Our Hα map is deeper than the one by Rossa & Dettmar (2003) but nevertheless does not show any Hα emission in the tidal arms seen in their unsharped-mask *R*-band image, the emission being restricted to the central regions ($\sim$1/3$D_{25}/2$). As a consequence, our Hα rotation curve only shows the inner rising part. It is difficult to make a direct comparison with the rotation curve obtained by Rampazzo

et al. (1995) because they choose to align their slit in the direction of UGC 8709, which is about 30° different from the true major-axis. However, simulating a slit with their orientation along our Hα velocity field shows that our results are consistent. On the WHISP H I velocity field (website), one can hardly distinguish NGC 5296 close to UGC 8709, although it seems to appear as a point source in the average resolution map.

(lxx) *UGC 8709 (NGC 5297)*. It is the large companion of NGC 5296. Hα emission is detected in the northern arm but only in the beginning of the southern tidal arm, in agreement with Rossa & Dettmar (2003). The clear signature of a bar can be seen at the centre of the Hα velocity field. From the kinematics, we find an inclination (76° ± 1°) slightly smaller than the photometric one (82° ± 3°). It seems that the photometric inclination has been computed from the axial ratio of the disc including the tidal arms. The width of the H I profile at 20 per cent (418 km s^{-1} from van Driel et al. 2001, 413 km s^{-1} from Bottinelli et al. 1990) is in agreement with our Hα velocity field amplitude. The H I velocity field has been observed by WHISP (website) and is consistent with ours. The H I position–velocity diagram shows a slightly decreasing plateau beyond 1 arcmin, in agreement with our Hα rotation curve. The long-slit rotation curve observed by Rampazzo et al. (1995) also shows a decreasing trend in the outer parts. No CO has been detected in this galaxy (Elfhag et al. 1996).

(lxxi) *UGC 8852 (NGC 5376)*. This galaxy is included in a group together with UGC 8860 (NGC 5379) and UGC 8866 (NGC 5389). Strong Hα emission is seen, in particular in a ring located 15 arcsec from the centre. No H I velocity field is available. The width of the H I profile at 20 per cent (402 km s^{-1}, Theureau et al. 1998) is significantly higher than our Hα velocity field amplitude (~320 km s^{-1}). Since our Hα rotation curve is still rising in the outer parts, before we reach the optical radius, this suggests that the maximum velocity is not reached.

(lxxii) *UGC 8863 (NGC 5377)*. The detection of Hα emission in this early-type SBa galaxy is limited to two faint lobes at about 1 arcmin on each side of the disc. As a consequence our Hα rotation curve is reduced to two points (which nevertheless represent 34 independent bins, that is, about a thousand of pixels), one for the receding side and one for the approaching side and we only get a lower limit for the Hα maximum rotation velocity of ~190 km s^{-1}. Moreover, even if the signal-to-noise ratio does not allow to compute another velocity bin at the centre of the galaxy, the position–velocity diagram suggests a faint Hα emission (yellow spots) allowing us to measure a central gradient of ~40 km s^{-1} arcsec^{-1} (i.e. ~350 km s^{-1} kpc^{-1}). Due to beam smearing limitation, this strong gradient cannot be seen in the WHISP position–velocity diagram (Noordermeer et al. 2005). Indeed, the maximum velocity is reached at about 1 arcmin from the centre in H I data leading to a lower velocity gradient of ~3 km s^{-1} arcsec^{-1} (i.e. ~25 km s^{-1} kpc^{-1}). Our maximum velocity is probably close to the actual maximum velocity rotation since the width of the H I profile at 20 per cent (391 km s^{-1}) found by Noordermeer et al. (2005) is close to our Hα velocity field amplitude.

(lxxiii) *UGC 8898 and UGC 8900 (NGC 5394 and NGC 5395, Arp 84)*. The nuclei of this interacting pair of galaxies are separated by only 1.9 arcmin (~27 kpc). No Hα emission is detected in the tidal arms of UGC 8898, while Hα emission is more extended in UGC 8900, in agreement with Kaufman et al. (1999) from Fabry–Perot imaging. The photometric inclination for UGC 8898 is 70° ± 3°, quite different from our kinematical inclination (27° ± 20°) which is in fact based on the very central part only (about 15 arcsec diameter). Despite its limited extent, our Hα velocity

field of UGC 8898 clearly suggests a PA of the major-axis of 31°, differing by 66° from the one used by Márquez et al. (2002) for long-slit spectroscopy, which they confess is not adequate to elaborate the rotation curve. Indeed, they did not observe any clear rotation within the first 10 arcsec. Our Hα rotation curve extends only up to ~10 arcsec and we do not reach either a plateau or, probably, the maximum rotation velocity. Because our observations of UGC 8898 have been done through the edge of the transmission function of the interference filter, the spatial coverage of our data is smaller than that of Kaufman et al. (1999). They have also observed UGC 8898 in the CO line (Kaufman et al. 2002) and find a very good agreement between Hα and CO data. In agreement with the Fabry–Perot Hα velocity field of Kaufman et al. (1999), our Hα velocity field of UGC 8900 is not well enough defined to show straightforward evidence for interaction, except that the velocity field is uncompleted and the kinematical major-axis is shifted by 11° from the morphological one, which is a significant difference considering the high inclination of this galaxy. Márquez et al. (2002) have aligned the slit of their spectrograph almost along the morphological major-axis, explaining part of the differences between our rotation curves. Their rotation curve is slightly more extended but much more chaotic and asymmetric, with a markedly smaller velocity amplitude than ours. Both sides of our Hα rotation curve are fairly symmetric and show a slowly rising trend (almost solid body like between 20 and 60 arcsec) without ever reaching a plateau. Such a behaviour is unexpected for an Sa-type galaxy and could be due to the interaction with its companion. The kinematical and morphological inclinations of UGC 8900 are compatible within the error bars (they differ by only 9°). H I single dish observations cannot disentangle UGC 8898 from its companion UGC 8900 (van Driel et al. 2001; Theureau et al. 1998). The pair has also been observed in the H I by WHISP (website) and by Kaufman et al. (1999). Taking into account the lower H I spatial resolution, the H I and Hα kinematics are compatible, and the H I position–velocity diagram suggests that we actually reach the maximum of the rotation curve at the end of our Hα rotation curve.

(lxxiv) *UGC 8937 (NGC 5430)*. Our Hα map shows low-emission Hα regions that were not detected by García-Barreto et al. (1996). The signature of the strong central bar can be seen in our Hα velocity field (S-shape signature). Our rotation curve reaches a plateau within a few arcsec. A strong velocity gradient of ~300 km s^{-1} is observed between −5 and 5 arcsec, as can be seen in the position–velocity diagram. The H I linewidth at 20 per cent (371 km s^{-1} from Springob et al. 2005, 344 km s^{-1} from Theureau et al. 1998) is slightly smaller than the amplitude of our Hα velocity field (~400 km s^{-1}).

(lxxv) *UGC 9013 (NGC 5474)*. This late-type peculiar dwarf galaxy is the nearest companion of M101 (44 arcmin) and is tidally deformed into a very asymmetric and disturbed object. Our Hα velocity field cannot help us finding the rotation centre as it shows a solid body shape. Knapen et al. (2004) show an Hα map in good agreement with ours. The Hα rotation curve derived from long-slit spectroscopy data by Catinella, Haynes & Giovanelli (2005) cannot be compared directly with ours, because their centre has been chosen to be the 'pseudo-nucleus'. Several H I studies are available in the literature (Huchtmeier & Witzel 1979; van der Hulst & Huchtmeier 1979; Rownd, Dickey & Helou 1994; Kornreich et al. 2000). Kornreich et al. (2000) and Rownd et al. (1994) used the same data set from the VLA array (35-arcsec beam). The optical part of the galaxy is not affected by the severe warp seen in H I and the solid body rotation seen in Hα is compatible with H I data. These authors place the kinematical centre as the symmetry centre of the warp.

It is closer to the centre of the outermost optical isophotes than the 'pseudo-nucleus'. Rownd et al. (1994) assumed an inclination of 21° from a tilted ring model. Their PA of the major-axis at the centre (∼158°) is in agreement with ours but almost perpendicular to the photometric PA. Due to the presence of the strong tidal arm and the relative low spatial Hα coverage, the inclination and centre are in fact difficult to recover. That is why we preferred using the H I kinematical centre and inclination (21°) consistent with the external axial ratio of the outermost isophotes from the XDSS image. The strange behaviour of the resulting Hα rotation curve in the first 40 arcsec could be the signature of strong non-circular motions. We find a maximum velocity rotation ∼120 km s^{-1} at about 70 arcsec, significantly higher than the velocities found by Kornreich et al. (2000) even when assuming a very low inclination for the H I disc. Also the amplitude of our Hα velocity field is higher than the H I velocity field amplitude.

(lxxvi) *UGC 9179 (NGC 5585)*. It is a satellite of M101 (Sandage & Bedke 1994). A good agreement is observed between our Hα map and that of James et al. (2004); however, we miss an Hα region in the north-east because of our smaller field-of-view. The Hα rotation curve is perturbed, due to the presence of the bar and an inner arm-like structure. This galaxy has been observed in H I by Cote, Carignan & Sancisi (1991) who obtained a velocity field and a rotation curve in agreement with ours although their H I extent is larger and our Hα resolution higher. Our Hα rotation velocities are higher because we assume an inclination of 36° (derived from our Hα velocity field), whereas the H I data led to a higher inclination of 51°.5. Both values are nevertheless compatible within the Hα error bars. Although the shape of our Hα rotation curve suggests that we reach the maximum rotation velocity at the optical limit, the H I rotation curve from Cote et al. (1991) shows that the true maximum is reached a bit further.

(lxxvii) *UGC 9219 (NGC 5608)*. It has been observed in Hα by van Zee (2000) and James et al. (2004), their maps are in agreement with ours. Our Hα velocity field amplitude is nevertheless compatible with the H I linewidth at 20 per cent of 130 km s^{-1} from Bottinelli et al. (1990). No H I velocity map is available in the literature for this galaxy.

(lxxviii) *UGC 9248 (NGC 5622)*. The Hα emission is asymmetric and much brighter on the western side. Nevertheless, the resulting rotation curve is fairly symmetric and reaches a plateau within the optical limit. No H I velocity map is available in the literature but H I linewidth measurements at 20 per cent have been done and are compatible with our Hα velocity field amplitude although somewhat larger (357 km s^{-1} by Theureau et al. 1998, 349 km s^{-1} by Springob et al. 2005).

(lxxix) *UGC 9358 (NGC 5678)*. Márquez et al. (2002) derived a rotation curve from long-slit spectroscopy which is in good agreement with our Hα rotation curve, for both sides. However, since we adopted a slightly lower inclination, our velocities are slightly higher. Their rotation curve is more extended, but the dispersion of their points in the outer parts is quite high, especially on the receding side. Our Hα velocity field is perturbed and clearly shows the signature of a bar at the centre (S shape of the isovelocity lines). No H I velocity map is available in the literature but the width of the H I profile at 20 per cent (424 km s^{-1}, Springob et al. 2005) is in good agreement with our Hα velocity field amplitude.

(lxxx) *UGC 9363 (NGC 5668)*. Our observations are in agreement with previous Hα Fabry–Perot observations by Jiménez-Vicente & Battaner (2000). They adopted an inclination of 18° derived by Schulman et al. (1996) from a tilted ring model applied to VLA H I data. This inclination is lower than expected from morphology (33°). Our data confirm this tendency, explaining why morphological and kinematical major axes are found to be quite different (40°). Our kinematical estimate of the inclination is close to 0° and leads to unrealistically high rotational velocities. Thus, as Jiménez-Vicente & Battaner (2000), we fixed the inclination to the H I value of 18°. Schulman et al. (1996) H I data show a warp starting at 120 arcsec, which is the outermost limit of our Hα rotation curve. Indeed, it is possible that the outermost points of our Hα rotation curve are affected by this warp, since it shows a clear trend to increase from 80 to 120 arcsec, whereas the H I observations by Schulman et al. (1996) suggest that the plateau of the curve is already reached at 100 arcsec when correcting for the warp. The width of the H I profile at 20 per cent (122 km s^{-1}, Springob et al. 2005) is in agreement with our Hα velocity field amplitude.

(lxxxi) *UGC 9406 (NGC 5693)*. A short bright bar and an asymmetric disc (with one knotty arm) are observed. This galaxy is paired with UGC 9399 (NGC 5689) at 11.8 arcmin, which may explain the presence of a single arm. Poor Hα emission is detected and our Hα velocity field shows a strong dispersion, so that it is difficult to draw any reliable rotation curve from our data. The photometric inclination found in the literature varies from 33° (Vorontsov-Velyaminov & Krasnogorskaya 1994) to 51° (HyperLeda). Even when adopting the lowest value of inclination, we find a maximum rotation velocity which remains abnormally low considering the absolute magnitude of this galaxy, suggesting that our Hα velocity field is far from reaching the maximum velocity amplitude. Indeed the width of the H I profile at 20 per cent is 74 km s^{-1} (Bottinelli et al. 1990), whereas our Hα velocity field amplitude is smaller than 50 km s^{-1}. No H I velocity map is available for this galaxy in the literature.

(lxxxii) *UGC 9465 (NGC 5727)*. A good agreement is observed between our Hα map and that of James et al. (2004). No signature of the central bar can be seen in our Hα velocity field. It has been observed in H I by Pisano, Wilcots & Liu (2002) and their velocity field is in good agreement with ours. These authors adopted an inclination of 61° (close to the inclination of 65° we deduced from our Hα velocity field) and found a maximum rotation velocity of 93 km s^{-1} in good agreement with our Hα value (98 km s^{-1}). The inclination of 90° given in HyperLeda is certainly wrong because this galaxy seems far from being seen edge-on. The inclination deduced from our Hα velocity field exactly matches the value suggested by the axial ratio given in NED.

(lxxxiii) *UGC 9576 (NGC 5774)*. This galaxy is the companion of NGC 5775. There is a good agreement between our Hα map and that of James et al. (2004). Márquez et al. (2002) derived a rotation curve from long-slit spectroscopy. However, their slit was 20° away from the true kinematical major-axis, maybe explaining why their rotation curve is more chaotic than ours. Our Hα rotation curve is much more symmetric and extends farther out. The width of the H I profile at 20 per cent (280 km s^{-1}) from Springob et al. (2005) is almost twice our Hα velocity field amplitude, which is quite surprising since the shape of our Hα rotation curve suggests that we reach the maximum rotation velocity. The value given by Springob et al. (2005) seems nevertheless suspicious as Bottinelli et al. (1990) and Irwin (1994), respectively, found 152 and 179 km s^{-1} (uncorrected for galaxy inclination) for the width of the H I profile at 20 per cent, which is quite compatible with our Hα velocity field amplitude. The detailed H I velocity field of the pair NGC 5774–NGC 5775 has been observed at the VLA by Irwin (1994). Her velocity field and rotation curve for NGC 5774 are in good agreement with our Hα data and have about the same spatial extension. She used the

same method as ours to determine the kinematical parameters and they are in very good agreement with ours.

(lxxxiv) *UGC 9736 (NGC 5874)*. We detect poor and asymmetric Hα emission in that galaxy. Our Hα rotation curve is nevertheless fairly symmetric and almost reaches the optical limit, with a trend to flatten in its outermost parts. The width of the H I profile at 20 per cent (324 km s^{-1} from Springob et al. 2005, 315 km s^{-1} from Bottinelli et al. 1990) is in agreement with our Hα velocity field amplitude and suggests that we actually reach the maximum of the rotation curve. No H I velocity map is available in the literature.

(lxxxv) *UGC 9866 (NGC 5949)*. Comparing our Hα map with that of James et al. (2004) shows that our data suffer from bad seeing conditions leading to non-resolved H II regions. However, the Hα emission is strong enough so that we have a complete velocity field all over the disc. The Hα emission is asymmetric, stronger on the receding side (north-west). Our rotation curve is in very good agreement with the radial velocities measured by Karachentsev & Petit (1990) from slit spectroscopy when correcting for the inclination. Courteau (1997), also from slit spectroscopy, finds a slightly smaller extension for the rotation curve but the velocity width he measures from the flux-weighted rotation profile (213 km s^{-1}) is in agreement with our maximum velocity field amplitude. No H I velocity map is available but the width of the H I profile at 20 per cent (216 km s^{-1} from Springob et al. 2005, 197 km s^{-1} from Bottinelli et al. 1990) is also in good agreement with our Hα velocity field amplitude.

(lxxxvi) *UGC 9943 (NGC 5970)*. It forms a pair with IC 1131 at 8 arcmin. Hα emission is strong in particular in an inner ring. Our Hα rotation curve is in good agreement with the slit spectroscopy one of Márquez et al. (2002). A plateau is clearly reached around 3 kpc. No H I velocity map is available in the literature but the width of the H I profile at 20 per cent (338 km s^{-1} from Springob et al. 2005, 326 km s^{-1} from Bottinelli et al. 1990) is in good agreement with our Hα velocity field amplitude.

(lxxxvii) *UGC 10075 (NGC 6015)*. There is a good agreement between our Hα map and that of James et al. (2004). We detect, however, some faint emission in an outer spiral arm to the south-east that they do not detect. Our Hα rotation curve is in good agreement with the slit spectroscopy observations of Carozzi (1976) when correcting for the different inclinations adopted. However, her detection was not as good, and our rotation curve is almost twice more extended, clearly showing a slowly rising plateau beyond 50 arcsec radius. No H I velocity map is available in the literature but the width of the H I profile at 20 per cent (315 km s^{-1} from Springob et al. 2005, 310 km s^{-1} from Bottinelli et al. 1990) is in good agreement with our Hα velocity field amplitude. It has been observed in CO by Braine et al. (1993) who find a strong CO emission at 40 arcsec (2.7 kpc) from the centre.

(lxxxviii) *UGC 10521 (NGC 6207)*. There is a good agreement between our Hα map and that of James et al. (2004). Our Hα rotation curve is in good agreement with the slit spectroscopy observations by Carozzi (1976) (PA = 15°) and Márquez et al. (2002) (with PA = 22°) when correcting for the different inclinations adopted. No H I velocity map available in the literature but the width of the H I profile at 20 per cent (255 km s^{-1} from Springob et al. 2005, 240 km s^{-1} from Bottinelli et al. 1990) is in good agreement with our Hα velocity field amplitude.

(lxxxix) *UGC 10652 (NGC 6283)*. This galaxy is asymmetric, with some bright Hα spots and diffuse Hα emission all over the disc. An inner Hα ring, of some 7 arcsec radius, can be seen at the centre. The morphological inclination of 30° ± 7° is compatible, within the error bars, with the kinematical inclination (16° ± 12°)

deduced from our Hα velocity field. The position of the kinematical major-axis differs from the photometric one by 12°. Our Hα rotation curve seems to reach a plateau at about 2 kpc (23 arcsec) within the optical limit. No useful H I data are available in the literature for that galaxy.

(xc) *UGC 10713*. We adopted an inclination of 90° for that galaxy, otherwise our method led to a clearly wrong value below 70°, probably because of the odd pattern of our Hα velocity field at the centre. It has been observed in H I by WHISP (website) and their velocity field is in agreement with ours, but much more extended. Their H I position–velocity diagram suggests that the rotation curve reaches a plateau at about 1 arcmin radius, just beyond the limits of our Hα rotation curve which is limited to the solid body rising part. The H I linewidth at 20 per cent (268 km s^{-1} by Theureau et al. 1998 and 260 km s^{-1} by Springob et al. 2005) is in agreement with our Hα velocity field amplitude.

(xci) *UGC 10757*. This galaxy has a velocity of 1168 km s^{-1}. It is located in a triple subgroup with UGC 10762 (NGC 6340) an S0/a galaxy with a peculiar morphology with a series of tightly wound, almost circular, multiple-fragment, relatively thin outer arms surrounding a bulge and a lens at 6.4 arcmin and UGC 10769 which has an Sb pec morphological type located at 6.1 arcmin with a velocity of 1283 km s^{-1}. This system is clearly in interaction as shown by the H I cloud in which the three galaxies are embedded (e.g. WHISP website). This galaxy is asymmetric, with a brighter Hα emission at the beginning of the northern spiral arm, also seen in the optical (XDSS) and UV (GALEX) images. The WHISP H I velocity field corresponding to the optical extent of the galaxy (also coinciding with the brightest part of the H I complex) is in agreement with our Hα velocity field. However, the pattern of the whole extent of the H I velocity field is quite odd, apparently because of several galaxies interacting there. As a result, the width of the H I profile at 20 per cent found in the literature for that galaxy (283 km s^{-1} from Springob et al. 2005, 276 km s^{-1} from Lang et al. 2003, 222 km s^{-1} from Theureau et al. 1998) is larger than the amplitude of the Hα velocity field because a more extended region is embedded in the H I. The shape of the Hα rotation curve suggests that we are not far from reaching the maximum rotation velocity within the optical limit.

(xcii) *UGC 10769*. This galaxy has a diffuse disc and no spiral pattern visible. It has a higher velocity than the two other galaxies in the triple system (see UGC 10757 for a detailed discussion). We detect Hα emission only in the north-eastern edge of the disc so that no rotation curve can be derived. The secondary peak in the H I distribution corresponds to the same region where the Hα is detected.

(xciii) *UGC 10791*. This low surface brightness galaxy has two companions according to the WHISP website. We observe a faint diffuse Hα emission throughout the disc insufficient to determine unambiguously its inclination. This galaxy is classified face-on in HyperLeda; nevertheless, it does not look face-on in the XDSS image (see Fig. D93); in addition, the velocity field displays a clear rotation compatible with the H I velocity field (e.g. same PA and velocity amplitude in the central region). Thus, we fixed the inclination to the WHISP value of 34°. The Hα distribution extends only until half of the optical radius and thus does not reach the maximum rotation velocity observable in the H I [full width at half-maximum (FWHM): 199 km s^{-1} from Springob et al. 2005, 156 km s^{-1} from Theureau et al. 1998; amplitude of the WHISP velocity field of ∼150 km s^{-1}].

(xciv) *UGC 11012 (NGC 6503)*. This galaxy has a strong Hα emission all over its disc, with a faint extended feature on the

western edge (~2 arcmin from the centre). This faint extension cannot be seen in the Hα map from Strickland et al. (2004). Our rotation curve clearly reaches a plateau around 80 arcsec, well before the optical limit. Several optical rotation curves are found in the literature but none of them takes this extension into account and their extension is limited to ~80 arcsec, whereas ours extends up to 150 arcsec (for the receding side, owing to the mentioned Hα extension). Nevertheless, these rotation curves (de Vaucouleurs & Caulet 1982; Karachentsev & Petit 1990) are in very good agreement with our Hα rotation curve. Hβ observations made by Bottema (1989) also show a rotation curve in good agreement with ours. The H I map obtained by Begeman (1987) is more extended than our Hα map otherwise both velocity fields are in good agreement, as well as the derived rotation curves. The parameters computed in H I with a tilted ring model (PA = $-59°.4$, $i = 73°.8$) are in very good agreement with our own parameters.

(xcv) *UGC 11269 (NGC 6667).* Despite a short exposure time (~1 h), our Hα observations perfectly match James et al. (2004) Hα data who find faint patchy emission. It has been observed in H I by WHISP (Noordermeer et al. 2005) and their velocity field and rotation curve extend more than four times the optical radius. Our Hα position–velocity diagram does not show the steep velocity gradient observed in their H I position–velocity diagram in the innermost 40 arcsec due to a very noisy and patchy distribution of the ionized gas. The maximum rotation velocity is reached in Hα, as confirmed by the width of the H I profile at 20 per cent found by different authors (415 km s^{-1} from Noordermeer et al. 2005, 394 km s^{-1} from Springob et al. 2005, 406 km s^{-1} from Bottinelli et al. 1990). Our Hα data suggest that the maximum rotation velocity is reached within the first kpc instead of the first ~6 kpc as suggested by the H I data (Noordermeer et al. 2005).

(xcvi) *UGC 11300 (NGC 6689, NGC 6690).* This galaxy has been published in Paper IV. See specific comment at the end of this section.

(xcvii) *UGC 11332 (NGC 6654A).* There is a good agreement between our Hα map and that of James et al. (2004). However, our image is affected by very bad seeing conditions (see Table C2) resulting in a diffuse emission around the galaxy that is most probably an artefact. No H I velocity map is available in the literature. The width of the H I profile at 20 per cent (331 km s^{-1} from Springob et al. 2005, 315 km s^{-1} from Bottinelli et al. 1990) is significantly larger than our Hα velocity field amplitude (about 200 km s^{-1}), suggesting that our Hα velocity field does not reach the maximum rotation velocity although it extends up to the optical radius.

(xcviii) *UGC 11407 (NGC 6764).* The Hα emission is conspicuous along the bar and in the arms (particularly the northern arm). Our Hα rotation curve has been drawn using the photometric PA of the major-axis and the photometric inclination. It is much chaotic at the centre, up to 20 arcsec (probably because of the strong bar), and then looks on average like that of a solid body rotating disc, although it is markedly asymmetric. The central bar is almost aligned along the photometric major-axis and the H I velocity field derived from VLA observations (Wilcots, Turnbull & Brinks 2001) leads to the same PA. In the central parts, the isovelocity line patterns show the signature of the strong central bar on both Hα and H I velocity fields. The position–velocity diagram shows a steep velocity rise in the galaxy core. The width of the H I profile at 20 per cent (291 km s^{-1} from Springob et al. 2005, 293 km s^{-1} from Bottinelli et al. 1990, ~300 km s^{-1} from Wilcots et al. 2001) is in agreement with our Hα velocity field amplitude.

(xcix) *UGC 11466.* We detect a strong Hα emission along a bar-like feature. This galaxy has been observed in H I by WHISP (web-

site) and their high-resolution velocity field is in agreement with our Hα velocity field. Their lower resolution maps show a much larger H I disc but no greater velocity amplitude, suggesting that our Hα rotation curve reaches the maximum velocity in the outer parts of the optical disc (also, the WHISP position–velocity diagram is in agreement with our Hα position–velocity diagram and rotation curve). This is confirmed by the width of the H I profile at 20 per cent measured by different authors (247 km s^{-1} from Springob et al. 2005, 239 km s^{-1} from Theureau et al. 1998, 251 km s^{-1} from Kamphuis, Sijbring & van Albada 1996) which is in perfect agreement with our Hα velocity field amplitude.

(c) *UGC 11470 (NGC 6824).* The Hα emission is rather faint, and hardly detected on the eastern side of the galaxy because of the interference filter transmission mismatching the systemic velocity. As a result, the rotation curve could be drawn almost only from the approaching side. No H I velocity map is available in the literature. The width of the H I profile at 20 per cent (574 km s^{-1} from Springob et al. 2005) is in agreement with the Hα velocity amplitude showing that the maximum velocity is reached at a small radius (~3 kpc) compared to the optical radius (~18 kpc), in agreement with what is expected for such a bright early-type galaxy ($M_B = -21.3$; Sab). There has been no detection of CO in that galaxy by Elfhag et al. (1996).

(ci) *UGC 11496.* The Hα emission is very faint in that galaxy, sufficient, however, for drawing a velocity field and deriving an acceptable rotation curve. The H I velocity field (WHISP website) is in agreement with our Hα velocity field but much more extended. The width of the H I profile at 20 per cent (121 km s^{-1} from Bottinelli et al. 1990) is in agreement with our Hα velocity field amplitude and confirms that we reach the maximum rotation velocity as already suggested by the shape of our Hα rotation curve, showing a trend to reach a plateau in the outer parts.

(cii) *UGC 11498.* The Hα emission is faint and asymmetric in this early-type galaxy (SBb). However, although there is only a few Hα emission on the receding side, the shape of our rotation curve suggests that a plateau is reached on both sides. No H I velocity map is available in the literature. The width of the H I profile at 20 per cent (509 km s^{-1} from Springob et al. 2005, 500 km s^{-1} from Bottinelli et al. 1990) perfectly matches our Hα velocity field amplitude. We find a maximum rotation velocity of 274 km s^{-1} which seems a bit high when taking into account its luminosity.

(ciii) *UGC 11597 (NGC 6946).* NGC 6946 is a very well studied nearby spiral galaxy. Our Hα Fabry–Perot observations are in perfect agreement with the Hα Fabry–Perot data recently published by Daigle et al. (2006a) who had a larger field-of-view (we miss the outer parts of the optical disc). We find a kinematical inclination of $40° \pm 10°$ close to their value ($8°.4 \pm 3°$) and compatible with the photometric value ($17° \pm 19°$) within the error bars.

(civ) *UGC 11670 (NGC 7013).* The Hα emission is mainly concentrated in the central part of the disc (with two bright blobs, on each side of the central bulge, along the major-axis) and some emission can be seen on the north-western edge of the optical disc. Our Hα rotation curve rapidly reaches a maximum, at about 20 arcsec from the centre (~1 kpc), followed by a slight decrease and a plateau. The velocity gradient observed in the inner 20 arcsec of our position–velocity diagram is consistent with that observed in the H I position–velocity diagram from WHISP (Noordermeer et al. 2005) and their velocity field is in agreement with our Hα velocity field but much more extended. The width of the H I profile at 20 per cent (342 km s^{-1} from Noordermeer et al. 2005, 363 km s^{-1} from Springob et al. 2005, 355 km s^{-1} from Bottinelli et al. 1990) is in good agreement with our Hα velocity field amplitude. The

morphological inclination of 90° found in HyperLeda assumes a thick disc. However, assuming a thin disc, the inclination is found to be 68° with a tilted ring fitted to the H I velocity field (Noordermeer et al. 2005) in agreement with the value deduced from our Hα velocity field (65° ± 2°) as well as with the inclination deduced from the axial ratio (69°) or other morphological determinations (Vorontsov-Velyaminov & Krasnogorskaya 1994).

(cv) *UGC 11872 (NGC 7177)*. Our Hα map has a mottled appearance, in agreement with that of James et al. (2004); however, our observations suffer from bad seeing conditions. Our Hα rotation curve rapidly reaches a well-defined and symmetric plateau, extending up to the optical radius. The rotation curve obtained by Márquez et al. (2002) reaches the plateau more rapidly (10 arcsec instead of 20 arcsec) but they find it at a lower value since they assume a surprisingly high inclination (79°, while we find 47° from our Hα velocity field, which is closer to the morphological value of 54°). Furthermore, slit spectroscopy of the inner part of the galaxy by Héraudeau et al. (1999) confirms that the maximum velocity is not reached before 20 arcsec. No H I velocity map is available in the literature; however, H I linewidths have been measured (314 km s^{-1} from Springob et al. 2005, 317 km s^{-1} from Bottinelli et al. 1990) and are in agreement with our Hα velocity field amplitude. Moreover, a radio synthesis observation has been done (Rhee & van Albada 1996) to derive a position–velocity diagram. It shows a solid body rotation as far out as 1 arcmin which is likely to be explained by beam smearing effects.

(cvi) *UGC 12082*. The Hα emission in this low-luminosity nearby galaxy is rather patchy. Our Hα map is in agreement with that of James et al. (2004). The H I velocity field (WHISP website) confirms our PA determination for the major-axis in the central part. It is, however, much more extended than the Hα one and shows a

strong warp of the H I disc. The WHISP position–velocity diagram suggests that we do not reach the maximum velocity within the optical radius although the shape of our Hα rotation curve shows a trend to reach a plateau in the outer parts. The H I linewidth at 20 per cent confirms that point, since all the values found in the literature (95 km s^{-1} from Braun, Thilker & Walterbos 2003, 103 km s^{-1} from Springob et al. 2005, 79 km s^{-1} from Bottinelli et al. 1990) are markedly larger than the amplitude of our Hα velocity field.

NB. The following targets, already published in the previous GHASP papers, have been observed again in different conditions (filters, seeing, transparency, exposure time, etc.) in order to check if the quality of the data may be improved: UGC 2023, UGC 2034, UGC 3734, UGC 11300 and UGC 12060. The results are fully consistent with the previous set of observations without any significant improvement so that we do not present the new data in this paper, except for UGC 11300.

We present the new observation for UGC 11300 mainly to compare the new method of reduction presented in this paper with the previous GHASP papers. We observe a general good agreement in velocities as well as in radial extension. The adaptive spatial binning enables us now: (1) to plot velocity measurement in the outskirts of the approaching side; (2) to increase the spatial resolution within the inner 30 arcsec (∼1 kpc); and (3) to underline that the error bars are correlated with the spatial resolution and the quality of the data (the error bars are generally smaller and a wide range of amplitudes are observed).

APPENDIX C: TABLES

Table C1. Log of the observations.

$N°$ UGC (1)	$N°$ NGC (2)	α (2000) (3)	δ (2000) (4)	λ_c (Å) (5)	FWHM (Å) (6)	Date (7)	Exposure time (s) (8)	Seeing (arcsec) (9)
12893		00^{h}00^{m}28^{s}0	17°13′ 09″	6582.8	10.6	2003 October 25	8640	2.6
89	23	00^{h}09^{m}53^{s}4	25°55′ 24″	6660.3	20.0	2002 September 5	720	2.6
				6660.3	20.0	2002 September 6	1920	4.3
				6660.2	20.0	2002 September 7	6000	2.6
94	26	00^{h}10^{m}25^{s}9	25°49′ 54″	6660.3	20.0	2002 September 3	6240	2.9
1013	536	01^{h}26^{m}21.8^s	34°42′ 11″	6675.0	20.0	2002 September 10	1920	4.8
				6675.2	20.0	2002 September 8	1920	2.4
NGC 542	542	01^{h}26^{m}21.8^s	34°42′ 11″	6675.0	20.0	2002 September 10	1920	4.8
				6675.2	20.0	2002 September 8	1920	2.4
1317	697	01^{h}51^{m}17^{s}6	22°21′ 28″	6628.4	20.0	2002 September 10	4800	3.4
1437	753	01^{h}57^{m}42^{s}2	35°54′ 58″	6660.2	20.0	2002 September 3	6720	3.8
1655	828	02^{h}10^{m}09^{s}7	39°11′ 25″	6693.1	22.6	2000 October 24	12 720	3.9
1810		02^{h}21^{m}28.7^s	39°22′32″	6735.0	20.0	2002 September 7	7200	3.6
3056	1569	04^{h}30^{m}49.2^s	64°50′53″	6560.3	12.0	2001 November 21	6000	2.7
3334	1961	05^{h}42^{m}04^{s}6	69°22′ 43″	6654.9	20.6	2001 November 20	5040	3.1
3382		05^{h}59^{m}47^{s}7	62°09′ 28″	6658.0	20.0	2003 October 25	4080	3.6
				6658.0	20.0	2003 October 30	7920	4.6
3463		06^{h}26^{m}55^{s}8	59°04′ 47″	6627.6	20.0	2003 March 6	6960	7.2
3521		06^{h}55^{m}00^{s}1	84°02′ 30″	6659.3	20.0	2003 March 8	8400	3.4
3528		06^{h}56^{m}10^{s}6	84°04′ 44″	6659.3	20.0	2003 March 8	8400	3.4
3618	2308	06^{h}58^{m}37.6^s	45°12′38″	6689.5	20.0	2003 March 4	6000	2.4
3685		07^{h}09^{m}05^{s}9	61°35′ 44″	6603.2	12.0	2002 March 17	5520	3.0
3708	2341	07^{h}09^{m}12^{s}0	20°36′ 11″	6674.2	20.0	2003 March 2	6480	3.3
3709	2342	07^{h}09^{m}18^{s}1	20°38′ 10″	6674.2	20.0	2003 March 2	6480	3.3
3826		07^{h}24^{m}28^{s}0	61°41′ 38″	6601.6	12.0	2002 March 20	4560	3.2
3740	2276	07^{h}27^{m}13^{s}1	85°45′ 16″	6613.7	11.1	2002 March 15	4800	3.4

Table C1 – *continued*

N° UGC (1)	N° NGC (2)	α (2000) (3)	δ (2000) (4)	λ$_c$ (Å) (5)	FWHM (Å) (6)	Date (7)	Exposure time (s) (8)	Seeing (arcsec) (9)
3876		07^{h}29^{m}17^{s}5	27°54′00″	6581.7	10.6	2004 March 18	6000	3.4
				6581.7	10.6	2004 March 19	9600	3.4
3915		07^{h}34^{m}55^{s}8	31°16′34″	6659.2	20.0	2003 March 3	6000	3.4
IC 476		07^{h}47^{m}16^{s}5	26°57′03″	6659.2	20.0	2003 March 7	6240	3.0
4026	2449	07^{h}47^{m}20^{s}4	26°55′48″	6659.2	20.0	2003 March 7	6240	3.0
4165	2500	08^{h}01^{m}53^{s}2	50°44′15″	6573.7	11.4	2002 March 16	4800	3.0
				6573.6	11.4	2002 March 17	4800	2.5
4256	2532	08^{h}10^{m}15^{s}2	33°57′24″	6674.3	20.0	2004 March 17	6960	2.4
4393		08^{h}26^{m}04^{s}4	45°58′02″	6611.1	11.1	2004 March 20	6960	3.5
4422	2595	08^{h}27^{m}42^{s}0	21°28′45″	6658.4	20.0	2003 March 9	7200	2.7
4456		08^{h}32^{m}03^{s}5	24°00′39″	6688.7	20.0	2004 March 22	6720	4.8
4555	2649	08^{h}44^{m}08^{s}4	34°43′02″	6658.7	20.0	2004 March 23	6960	5.9
4770	2746	09^{h}05^{m}59^{s}4	35°22′38″	6718.7	20.0	2004 March 24	7920	4.3
4820	2775	09^{h}10^{m}20^{s}1	07°02′17″	6593.0	10.1	2003 March 6	8400	6.3
5045		09^{h}28^{m}10^{s}2	44°39′52″	6734.3	20.0	2003 March 9	6960	2.5
5175	2977	09^{h}43^{m}46^{s}8	74°51′35″	6628.5	20.0	2004 March 23	5520	6.9
5228		09^{h}46^{m}03^{s}8	01°40′06″	6602.9	12.0	2003 March 4	9120	2.8
5251	3003	09^{h}48^{m}36^{s}4	33°25′17″	6593.9	10.1	2002 March 15	1680	3.1
5279	3026	09^{h}50^{m}55.1^s	28°33′05″	6594.2	10.1	2004 March 16	6000	2.7
5319	3061	09^{h}56^{m}12^{s}0	75°51′59″	6613.9	11.1	2004 March 17	7200	2.4
5351	3067	09^{h}58^{m}21.3^s	32°22′12″	6593.7	10.1	2003 March 7	7200	4.1
5373		10^{h}00^{m}00^{s}5	05°19′58″	6571.0	11.4	2004 March 22	7680	4.6
5398	3077	10^{h}03^{m}20.0^s	68°44′01″	6563.7	12.0	2003 March 8	7920	3.2
IC 2542		10^{h}07^{m}50^{s}5	34°18′55″	6689.7	20.0	2004 March 21	7440	4.1
5510	3162	10^{h}13^{m}31^{s}7	22°44′14″	6592.3	10.1	2003 March 2	6240	3.5
5532	3147	10^{h}16^{m}53^{s}5	73°24′03″	6630.3	9.6	2002 March 19	4560	3.3
				6623.1	8.6	2002 March 20	1920	3.3
5556	3187	10^{h}17^{m}47.9^s	21°52′24″	6593.9	10.1	2002 March 17	5760	3.1
5786	3310	10^{h}38^{m}45^{s}9	53°30′12″	6584.2	10.6	2002 March 20	4080	4.1
5840	3344	10^{h}43^{m}31^{s}1	24°55′21″	6573.7	11.4	2002 March 20	5760	3.3
5842	3346	10^{h}43^{m}39^{s}0	14°52′18″	6584.2	10.6	2004 March 20	6000	3.5
6118	3504	11^{h}03^{m}11^{s}3	27°58′20″	6593.9	10.1	2002 March 18	5760	2.4
6277	3596	11^{h}15^{m}06^{s}2	14°47′12″	6580.8	10.6	2004 March 19	10 320	2.9
6419	3664	11^{h}24^{m}24^{s}6	03°19′36″	6593.9	10.1	2003 April 27	6960	3.5
6521	3719	11^{h}32^{m}13^{s}4	00°49′09″	6689.2	20.0	2003 March 5	6960	3.7
6523	3720	11^{h}32^{m}21^{s}6	00°48′14″	6689.2	20.0	2003 March 5	6960	3.7
6787	3898	11^{h}49^{m}15^{s}6	56°05′04″	6584.3	10.6	2002 March 19	3600	2.9
				6584.2	10.6	2002 March 20	5760	3.3
7021	4045	12^{h}02^{m}42^{s}3	01°58′36″	6602.6	12.0	2003 March 4	7200	4.3
7045	4062	12^{h}04^{m}03^{s}8	31°53′42″	6581.1	10.6	2004 March 18	6000	2.1
7154	4145	12^{h}10^{m}01^{s}4	39°53′02″	6584.2	10.6	2002 March 21	5520	4.2
7429	4319	12^{h}21^{m}43.1^s	75°19′22″	6592.1	10.1	2003 March 3	6960	4.3
7699		12^{h}32^{m}48.0^s	37°37′18″	6573.9	14.0	2004 March 22	6720	4.6
7766	4559	12^{h}35^{m}57^{s}3	27°57′38″	6583.3	10.6	2002 June 17	2400	1.9
7831	4605	12^{h}39^{m}59^{s}7	61°36′29″	6565.7	12.0	2002 June 15	3840	2.2
7853	4618	12^{h}41^{m}33^{s}1	41°09′05″	6573.6	11.4	2002 March 18	5040	2.6
7861	4625	12^{h}41^{m}52^{s}9	41°16′25″	6575.7	11.4	2002 June 16	3840	3.3
7876	4635	12^{h}42^{m}39^{s}3	19°56′44″	6584.3	10.6	2004 March 17	6720	3.0
7901	4651	12^{h}43^{m}42^{s}7	16°23′35″	6581.7	10.6	2004 March 19	8160	3.8
7985	4713	12^{h}49^{m}57^{s}9	05°18′42″	6574.1	11.4	2003 April 26	6240	5.4
8334	5055	13^{h}15^{m}49^{s}4	42°01′46″	6572.9	13.7	2002 June 14	4320	2.3
8403	5112	13^{h}21^{m}56^{s}6	38°44′05″	6584.2	10.6	2002 March 21	4080	4.4
NGC 5296	5296	13^{h}46^{m}18^{s}7	43°51′04″	6615.4	11.1	2002 June 13	6000	3.2
8709	5297	13^{h}46^{m}23^{s}7	43°52′20″	6615.4	11.1	2002 June 13	6000	3.2
8852	5376	13^{h}55^{m}16^{s}1	59°30′25″	6610.2	11.1	2003 March 5	2880	2.8
				6609.9	11.1	2003 March 7	4800	3.7
8863	5377	13^{h}56^{m}16^{s}7	47°14′08″	6601.1	12.0	2004 March 26	5040	3.3
8898	5394	13^{h}58^{m}33^{s}7	37°27′12″	6651.1	20.6	2002 March 18	4320	2.7
8900	5395	13^{h}58^{m}38^{s}0	37°25′28″	6651.1	20.6	2002 March 18	4320	2.7
8937	5430	14^{h}00^{m}45^{s}8	59°19′43″	6628.2	20.0	2003 March 3	8880	4.4
9013	5474	14^{h}05^{m}02^{s}0	53°39′08″	6565.2	12.0	2002 June 14	5040	2.3

Table C1 – *continued*

N° UGC (1)	N° NGC (2)	α (2000) (3)	δ (2000) (4)	λ_c (Å) (5)	FWHM (Å) (6)	Date (7)	Exposure time (s) (8)	Seeing (arcsec) (9)
9179	5585	$14^h19^m48^s.1$	56°43′45″	6570.7	11.4	2004 March 20	8160	3.1
9219	5608	*$14^h23^m17.5^s$*	*41°46′34″*	6573.7	11.4	2004 March 22	6480	4.7
9248	5622	$14^h26^m12^s.2$	48°33′51″	6655.2	20.6	2004 March 21	10 800	4.8
9358	5678	$14^h32^m05^s.6$	57°55′16″	6603.0	12.0	2004 March 19	7680	4.3
9363	5668	$14^h33^m24^s.4$	04°27′02″	6594.1	10.1	2003 April 26	8160	2.8
9406	5693	$14^h36^m11^s.1$	48°35′06″	6612.6	11.1	2003 April 28	6000	3.3
9465	5727	$14^h40^m26^s.1$	33°59′23″	6594.1	10.1	2004 March 17	6480	3.4
9576	5774	$14^h53^m42^s.5$	03°34′57″	6594.2	10.1	2003 April 27	6840	4.1
9736	5874	$15^h07^m51^s.9$	54°45′08″	6629.1	20.0	2003 March 2	3840	4.8
9866	5949	$15^h28^m00^s.6$	64°45′46″	6572.2	11.4	2004 March 24	5280	6.9
9943	5970	$15^h38^m30^s.0$	12°11′11″	6602.5	12.0	2003 March 4	8400	4.3
10075	6015	$15^h51^m25^s.3$	62°18′36″	6580.9	10.6	2004 March 18	5760	3.2
10521	6207	$16^h43^m03^s.7$	36°49′55″	6582.1	10.6	2003 April 28	2400	3.0
				6582.1	10.6	2003 April 29	5280	3.9
10652	6283	$16^h59^m26^s.5$	49°55′20″	6584.2	10.6	2003 April 26	2880	3.2
				6584.2	10.6	2003 April 27	3120	4.1
10713		*$17^h04^m33.7^s$*	*72°26′45″*	6585.5	10.6	2002 September 4	5040	2.4
10757		$17^h10^m13^s.4$	72°24′38″	6586.0	10.6	2002 June 17	5280	2.4
10769		*$17^h11^m33.5^s$*	*72°24′07″*	6592.9	10.1	2002 June 17	5280	2.1
10791		$17^h14^m38^s.5$	72°23′56″	6593.1	10.1	2002 June 15	6000	2.6
11012	6503	$17^h49^m26^s.3$	70°08′40″	6562.2	8.8	2002 September 6	5040	2.6
11269	6667	$18^h30^m39^s.7$	67°59′14″	6615.5	11.1	2002 June 17	3840	2.3
11300	6689	$18^h34^m49^s.9$	70°31′28″	6584.4	10.6	2002 September 5	5040	3.7
11332	6654A	*$18^h39^m25.2^s$*	*73°34′48″*	6594.7	10.1	2002 September 10	7200	5.5
11407	6764	$19^h08^m16^s.4$	50°55′59″	6615.0	11.1	2002 September 11	6480	2.6
11466		$19^h42^m59^s.1$	45°17′58″	6583.0	10.6	2002 June 16	5040	2.3
11470	6824	$19^h43^m40^s.8$	56°06′34″	6628.6	20.0	2002 September 6	3600	2.2
11496		$19^h53^m01^s.8$	67°39′54″	6611.3	11.1	2002 June 18	5520	1.9
11498		$19^h57^m15^s.1$	05°53′24″	6628.0	20.0	2003 October 25	8400	4.3
11597	6946	$20^h34^m52^s.5$	60°09′12″	6562.3	8.8	2002 June 14	5280	2.4
11670	7013	$21^h03^m33^s.7$	29°53′50″	6581.9	10.6	2002 September 11	7440	2.7
11872	7177	$22^h00^m41^s.2$	17°44′18″	6584.8	10.6	2002 September 10	7200	4.7
12082		$22^h34^m11^s.3$	32°51′42″	6582.1	10.6	2002 September 2	7440	2.8

Column (1): name of the galaxy in the UGC catalogue except for NGC 542, IC 476, IC 2542 and NGC 5296 that do not have UGC name. Column (2): name in the NGC catalogue when available. Columns (3) and (4): coordinates (in J2000) of the centre of the galaxy used for the kinematic study except for those in italic (taken from HyperLeda). Column (5): central wavelength of the interference filter used. Column (6): FWHM of the interference filter. Column (7): date of the observations. Column (8): total exposure time in second. Column (9): seeing in arcsec.

Table C2. Model parameters.

N° UGC (1)	V_{sys_Leda} (km s^{-1}) (2)	V_{sys_FP} (km s^{-1}) (3)	i_{Morph} (°) (4)	i_{Kin} (°) (5)	PA_{Morph} (°) (6)	PA_{Kin} (°) (7)	$\overline{Res}$ (10^{-3} km s^{-1}) (8)	σ_{res} (km s^{-1}) (9)	χ^2_{red} (10)
12893	1102 ± 7	1097 ± 2	30 ± 8	19 ± 19	95 ± 51	77# ± 5	−28.1	8	1.2
89	4564 ± 3	4510 ± 5	40 ± 4	33 ± 13	174 ± 24	177 ± 4	42.5	23	8.6
94	4592 ± 4	4548 ± 2	50 ± 4	42 ± 5	102 ± 15	94 ± 2	−3.9	13	2.7
1013	5190 ± 4		80 ± 3		68 ± 5				
NGC 542	4660 ± 8		90		143 ± 6				
1317	3111 ± 5	3090 ± 2	75 ± 4	73 ± 1	105 ± 5	106 ± 1	−1.3	15	3.3
1437	4893 ± 4	4858 ± 2	52 ± 3	47 ± 4	134 ± 17	127# ± 2	−0.8	18	5.2
1655	5340 ± 16	5427 ± 7	45 ± 9	45 ± 18*		138# ± 6	−2744.9	30	15.4
1810	7556 ± 21		75 ± 3		42 ± 6				
3056	−100 ± 7		65 ± 7		120 ± 12				
3334	3934 ± 4	3952 ± 13	47 ± 7	47 ± 14*	85 ± 15	97# ± 6	9.9	54	46.0
3382	4497 ± 6	4489 ± 2	21 ± 10	21 ± 14	30^{2M}/168^{Pa} ± 61	6# ± 2	−11.5	16	4.1
3463	2692 ± 4	2679 ± 3	63 ± 3	63 ± 3	117 ± 8	110 ± 2	−0.1	15	3.6
3521	4426 ± 7	4415 ± 2	61 ± 3	58 ± 5	76 ± 12	78# ± 3	3.2	16	4.1
3528	4421 ± 18	4340 ± 5	59 ± 5	42 ± 12	38 ± 16	43# ± 4	−17.8	32	17.6
3618	5851 ± 6		49 ± 5		171 ± 16				
3685	1796 ± 4	1795 ± 1	55 ± 4	12 ± 17	133 ± 12	118# ± 4	−1.3	9	1.4
3708	5201 ± 26	5161 ± 4	16 ± 24	44 ± 16	136^{Ni} ± 90	50# ± 4	−11.6	18	5.4

Table C2 – *continued*

$N°$ UGC (1)	$V_{\mathrm{sys\_Leda}}$ (km s^{-1}) (2)	$V_{\mathrm{sys\_FP}}$ (km s^{-1}) (3)	i_{Morph} (°) (4)	i_{Kin} (°) (5)	PA$_{\mathrm{Morph}}$ (°) (6)	PA$_{\mathrm{Kin}}$ (°) (7)	$\overline{Res}$ (10^{-3} km s^{-1}) (8)	σ_{res} (km s^{-1}) (9)	χ^2_{red} (10)
3709	5223 ± 50	5292 ± 4	46 ± 4	55 ± 4	66 ± 18	$52^{\#} \pm 2$	-4.7	18	5.3
3826	1733 ± 3	1724 ± 2	30 ± 9	20 ± 19	$160^{2M}/85^{Ni} \pm 34$	$74^{\#} \pm 5$	135.4	9	1.2
3740	2417 ± 6	2416 ± 2	40 ± 6	48 ± 14	19 ± 20	$67^{\#} \pm 4$	<0.1	11	1.7
3876	860 ± 7	854 ± 2	61 ± 3	59 ± 5	178 ± 9	$178^{\#} \pm 3$	-0.2	10	1.6
3915	4679 ± 7	4659 ± 3	59 ± 5	47 ± 4	25 ± 17	30 ± 2	6.8	13	2.7
IC 476	4734 ± 32	4767 ± 3	40 ± 5	55 ± 24	102 ± 30	68 ± 6	-5.9	18	5.5
4026	4782 ± 11	4892 ± 3	73 ± 4	56 ± 4	136 ± 8	139 ± 2	4.0	19	5.7
4165	515 ± 4	504 ± 1	21 ± 9	41 ± 10	$74^{Pa} \pm 43$	$85^{\#} \pm 2$	-0.4	10	1.6
4256	5252 ± 5	5252 ± 3	36 ± 4	38 ± 21	26 ± 23	$111^{\#} \pm 6$	15.9	26	11.1
4393	2126 ± 5	2119 ± 4	50 ± 5	$50 \pm 9^{*}$	50 ± 22	$70^{\#} \pm 7$	0.6	11	1.7
4422	4333 ± 4	4321 ± 2	49 ± 4	25 ± 8	12 ± 17	36 ± 2	-18.3	20	6.2
4456	5497 ± 23	5470 ± 1	28 ± 6	9 ± 14	42 ± 41	124 ± 3	7.3	14	3.1
4555	4235 ± 6	4235 ± 2	21 ± 12	38 ± 7	$140^{2M}/78^{SDSS} \pm 72$	90 ± 2	0.5	15	3.5
4770	7063 ± 9	7026 ± 3	36 ± 9	20 ± 13	54 ± 30	$98^{\#} \pm 3$	-36.8	14	3.0
4820	1355 ± 4	1350 ± 2	41 ± 4	38 ± 3	160 ± 16	157 ± 2	<0.1	13	2.7
5045	7716 ± 23	7667 ± 2	41 ± 4	16 ± 9	136 ± 21	148 ± 2	-2.8	13	2.7
5175	3052 ± 11	3049 ± 2	65 ± 4	56 ± 3	145 ± 9	143 ± 2	-2.3	13	2.9
5228	1873 ± 7	1869 ± 2	82 ± 2	72 ± 2	122 ± 4	120 ± 2	-0.7	9	1.3
5251	1481 ± 3	1465 ± 3	88 ± 9	73 ± 6	78 ± 3	$80^{\#} \pm 3$	<0.1	15	3.5
5279	1488 ± 4		90		83 ± 4				
5319	2448 ± 9	2439 ± 1	40 ± 5	30 ± 9	$125^{2M}/7^{Pa} \pm 19$	$165^{\#} \pm 2$	-21.0	9	1.3
5351	1473 ± 4		82 ± 6		105 ± 4				
5373	302 ± 3	291 ± 2	60 ± 6	10 ± 18	110 ± 12	51 ± 8	-0.5	8	0.9
5398	14 ± 5		40 ± 10		45 ± 23				
IC 2542	6113 ± 20	6111 ± 2	43 ± 4	20 ± 15	173 ± 21	174 ± 3	-0.9	20	6.3
5510	1301 ± 3	1298 ± 2	38 ± 5	31 ± 10	26 ± 24	$20^{\#} \pm 3$	-0.3	10	1.4
5532	2812 ± 8	2802 ± 1	33 ± 9	32 ± 3	150 ± 27	147 ± 1	<0.1	14	2.9
5556	1581 ± 3		75 ± 2		105 ± 5				
5786	990 ± 3	992 ± 4	16 ± 25	53 ± 11	$18^{SDSS} \pm 90$	153 ± 5	-574.4	18	4.9
5840	582 ± 4	580 ± 1	18 ± 14	18 ± 11		$153^{\#} \pm 3$	<0.1	12	2.1
5842	1261 ± 10	1245 ± 1	34 ± 6	47 ± 9	104 ± 24	$112^{\#} \pm 2$	-1.5	10	1.7
6118	1539 ± 5	1525 ± 2	27 ± 7	$39 \pm 8^{*}$	$150^{2M}/57^{Pa} \pm 32$	$163^{\#} \pm 3$	16.3	11	1.9
6277	1192 ± 3	1191 ± 3	17 ± 16	$17 \pm 17^{*}$	$0^{2M} \pm 86$	76 ± 3	-5.1	19	5.7
6419	1365 ± 24	1381 ± 2	57 ± 5	66 ± 19	27 ± 15	34 ± 7	-1.8	8	0.9
6521	5879 ± 5	5842 ± 2	50 ± 3	46 ± 4	21 ± 13	20 ± 2	-0.9	17	4.5
6523	5913 ± 13	5947 ± 2	24 ± 7	$24 \pm 14^{*}$	$36^{Va}/12^{Pa}/1^{Pa} \pm 52$	$173^{\#} \pm 3$	-6.4	13	2.8
6787	1173 ± 3	1157 ± 1	57 ± 3	70 ± 2	108 ± 10	112 ± 2	-0.7	17	4.4
7021	1979 ± 8	1976 ± 3	56 ± 4	$56 \pm 7^{*}$	89 ± 11	$86^{\#} \pm 2$	-0.6	14	3.1
7045	770 ± 6	758 ± 1	70 ± 2	68 ± 2	101 ± 5	99 ± 2	0.2	10	1.5
7154	1011 ± 28	1009 ± 1	64 ± 3	65 ± 3	100 ± 8	$95^{\#} \pm 2$	<0.1	12	2.3
7429	1476 ± 24		73 ± 3		162 ± 7				
7699	496 ± 1		78 ± 2		32 ± 4				
7766	814 ± 3	807 ± 1	65 ± 4	69 ± 3	150 ± 7	$143^{\#} \pm 2$	<0.1	12	2.4
7831	147 ± 4	136 ± 3	70 ± 3	56 ± 12	125 ± 5	$110^{\#} \pm 5$	<0.1	9	1.2
7853	537 ± 4	530 ± 2	58 ± 5	$58 \pm 28^{*}$	40 ± 12	$37^{\#} \pm 4$	12.8	8	1.1
7861	611 ± 4	598 ± 1	47 ± 6	$47 \pm 24^{*}$	$116^{Pa}/30^{SDSS} \pm 20$	$117^{\#} \pm 4$	<0.1	11	1.9
7876	955 ± 8	944 ± 1	44 ± 5	53 ± 9	3 ± 22	$164^{\#} \pm 3$	0.3	8	1.1
7901	799 ± 2	788 ± 2	50 ± 3	53 ± 2	77 ± 11	$74^{\#} \pm 2$	<0.1	12	2.2
7985	653 ± 3	642 ± 2	24 ± 12	49 ± 6	$110^{2M}/87^{Ha}/153^{Pa}/100^{Ni}/88^{SDSS} \pm 48$	$96^{\#} \pm 3$	-0.1	8	1.0
8334	508 ± 3	484 ± 1	55 ± 5	66 ± 1	102 ± 11	100 ± 1	-0.1	11	1.7
8403	969 ± 4	975 ± 2	54 ± 3	57 ± 4	129 ± 12	121 ± 2	-0.1	9	1.3
NGC 5296	2243 ± 3	2254 ± 2	65 ± 6	65 ± 4	12 ± 15	2 ± 3	-6.2	4	0.3
8709	2407 ± 13	2405 ± 3	82 ± 3	76 ± 1	147 ± 4	$150^{\#} \pm 2$	0.1	15	3.3
8852	2023 ± 17	2075 ± 1	55 ± 7	52 ± 3	65 ± 16	63 ± 2	0.9	10	1.5
8863	1796 ± 7	1789 ± 4	77 ± 4	$77 \pm 13^{*}$	38 ± 5	$38^{\#} \pm 7^{*}$	-41.4	14	3.3
8898	3464 ± 10	3448 ± 2	71 ± 3	27 ± 20	$30^{2M}/140^{Pa}/117^{SDSS} \pm 7$	31 ± 6	41.5	7	0.7
8900	3466 ± 11	3511 ± 3	66 ± 5	57 ± 10	172 ± 10	161 ± 2	5.8	20	6.6
8937	2968 ± 9	2961 ± 5	50 ± 5	32 ± 12	177 ± 16	$5^{\#} \pm 3$	2361.4	19	5.7
9013	255 ± 23	262 ± 1	50 ± 4	$21 \pm 16^{*}$	85 ± 14	164 ± 4	1.8	7	0.8
9179	302 ± 2	293 ± 2	53 ± 3	36 ± 14	33 ± 11	49 ± 4	<0.1	9	1.4
9219	666 ± 11		81 ± 6		99 ± 9				
9248	3867 ± 6	3865 ± 2	58 ± 3	58 ± 4	86 ± 12	$81^{\#} \pm 2$	3.5	15	3.6

Table C2 – *continued*

N° UGC (1)	$V_{\text{sys\_Leda}}$ (km s^{-1}) (2)	$V_{\text{sys\_FP}}$ (km s^{-1}) (3)	i_{Morph} (°) (4)	i_{Kin} (°) (5)	PA$_{\text{Morph}}$ (°) (6)	PA$_{\text{Kin}}$ (°) (7)	$\overline{Res}$ (10^{-3} km s^{-1}) (8)	σ_{res} (km s^{-1}) (9)	χ^2_{red} (10)
9358	1907 ± 4	1912 ± 3	62 ± 3	54 ± 4	2 ± 9	2$^{\#}$ ± 2	2.3	15	3.5
9363	1584 ± 3	1577 ± 1	33 ± 6	18 ± 14*	107 ± 27	147 ± 3	3.2	8	1.1
9406	2279 ± 2	2281 ± 2	51 ± 7	59 ± 25	60^{2M}/150^{SDSS} ± 22	132 ± 12	78.0	11	2.0
9465	1495 ± 3	1485 ± 2	90	65 ± 4	143 ± 9	127 ± 3	0.3	8	1.1
9576	1565 ± 5	1555 ± 2	52 ± 4	41 ± 11	125 ± 14	122 ± 3	−0.4	10	1.6
9736	3128 ± 4	3135 ± 2	51 ± 3	51 ± 5	57 ± 13	39$^{\#}$ ± 2	2.9	14	3.2
9866	427 ± 4	430 ± 1	69 ± 3	56 ± 6	150 ± 7	148 ± 2	−5.1	7	0.8
9943	1958 ± 4	1946 ± 1	48 ± 5	54 ± 2	87 ± 14	86$^{\#}$ ± 2	−0.1	9	1.4
10075	831 ± 3	827 ± 1	66 ± 3	62 ± 2	28 ± 7	30$^{\#}$ ± 1	<0.1	9	1.4
10521	852 ± 2	832 ± 2	71 ± 3	59 ± 3	17 ± 7	20 ± 2	0.7	9	1.2
10652	1092 ± 26	1089 ± 1	30 ± 7	21 ± 13	56 ± 33	45$^{\#}$ ± 3	0.6	8	1.0
10713	1073 ± 4		90		8 ± 4				
10757	1168 ± 8	1210 ± 2	59 ± 3	44 ± 22	66 ± 12	56 ± 6	0.7	11	1.8
10769	1230 ± 13		57 ± 4		41 ± 16				
10791	1328 ± 6	1318 ± 3	0	34 ± 20*		92 ± 4	726.5	10	1.7
11012	36 ± 12	25 ± 1	74 ± 2	72 ± 2	123 ± 5	119$^{\#}$ ± 2	0.4	8	1.0
11269	2590 ± 6	2563 ± 6	60 ± 8	69 ± 4	97 ± 12	92$^{\#}$ ± 3	3.8	30	14.4
11300	488 ± 3	480 ± 2	77 ± 2	76 ± 4	171 ± 4	167 ± 3	<0.1	10	1.6
11332	1569 ± 25		82 ± 2		65 ± 3				
11407	2412 ± 4	2402 ± 8	64 ± 3	64 ± 22*	65 ± 9	65 ± 10*	1.0	20	6.6
11466	820 ± 9	826 ± 3	55 ± 3	66 ± 5	35 ± 13	46$^{\#}$ ± 3	−0.3	13	2.6
11470	3530 ± 40	3546 ± 5	47 ± 6	47 ± 7	50 ± 22	47 ± 3	258.0	25	10.7
11496	2105 ± 6	2115 ± 2	0	44 ± 16		167 ± 4	135.8	9	1.2
11498	3266 ± 8	3284 ± 4	79 ± 4	71 ± 2	75 ± 7	71$^{\#}$ ± 2	−23.4	22	7.9
11597	46 ± 3	40 ± 2	17 ± 19	40 ± 10		61$^{\#}$ ± 3	0.4	13	2.5
11670	778 ± 3	776 ± 3	90	65 ± 2	159 ± 5	153$^{\#}$ ± 2	0.8	16	3.9
11872	1147 ± 5	1140 ± 1	54 ± 6	47 ± 3	88 ± 13	86 ± 2	−0.1	13	2.7
12082	803 ± 2	792 ± 2	29 ± 11	14 ± 19		143 ± 5	0.6	8	1.1

Column (1): name in the UGC catalogue (see Table C1). Column (2): systemic velocity found in the HyperLeda data base. Column (3): systemic velocity deduced from our velocity field analysis. Column (4): morphological inclination from HyperLeda (Paturel et al. 1997). Column (5): inclination deduced from the analysis of our velocity field; those marked with an asterisk (*) have been fixed equal to morphological value, except for UGC 6118, UGC 9013, UGC 9363 and UGC 10791 for which we used inclinations determined from H I data (see Table C3). Column (6): morphological PA from HyperLeda, except for those marked (*Ha*: Haynes et al. 1999; *Ni*: Nilson 1973; *PA*: Paturel et al. 2000; *SDSS*: 2006 Sloan Digital Sky Survey, DR5; *2M*: Two-Micron All-Sky Survey team 2003, 2MASS extended objects; *Va*: Vauglin et al. 1999). Column (7): PA deduced from our velocity field; those marked with an asterisk (*) have been fixed equal to morphological value. The symbol$^{\#}$ indicates that the PA refers to the approaching side. Column (8): mean residual velocity in the whole velocity field. Column (9): residual velocity dispersion in the whole velocity field. Column (10): reduced χ^2 of the model.

Table C3. Galaxy parameters.

N° UGC (1)	t (2)	Type (3)	D Mpc (4)	M_B (mag) (5)	b/a (6)	$i_{b/a}$ (°) (7)	$D_{25}/2$ (arcsec kpc^{-1}) (8)	V_{max} flag (km s^{-1}) (9)	V_{max} (10)	H I data (11)
12893	8.4 ± 0.8	Sd	12.5^{Ja}	−15.5	0.89 ± 0.06	27 ± 7	34 ± 5/2.1 ± 0.3	72 ± 67	2	
89	1.2 ± 0.6	SBa	64.2^{Mo}	−21.5	0.79 ± 0.04	38 ± 3	46 ± 4/14.5 ± 1.4	343 ± 117	1	W^{N05}
94	2.4 ± 0.6	S(r)ab	64.2^{Mo}	−20.4	0.68 ± 0.04	47 ± 3	34 ± 3/10.5 ± 0.8	209 ± 21	1	W^{N05}
1013	3.1 ± 0.2	SB(r)b pec	70.8	−22.0	0.31 ± 0.03	72 ± 2	88 ± 6/30.1 ± 2.0			W^{Web}
NGC 542	2.8 ± 3.9	Sb pec	63.7	−19.5	0.22 ± 0.03	77 ± 2	34 ± 6/10.4 ± 1.7	125 ± 8^{PV}	2	
1317	4.9 ± 0.7	SAB(r)c	42.2	−21.5	0.33 ± 0.04	71 ± 2	114 ± 7/23.4 ± 1.5	205 ± 9	1	W^{Web}
1437	4.9 ± 1.0	SABc	66.8	−21.8	0.63 ± 0.03	51 ± 2	43 ± 5/13.8 ± 1.7	218 ± 15	1	W^{Web}
1655	1.0 ± 0.5	Sa	73.0	−21.6	0.75 ± 0.09	42 ± 8	86 ± 10/30.3 ± 3.5	205 ± 64	4	
1810	3.1 ± 0.6	Sb pec	102.4	−22.2	0.36 ± 0.02	69 ± 1	52 ± 4/26.0 ± 2.0			W^{Web}
3056	9.6 ± 1.2	IB	2.5^{Oc}	−18.7	0.57 ± 0.06	55 ± 4	119 ± 9/1.4 ± 0.1			
3334	4.2 ± 1.0	SABb	55.6	−22.8	0.70 ± 0.07	45 ± 6	132 ± 8/35.7 ± 2.2	377 ± 85	1	W^{Web}
3382	1.0 ± 0.4	SB(r)a	62.8	−20.4	0.94 ± 0.05	20 ± 9	38 ± 4/11.5 ± 1.1	322 ± 207	2	W^{N05}
3463	4.7 ± 0.9	SABc	38.6	−20.7	0.49 ± 0.03	61 ± 2	66 ± 4/12.4 ± 0.8	168 ± 9	1	
3521	4.8 ± 1.8	Sc	62.6	−19.8	0.52 ± 0.03	59 ± 2	35 ± 4/10.7 ± 1.1	167 ± 12	3	
3528	2.0 ± 0.3	SBab	61.8	−20.1	0.58 ± 0.06	55 ± 4	41 ± 5/12.2 ± 1.6	276 ± 66	2	
3618	2.0 ± 0.3	Sab	80.0	−20.9	0.70 ± 0.05	46 ± 4	44 ± 4/16.9 ± 1.4			
3685	3.0 ± 0.4	SB(r)b	26.3^{Ja}	−19.7	0.61 ± 0.04	52 ± 3	57 ± 4/7.3 ± 0.5	133 ± 177	3	W^{Web}
3708	4.5 ± 1.7	Sbc pec	70.0	−20.7	0.96 ± 0.11	15 ± 23	25 ± 6/8.3 ± 2.0	235 ± 69	1	

Table C3 – *continued*

N° UGC (1)	t (2)	Type (3)	D (Mpc) (4)	M_B (mag) (5)	b/a (6)	$i_{b/a}$ (°) (7)	$D_{25}/2$ (arcsec kpc^{-1}) (8)	V_{max} flag (km s^{-1}) (9)	V_{max} (10)	H I data (11)
3709	5.7 ± 1.6	Sc	70.7	−21.5	0.71 ± 0.05	45 ± 4	35 ± 3/12.1 ± 1.1	241 ± 14	1	
3826	6.5 ± 0.8	SABc	25.7^{Ja}	−17.9	0.87 ± 0.07	29 ± 8	98 ± 9/12.2 ± 1.2	74 ± 66	1	W^{Web}
3740	5.4 ± 0.6	SAB(r)c pec	17.1^{Sh}	−19.8	0.78 ± 0.06	39 ± 5	67 ± 5/5.5 ± 0.4	87 ± 20	2	W^{Web}
3876	6.5 ± 0.8	Scd	14.5^{Ja}	−17.4	0.50 ± 0.03	60 ± 2	57 ± 4/4.0 ± 0.3	112 ± 10	2	
3915	4.6 ± 1.6	SBc	63.6	−21.4	0.55 ± 0.06	57 ± 4	34 ± 6/10.3 ± 1.7	205 ± 16	1	
IC 476	4.2 ± 2.6	SABb	63.9	−19.0	0.78 ± 0.05	39 ± 5	18 ± 3/5.7 ± 0.8	71 ± 22	3	
4026	2.0 ± 0.4	Sab	64.7	−20.8	0.41 ± 0.03	66 ± 2	43 ± 4/13.5 ± 1.2	285 ± 14	2	
4165	6.9 ± 0.4	SBcd	11.0^{Mo}	−18.2	0.94 ± 0.05	20 ± 8	74 ± 5/3.9 ± 0.2	80 ± 18	1	W^{Web}
4256	5.2 ± 0.6	SABc	71.7	−21.6	0.82 ± 0.04	35 ± 4	50 ± 4/17.3 ± 1.3	123 ± 59	1	W^{Web}
4393	4.6 ± 1.3	SBc	31.5^{Ja}	−19.3	0.66 ± 0.05	49 ± 4	44 ± 7/6.7 ± 1.1	47 ± 10	4	
4422	4.9 ± 0.6	SAB(r)c	58.1	−21.1	0.68 ± 0.04	47 ± 3	51 ± 5/14.4 ± 1.4	354 ± 95	1	
4456	5.2 ± 0.6	S(r)c	74.0	−20.8	0.89 ± 0.04	27 ± 5	31 ± 3/11.0 ± 1.1	212 ± 321	1	
4555	4.0 ± 0.6	SABb	58.0	−20.9	0.94 ± 0.07	20 ± 11	45 ± 5/12.7 ± 1.4	185 ± 30	1	
4770	1.1 ± 0.6	SBa	95.9	−21.3	0.83 ± 0.07	34 ± 8	48 ± 5/22.3 ± 2.3	330 ± 195	3	
4820	1.7 ± 0.8	S(r)ab	17.1^{Sh}	−20.3	0.79 ± 0.04	38 ± 4	127 ± 6/10.6 ± 0.5	337 ± 20	1	
5045	5.0 ± 0.5	SAB(r)c	105.1	−21.2	0.76 ± 0.04	40 ± 4	35 ± 3/18.0 ± 1.5	429 ± 228	1	
5175	3.2 ± 0.7	Sb	44.1	−20.6	0.48 ± 0.05	61 ± 3	62 ± 5/13.2 ± 1.1	188 ± 10	1	
5228	4.9 ± 0.5	SBc	24.7	−19.9	0.25 ± 0.02	76 ± 1	68 ± 5/8.2 ± 0.6	125 ± 9	1	
5251	4.3 ± 0.8	SBbc pec	21.5	−20.5	0.22 ± 0.01	77 ± 1	142 ± 7/14.8 ± 0.7	125 ± 9	3	W^{Web}
5279	9.7 ± 1.1	IB	21.3	−19.0	0.27 ± 0.02	74 ± 1	67 ± 5/6.9 ± 0.5	110 ± 8^{PV}	1	
5319	5.3 ± 0.6	SB(r)c	35.8	−19.7	0.77 ± 0.05	39 ± 4	47 ± 3/8.2 ± 0.6	180 ± 47	2	
5351	2.1 ± 0.6	SABa	19.3^{Sh}	−19.4	0.32 ± 0.04	71 ± 2	62 ± 3/5.8 ± 0.3	135 ± 8^{PV}	1	W^{N05}
5373	9.9 ± 0.3	IB	1.4^{Ka}	−14.3	0.62 ± 0.05	52 ± 4	148 ± 10/1.0 ± 0.1	90 ± 162	2	
5398	7.9 ± 3.8	Sd	3.8^{Ka}	−17.8	0.81 ± 0.08	36 ± 8	162 ± 13/3.0 ± 0.2			
IC 2542	4.6 ± 1.3	SBc	83.4	−20.5	0.75 ± 0.04	42 ± 4	31 ± 3/12.4 ± 1.2	290 ± 192	2	
5510	4.6 ± 1.0	SAB(r)c	18.6	−19.3	0.80 ± 0.05	37 ± 5	64 ± 6/5.8 ± 0.5	167 ± 44	1	
5532	3.9 ± 0.6	Sbc	41.1	−22.1	0.85 ± 0.08	32 ± 8	122 ± 10/24.2 ± 1.9	398 ± 24	1	W^{Web}
5556	5.0 ± 0.8	SBc pec	22.2	−18.9	0.32 ± 0.02	71 ± 1	67 ± 4/7.2 ± 0.4			W^{Web}
5786	4.0 ± 0.1	SAB(r)b	14.2^{Sh}	−19.6	0.96 ± 0.11	15 ± 23	54 ± 6/3.7 ± 0.4	80 ± 15	3	W^{Web}
5840	4.0 ± 0.3	SB(r)bc	6.9^{Ka}	−18.9	0.95 ± 0.07	17 ± 13	200 ± 10/6.7 ± 0.3*	251 ± 138	1	W^{Web}
5842	6.0 ± 0.4	SBc	15.2^{Sh}	−18.8	0.83 ± 0.05	34 ± 5	79 ± 5/5.8 ± 0.4	115 ± 18	2	
6118	2.1 ± 0.6	SB(r)ab	19.8^{Sh}	−20.0	0.90 ± 0.05	26 ± 7	74 ± 5/7.1 ± 0.4	137 ± 24	1	W^{N05}
6277	5.1 ± 0.5	SABc	16.9	−19.5	0.96 ± 0.07	17 ± 15	106 ± 9/8.7 ± 0.7	268 ± 257	2	V^{K00}
6419	8.9 ± 0.9	SBm	18.8	−18.6	0.65 ± 0.04	50 ± 3	44 ± 4/4.0 ± 0.4	53 ± 11	3	V^{W04}
6521	3.7 ± 0.9	S(r)bc	78.6	−21.2	0.67 ± 0.03	48 ± 2	50 ± 3/19.1 ± 1.2	249 ± 18	1	
6523	1.4 ± 1.1	Sa	80.0	−21.0	0.92 ± 0.04	23 ± 7	32 ± 3/12.5 ± 1.3	118 ± 63	4	
6787	1.7 ± 0.8	Sab	18.9	−20.5	0.60 ± 0.03	53 ± 2	104 ± 6/9.5 ± 0.5	232 ± 11	2	W^{N05}
7021	1.3 ± 0.8	SAB(r)a	26.8	−19.7	0.62 ± 0.04	52 ± 3	77 ± 5/10.0 ± 0.6	223 ± 18	1	
7045	5.3 ± 0.6	SABc	11.4^{Mo}	−19.2	0.39 ± 0.03	67 ± 2	124 ± 6/6.9 ± 0.3	160 ± 9	1	
7154	6.9 ± 0.4	SBcd	16.2	−20.0	0.46 ± 0.03	63 ± 2	139 ± 9/10.9 ± 0.7	145 ± 9	1	W^{Web}
7429	2.4 ± 0.7	SB(r)ab	23.7	−19.8	0.40 ± 0.03	67 ± 2	73 ± 5/8.4 ± 0.6			
7699	6.0 ± 0.6	SBc	9.3	−17.6	0.28 ± 0.01	74 ± 1	108 ± 6/4.9 ± 0.3	92 ± 8^{PV}	1	
7766	6.0 ± 0.4	SBc	13.0	−21.0	0.46 ± 0.05	63 ± 3	317 ± 15/20.0 ± 1.0*	120 ± 9	1	W^{Web}
7831	4.9 ± 0.4	SBc	5.2^{Ka}	−18.5	0.39 ± 0.03	67 ± 2	177 ± 8/4.5 ± 0.2	92 ± 15	2	W^{Web}
7853	8.6 ± 1.1	SBm	8.9^{Mo}	−18.9	0.64 ± 0.05	50 ± 3	106 ± 6/4.6 ± 0.3	110 ± 35	3	W^{Web}
7861	8.8 ± 0.7	SAB(r)m pec	10.2^{Mo}	−17.3	0.75 ± 0.05	41 ± 4	41 ± 4/2.0 ± 0.2	50 ± 21	3	W^{Web}
7876	6.5 ± 0.9	SABc	14.5	−17.9	0.72 ± 0.05	44 ± 4	58 ± 7/4.1 ± 0.5	98 ± 14	2	
7901	5.2 ± 0.6	Sc pec	20.7^{Sh}	−20.6	0.66 ± 0.03	49 ± 3	115 ± 6/11.6 ± 0.6	215 ± 10	1	
7985	6.9 ± 0.5	SBcd	13.7^{Mo}	−18.7	0.92 ± 0.08	23 ± 11	51 ± 5/3.4 ± 0.3	112 ± 13	1	
8334	4.0 ± 0.2	Sbc	9.8	−21.1	0.61 ± 0.06	53 ± 4	356 ± 20/16.9 ± 1.0	214 ± 9	1	
8403	5.8 ± 0.6	SBc	19.1^{Ja}	−19.2	0.61 ± 0.04	52 ± 3	90 ± 6/8.3 ± 0.6	128 ± 10	1	W^{Web}
NGC 5296	−1.1 ± 0.8	S0-a	32.8	−18.2	0.58 ± 0.04	54 ± 3	28 ± 3/4.5 ± 0.5	80 ± 9	3	W^{Web}
8709	4.9 ± 0.8	SABc pec	35.0	−21.4	0.24 ± 0.02	76 ± 1	112 ± 7/19.0 ± 1.1	207 ± 9	1	W^{Web}
8852	2.3 ± 0.6	SAB(r)a	30.6	−20.0	0.62 ± 0.08	52 ± 6	77 ± 9/11.4 ± 1.3	187 ± 10	3	
8863	1.1 ± 0.4	SBa	25.5^{Ko}	−20.3	0.39 ± 0.03	67 ± 2	108 ± 5/13.4 ± 0.6	193 ± 13	2	W^{N05}
8898	3.1 ± 0.6	SBb pec	49.0	−20.5	0.41 ± 0.03	66 ± 2	79 ± 6/18.7 ± 1.3	65 ± 45	4	W^{Web}
8900	3.2 ± 0.6	Sb pec	49.2	−21.7	0.47 ± 0.06	62 ± 4	75 ± 8/17.8 ± 1.8	346 ± 37	3	W^{Web}
8937	3.1 ± 0.4	SBb	49.0^{Mo}	−21.1	0.67 ± 0.06	48 ± 4	69 ± 6/16.4 ± 1.4	320 ± 105	1	
9013	6.0 ± 0.3	Sc pec	7.2^{Ka}	−18.2	0.66 ± 0.04	49 ± 3	72 ± 5/2.5 ± 0.2	62 ± 45	2	V^{R94}
9179	6.9 ± 0.4	SABc	5.7^{Ka}	−17.8	0.61 ± 0.03	52 ± 2	128 ± 8/3.5 ± 0.2	111 ± 36	3	
9219	9.7 ± 1.4	IB	10.2^{Ja}	−16.6	0.44 ± 0.03	64 ± 2	49 ± 4/2.4 ± 0.2	45 ± 8^{PV}	2	
9248	3.1 ± 0.5	Sb	54.9	−20.2	0.57 ± 0.03	55 ± 2	40 ± 4/10.6 ± 1.0	166 ± 11	1	

Table C3 – *continued*

N° UGC (1)	t (2)	Type (3)	D (Mpc) (4)	M_B (mag) (5)	b/a (6)	$i_{b/a}$ ($^\circ$) (7)	$D_{25}/2$ (arcsec kpc^{-1}) (8)	V_{max} flag (km s^{-1}) (9)	V_{max} (10)	H I data (11)
9358	3.3 ± 0.8	SABb	29.1	-20.8	0.52 ± 0.03	59 ± 2	$94 \pm 6/13.3 \pm 0.9$	221 ± 14	1	
9363	6.9 ± 0.4	S(r)cd	22.3	-19.8	0.84 ± 0.05	33 ± 6	$57 \pm 5/6.2 \pm 0.5$	143 ± 105	1	V[S96]
9406	6.9 ± 0.4	SB(r)cd	33.8	-19.0	0.64 ± 0.08	50 ± 6	$44 \pm 8/7.3 \pm 1.3$	19 ± 10	4	
9465	7.9 ± 0.9	SABd	26.4[Ja]	-18.0	0.40 ± 0.03	67 ± 2	$23 \pm 3/3.0 \pm 0.4$	97 ± 9	1	
9576	6.9 ± 0.4	SABc pec	27.4[Ja]	-19.6	0.63 ± 0.05	51 ± 4	$51 \pm 4/6.8 \pm 0.6$	104 ± 25	1	V[I94]
9736	5.0 ± 0.7	SABc	45.4	-20.6	0.65 ± 0.03	49 ± 2	$71 \pm 4/15.7 \pm 1.0$	193 ± 16	1	
9866	4.0 ± 0.3	S(r)bc	7.4[Ja]	-17.2	0.41 ± 0.03	65 ± 2	$55 \pm 4/2.0 \pm 0.1$	116 ± 11	2	
9943	5.0 ± 0.6	SB(r)c	28.0	-20.7	0.69 ± 0.05	46 ± 4	$82 \pm 5/11.1 \pm 0.7$	185 ± 10	1	
10075	6.0 ± 0.4	Sc	14.7[Ja]	-19.9	0.44 ± 0.04	64 ± 3	$174 \pm 9/12.4 \pm 0.7$	168 ± 9	1	
10521	4.9 ± 0.7	Sc	18.0[Mo]	-20.2	0.38 ± 0.03	68 ± 2	$106 \pm 9/9.3 \pm 0.7$	124 ± 9	1	
10652	3.8 ± 2.6	S(r)bc	18.2	-17.7	0.87 ± 0.05	29 ± 6	$33 \pm 3/2.9 \pm 0.3$	141 ± 82	2	
10713	3.0 ± 0.4	Sb	18.3	-19.0	0.19 ± 0.02	79 ± 1	$54 \pm 7/4.8 \pm 0.7$	105 ± 8[PV]	2	W[Web]
10757	6.0 ± 0.4	Sc	19.5	-17.7	0.53 ± 0.04	58 ± 2	$36 \pm 4/3.4 \pm 0.4$	81 ± 33	3	W[Web]
10769	3.0 ± 0.5	SABb	20.0	-17.0	0.59 ± 0.04	54 ± 3	$28 \pm 3/2.7 \pm 0.3$			W[Web]
10791	8.8 ± 0.5	SABm	21.7	-16.7	1.00 ± 0.13	0 ± 0	$56 \pm 9/5.9 \pm 0.9$	96 ± 49	3	W[Web]
11012	5.9 ± 0.7	Sc	5.3[Ka]	-18.7	0.33 ± 0.03	71 ± 2	$185 \pm 11/4.7 \pm 0.3$	117 ± 9	1	
11269	2.0 ± 0.5	SABa	35.0[Ja]	-19.9	0.56 ± 0.04	56 ± 3	$56 \pm 5/9.5 \pm 0.8$	202 ± 13	1	W[N05]
11300	6.4 ± 0.9	SABc	8.4[Ja]	-17.8	0.28 ± 0.01	74 ± 1	$99 \pm 5/4.0 \pm 0.2$	114 ± 9	2	W[Web]
11332	7.0 ± 0.5	SBcd	23.0[Ja]	-19.5	0.21 ± 0.01	78 ± 1	$63 \pm 5/7.1 \pm 0.5$	91 ± 8[PV]	3	
11407	3.6 ± 0.6	SBbc	35.8	-20.8	0.49 ± 0.03	61 ± 2	$75 \pm 6/13.0 \pm 1.0$	159 ± 31	1	V[W01]
11466	4.8 ± 1.9	Sc	14.2	-18.5	0.59 ± 0.03	54 ± 2	$45 \pm 4/3.1 \pm 0.3$	133 ± 10	1	W[Web]
11470	2.2 ± 0.6	Sab	50.8	-21.3	0.71 ± 0.07	45 ± 5	$72 \pm 9/17.8 \pm 2.2$	380 ± 40	2	
11496	8.8 ± 0.5	Sm	31.9		1.00 ± 0.13	0 ± 0	$57 \pm 9/8.9 \pm 1.3$	96 ± 29	2	W[Web]
11498	3.1 ± 0.7	SBb	44.9	-20.5	0.32 ± 0.04	71 ± 2	$84 \pm 9/18.2 \pm 1.9$	273 ± 9	1	
11597	5.9 ± 0.3	SABc	5.9[Ka]	-20.6	0.96 ± 0.09	16 ± 18	$342 \pm 14/9.8 \pm 0.4^*$	154 ± 32	3	
11670	0.5 ± 1.0	S(r)a	12.8	-19.4	0.33 ± 0.03	71 ± 2	$125 \pm 7/7.7 \pm 0.4$	190 ± 9	1	W[N05]
11872	2.5 ± 0.5	SAB(r)b	18.1[Ko]	-20.0	0.63 ± 0.07	51 ± 5	$85 \pm 6/7.4 \pm 0.5$	183 ± 12	1	
12082	8.7 ± 0.8	SABm	10.1[Ja]	-16.4	0.90 ± 0.07	26 ± 10	$81 \pm 9/3.9 \pm 0.4$	105 ± 137	3	W[Web]

Column (1): name of the galaxy in the UGC catalogue (see Table C1). Column (2): morphological type from the de Vaucouleurs classification (de Vaucouleurs 1979) in the HyperLeda data base. Column (3): morphological type from the HyperLeda data base. Column (4): distance D, deduced from the systemic velocity taken in NED corrected from Virgo infall, assuming $H_0 = 75$ km s^{-1} Mpc^{-1}, except for those marked (*Ja*: James et al. 2004; *Ka*: Karachentsev et al. 2004; *Ko*: Koopmann, Haynes & Catinella 2006; *Mo*: Moustakas & Kennicutt 2006; *Oc*: O'Connell, Gallagher & Hunter 1994; *Sh*: Shapley, Fabbiano & Eskridge 2001). Column (5): absolute B magnitude from D and apparent corrected B magnitude (HyperLeda). Column (6): axial ratio from HyperLeda. Column (7): inclination derived from the axial ratio (arccos b/a). Column (8): isophotal radius at the limiting surface brightness of 25 B mag arcsec^{-2}, from HyperLeda (Paturel et al. 1991) in arcsecond and kpc adopting the distance given in column (4); an asterisk (*) indicates that the galaxy is larger than GHASP field-of-view. Column (9): maximum velocity, V_{max}, derived from the fit of the velocity field discussed in Section 3.2, or from the position–velocity diagram (marked with[PV]). Column (10): quality flag on V_{max} (1: reached; 2: probably reached; 3 probably not reached; 4: not reached). Column (11): aperture synthesis H I data references: W for WHISP data (*S02*: Swaters et al. 2002; *N05*: Noordermeer et al. 2005; *web*: http://www.astro.rug.nl/ whisp); V for VLA data (*I94*: Irwin 1994; *R94*: Rownd et al. 1994; *S96*: Schulman et al. 1996; *K00*: Kornreich et al. 2000; *W01*: Wilcots et al. 2001; *W04*: Wilcots & Prescott 2004).
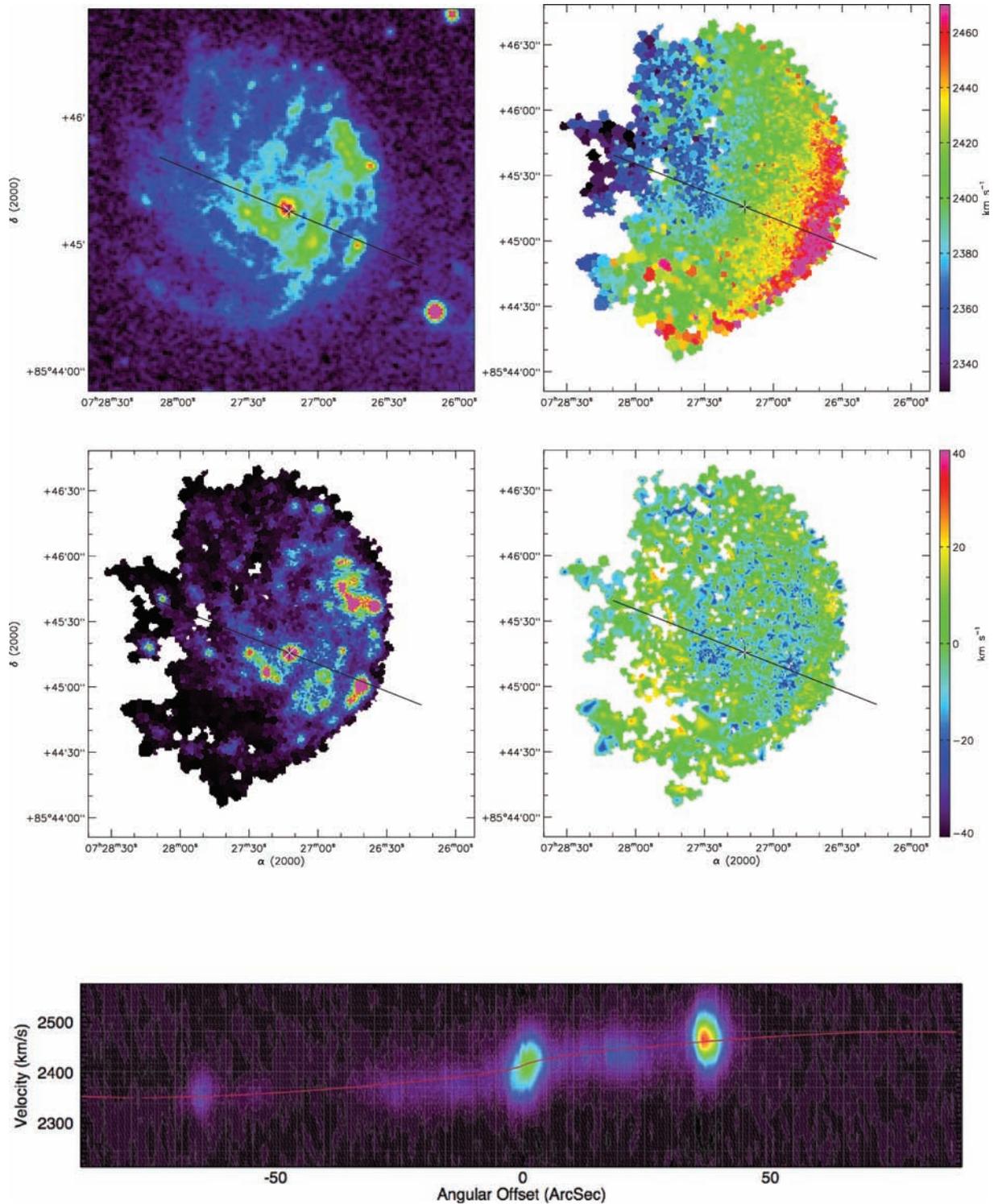
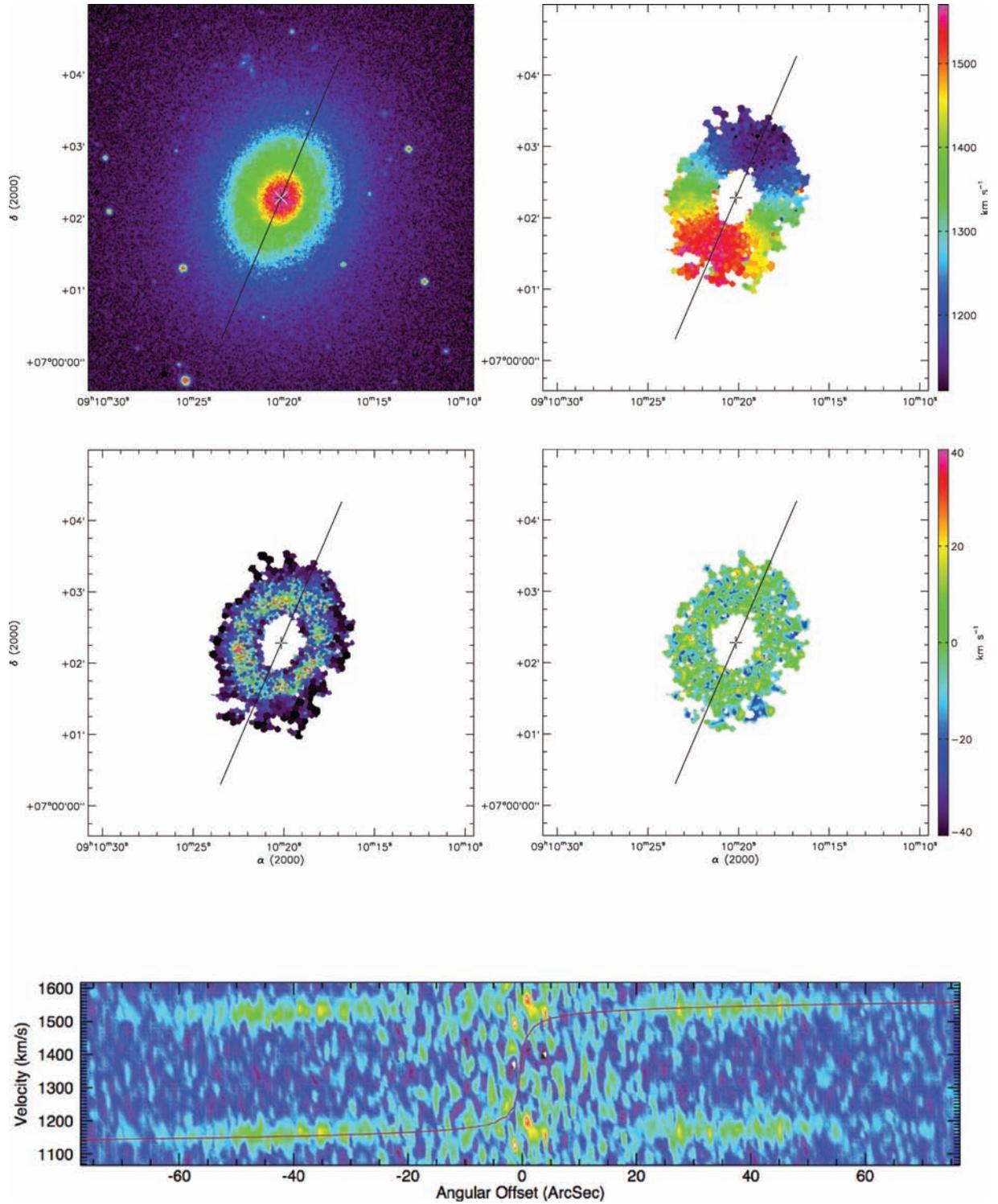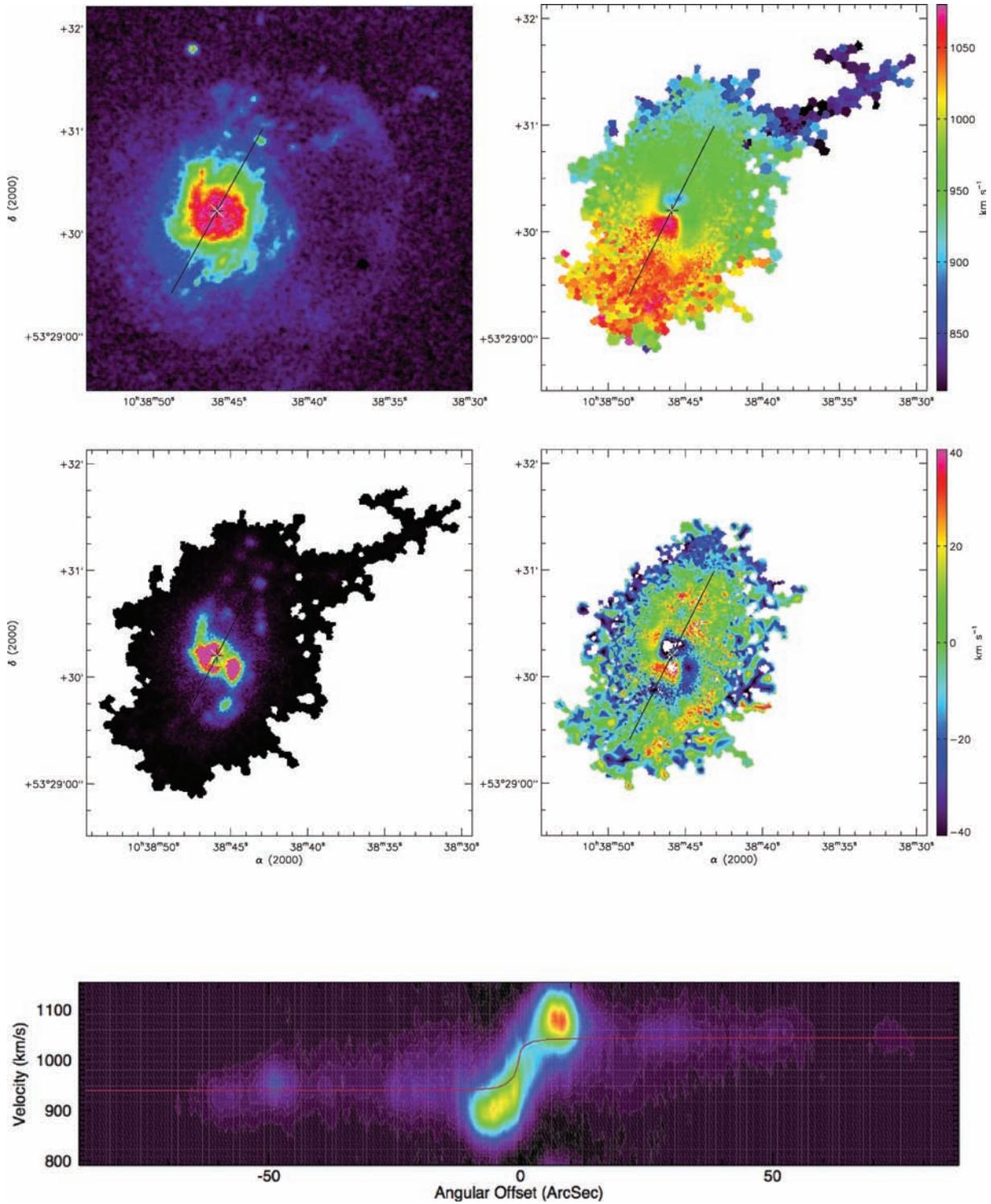## APPENDIX D: INDIVIDUAL MAPS AND
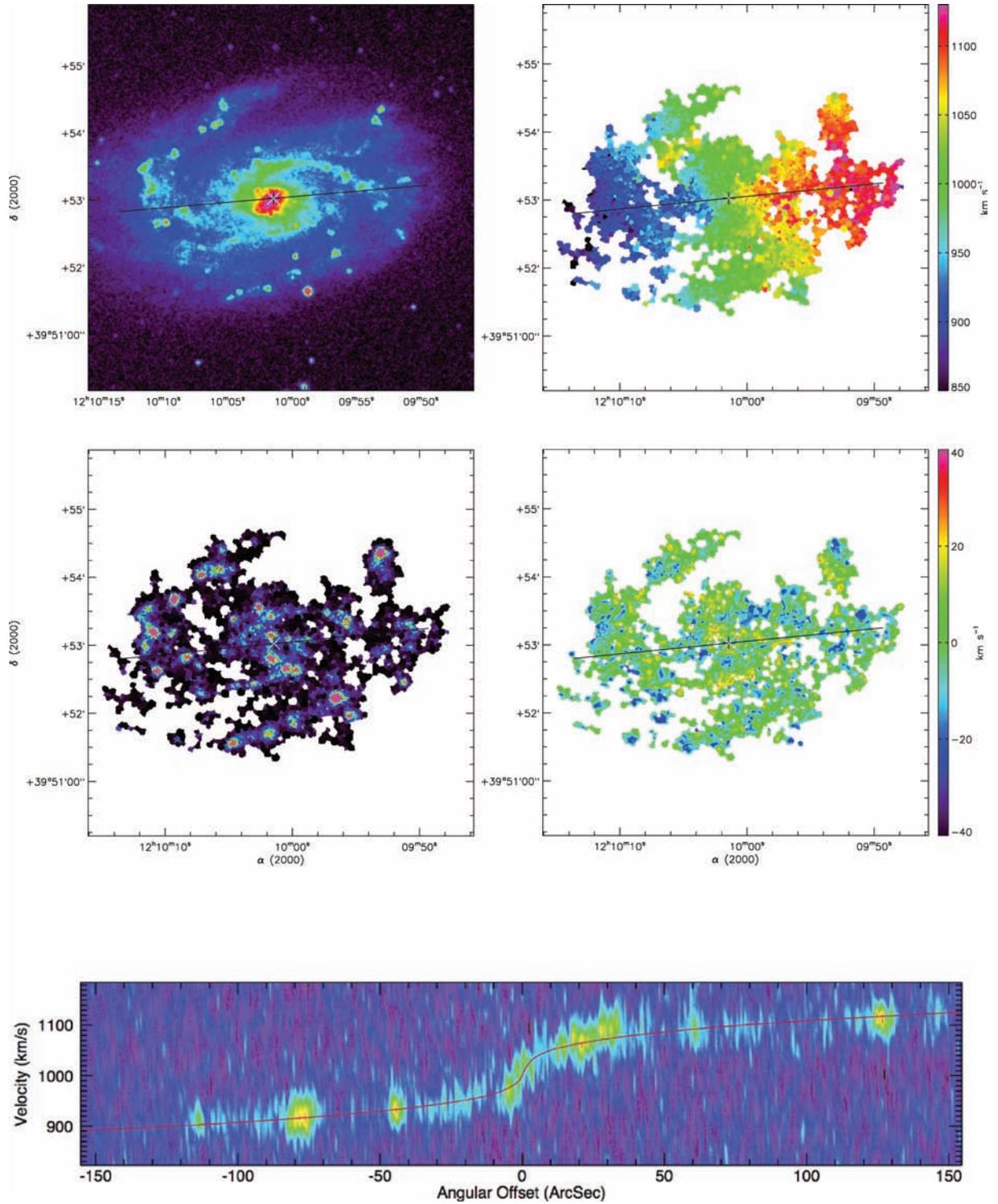## POSITION–VELOCITY DIAGRAMS

Figure D19. UGC 3740. Top left-hand panel: XDSS blue-band image. Top right-hand panel: Hα velocity field. Middle left-hand panel: Hα monochromatic image. Middle right-hand panel: Hα residual velocity field. The white and black cross is the kinematical centre. The black line is the major-axis, its length represents D_{25}. Bottom panel: position–velocity diagram along the major-axis (full width of 7 pixels), arbitrary flux units. The red line plots the rotation curve computed from the model velocity field along the major-axis (full width of 7 pixels).

**Figure D31.** UGC 4820. Top left-hand panel: XDSS blue-band image. Top right-hand panel: Hα velocity field. Middle left-hand panel: Hα monochromatic image. Middle right-hand panel: Hα residual velocity field. The white and black cross is the kinematical centre. The black line is the major-axis, its length represents D_{25}. Bottom panel: position–velocity diagram along the major-axis (full width of 7 pixels), arbitrary flux units. The red line plots the rotation curve computed from the model velocity field along the major-axis (full width of 7 pixel).

Figure D45. UGC 5786. Top left-hand panel: XDSS blue-band image. Top right-hand panel: Hα velocity field. Middle left-hand panel: Hα monochromatic image. Middle right-hand panel: Hα residual velocity field. The white and black cross is the kinematical centre. The black line is the major-axis, its length represents D_{25}. Bottom panel: position–velocity diagram along the major-axis (full width of 7 pixels), arbitrary flux units. The red line plots the rotation curve computed from the model velocity field along the major-axis (full width of 7 pixel).

Figure D56. UGC 7154. Top left-hand panel: XDSS blue-band image. Top right-hand panel: Hα velocity field. Middle left-hand panel: Hα monochromatic image. Middle right-hand panel: Hα residual velocity field. The white and black cross is the kinematical centre. The black line is the major-axis, its length represents D_{25}. Bottom panel: position–velocity diagram along the major-axis (full width of 7 pixels), arbitrary flux units. The red line plots the rotation curve computed from the model velocity field along the major-axis (full width of 7 pixel).

APPENDIX E: ROTATION CURVES
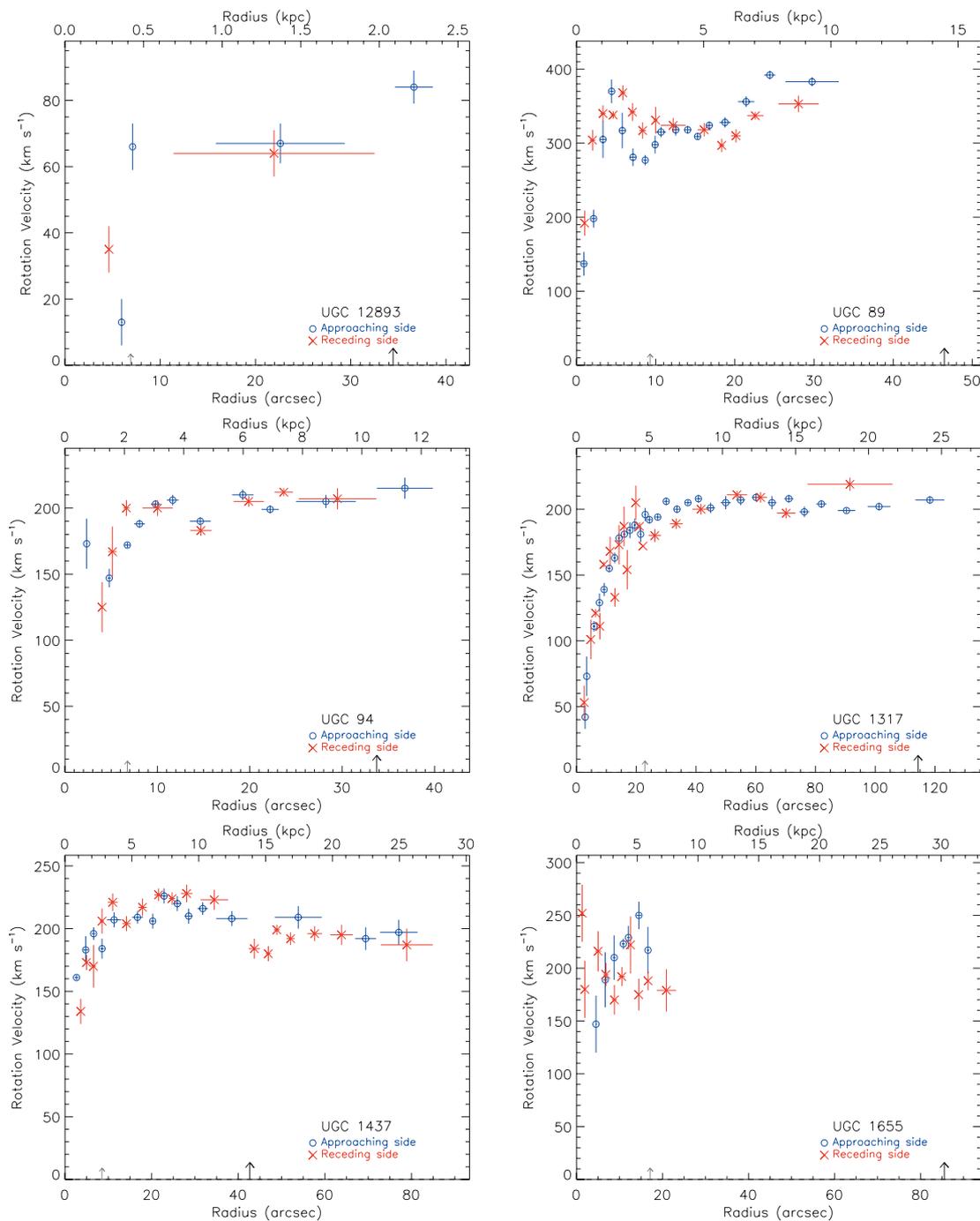
Figure E1. From the top left-hand panel to the bottom right-hand panel: Hα rotation curve of UGC 12893, UGC 89, UGC 94, UGC 1317, UGC 1437 and UGC 1655.
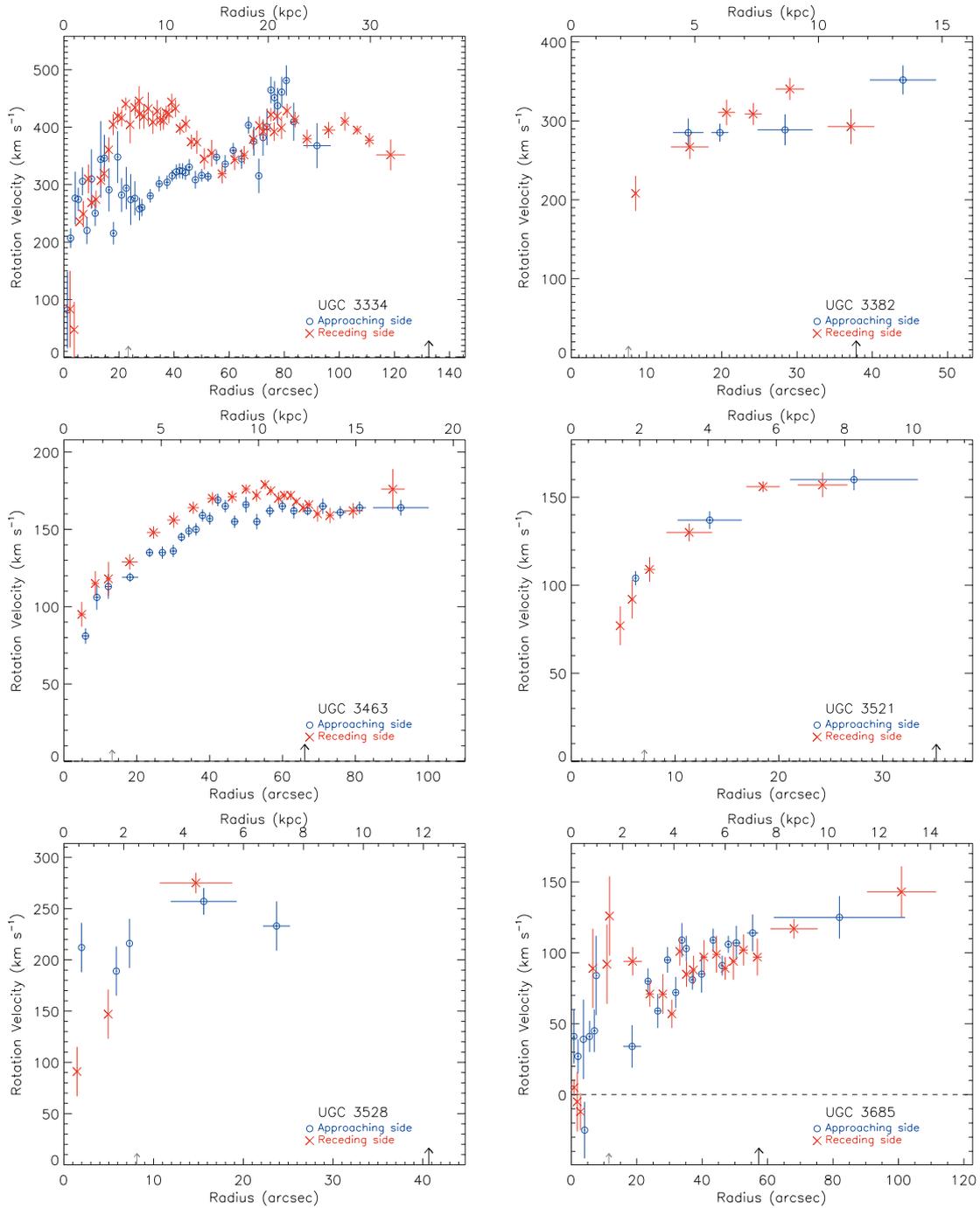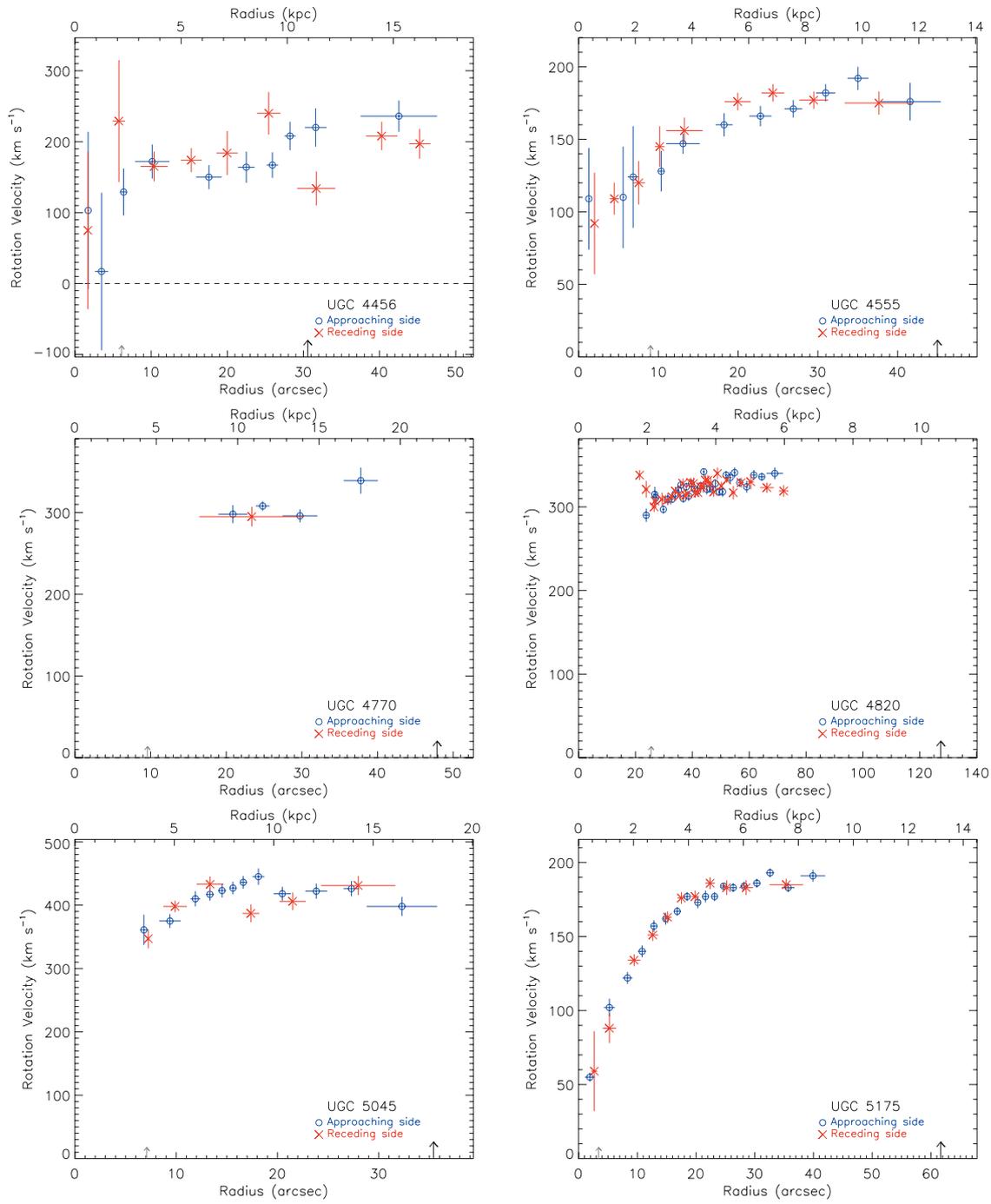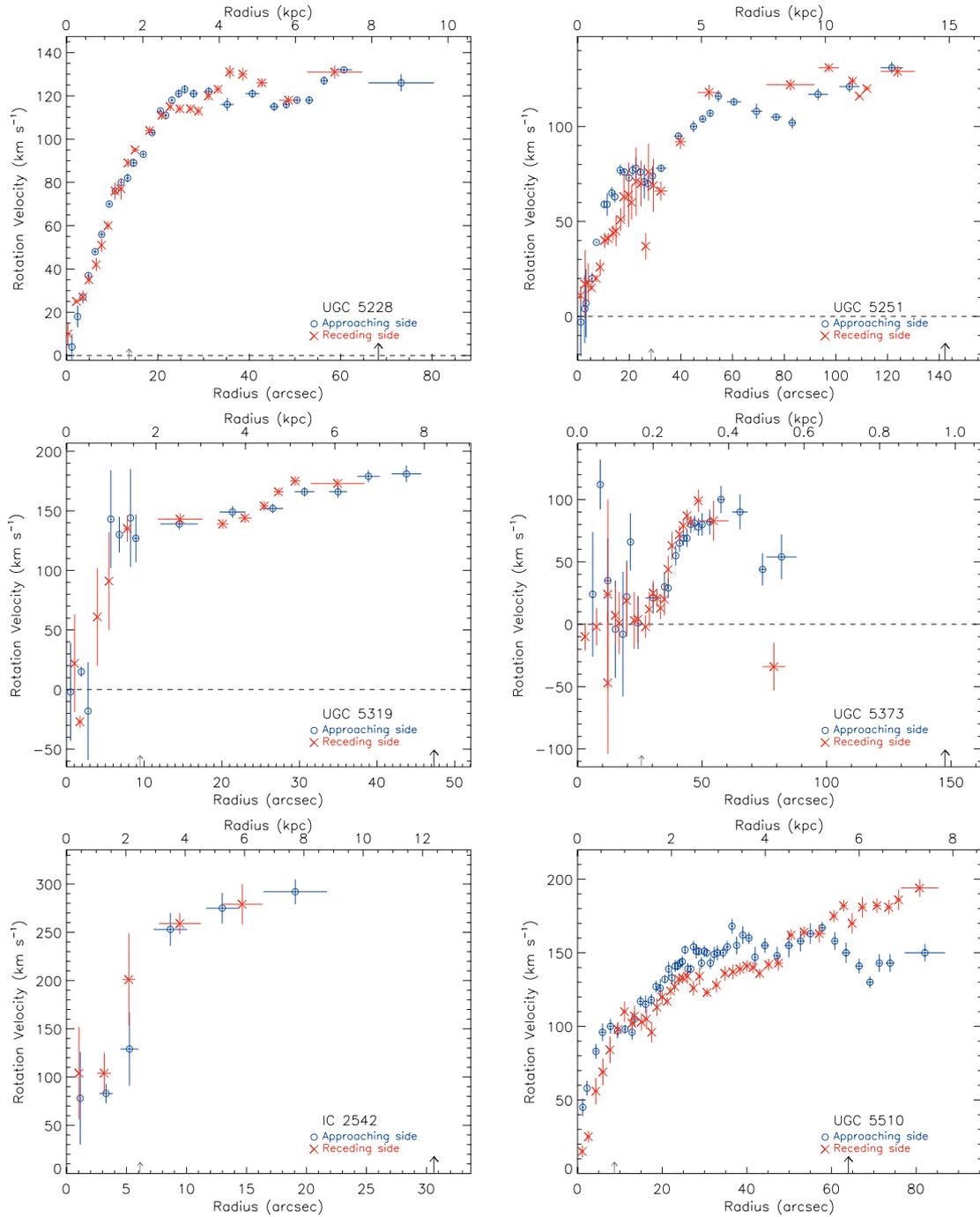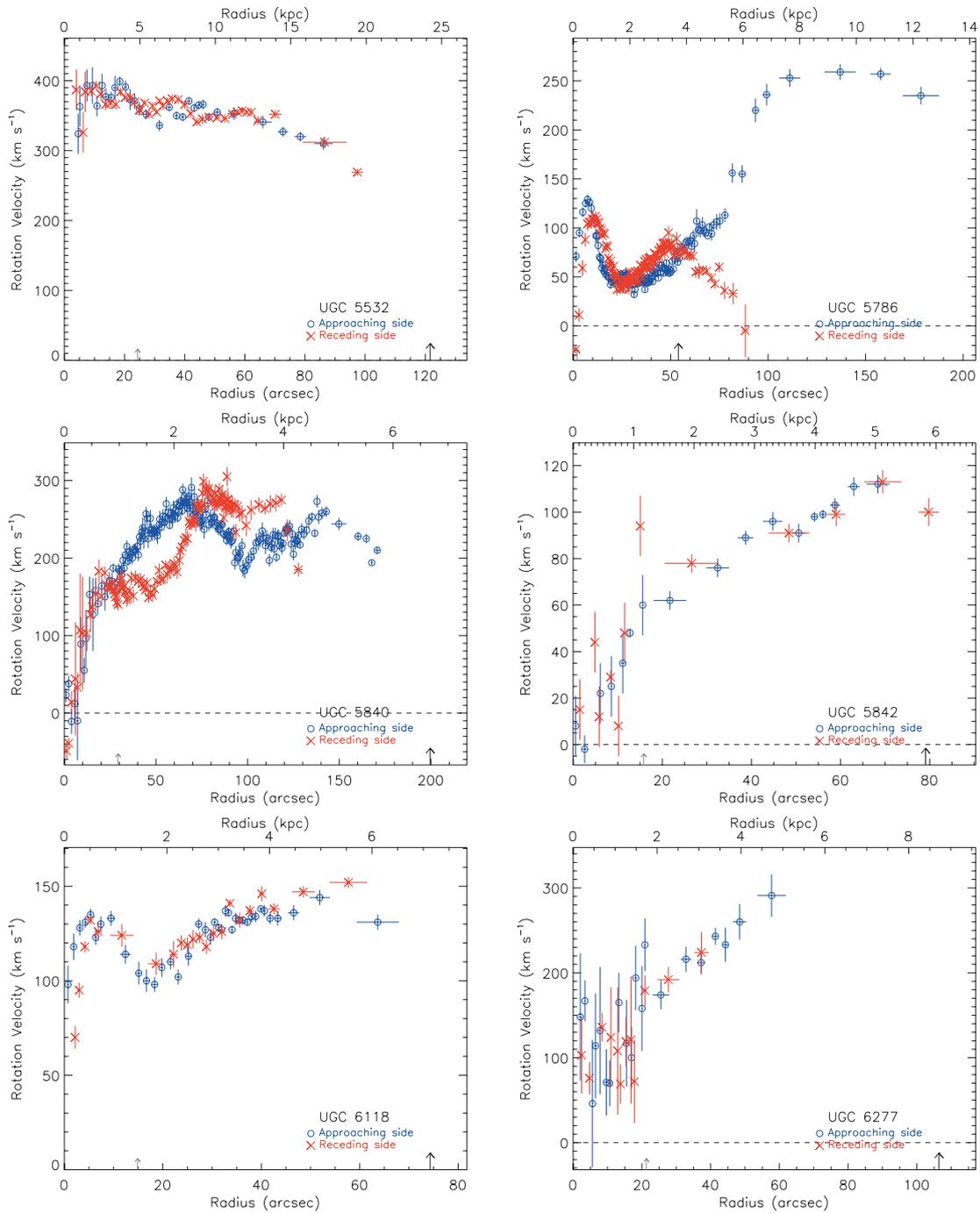
Figure E2. From the top left-hand panel to the bottom right-hand panel: Hα rotation curve of UGC 3334, UGC 3382, UGC 3463, UGC 3521, UGC 3528 and UGC 3685.
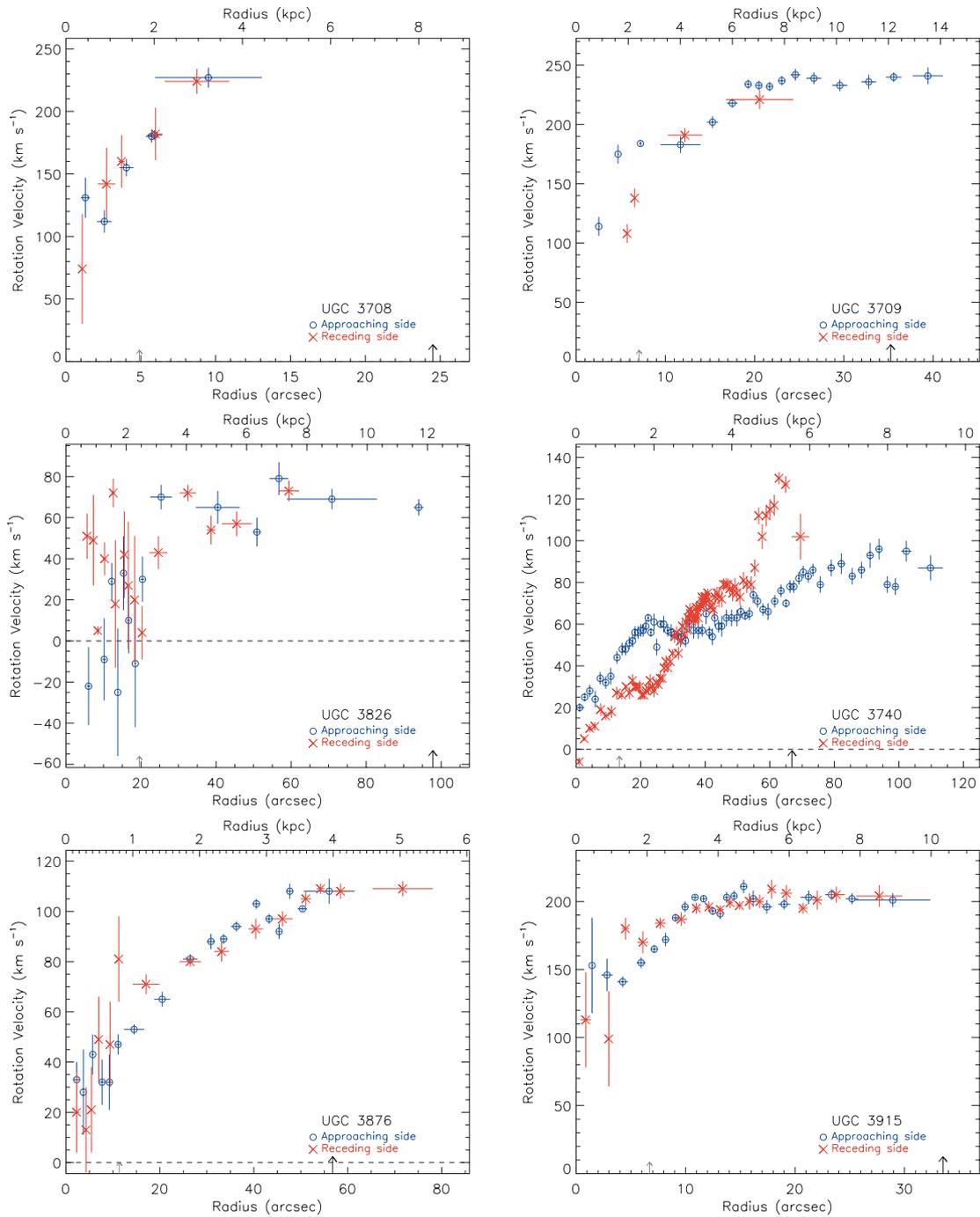
Figure E3. From the top left-hand panel to the bottom right-hand panel: Hα rotation curve of UGC 3708, UGC 3709, UGC 3826, UGC 3740, UGC 3876 and UGC 3915.
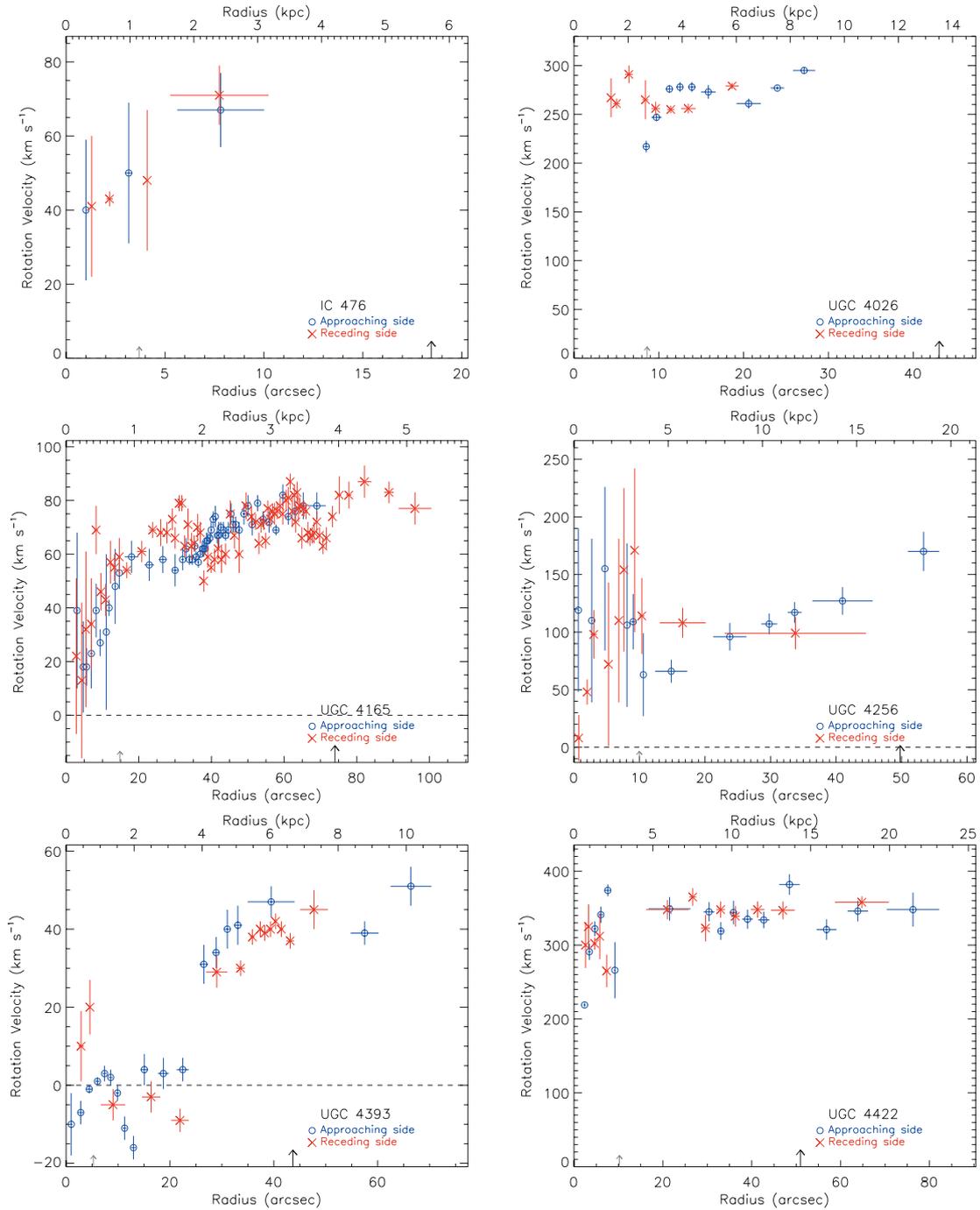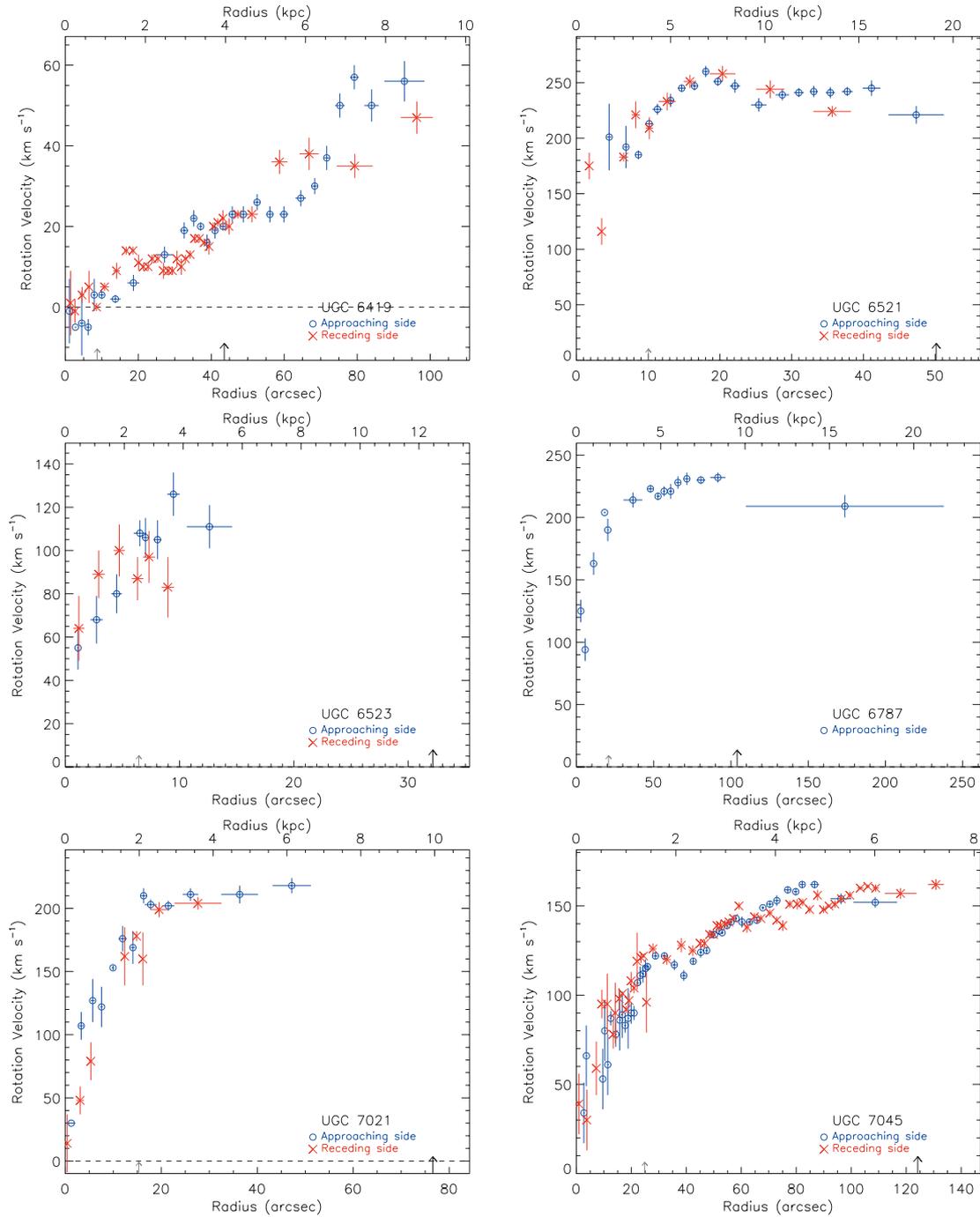
Figure E4. From the top left-hand panel to the bottom right-hand panel: Hα rotation curve of IC 476, UGC 4026, UGC 4165, UGC 4256, UGC 4393 and UGC 4422.

Figure E5. From the top left-hand panel to the bottom right-hand panel: Hα rotation curve of UGC 4456, UGC 4555, UGC 4770, UGC 4820, UGC 5045 and UGC 5175.

Figure E6. From the top left-hand panel to the bottom right-hand panel: Hα rotation curve of UGC 5228, UGC 5251, UGC 5319, UGC 5373, IC 2542 and UGC 5510.

Figure E7. From the top left-hand panel to the bottom right-hand panel: Hα rotation curve of UGC 5532, UGC 5786, UGC 5840, UGC 5842, UGC 6118 and UGC 6277.

Figure E8. From the top left-hand panel to the bottom right-hand panel: Hα rotation curve of UGC 6419, UGC 6521, UGC 6523, UGC 6787, UGC 7021 and UGC 7045.
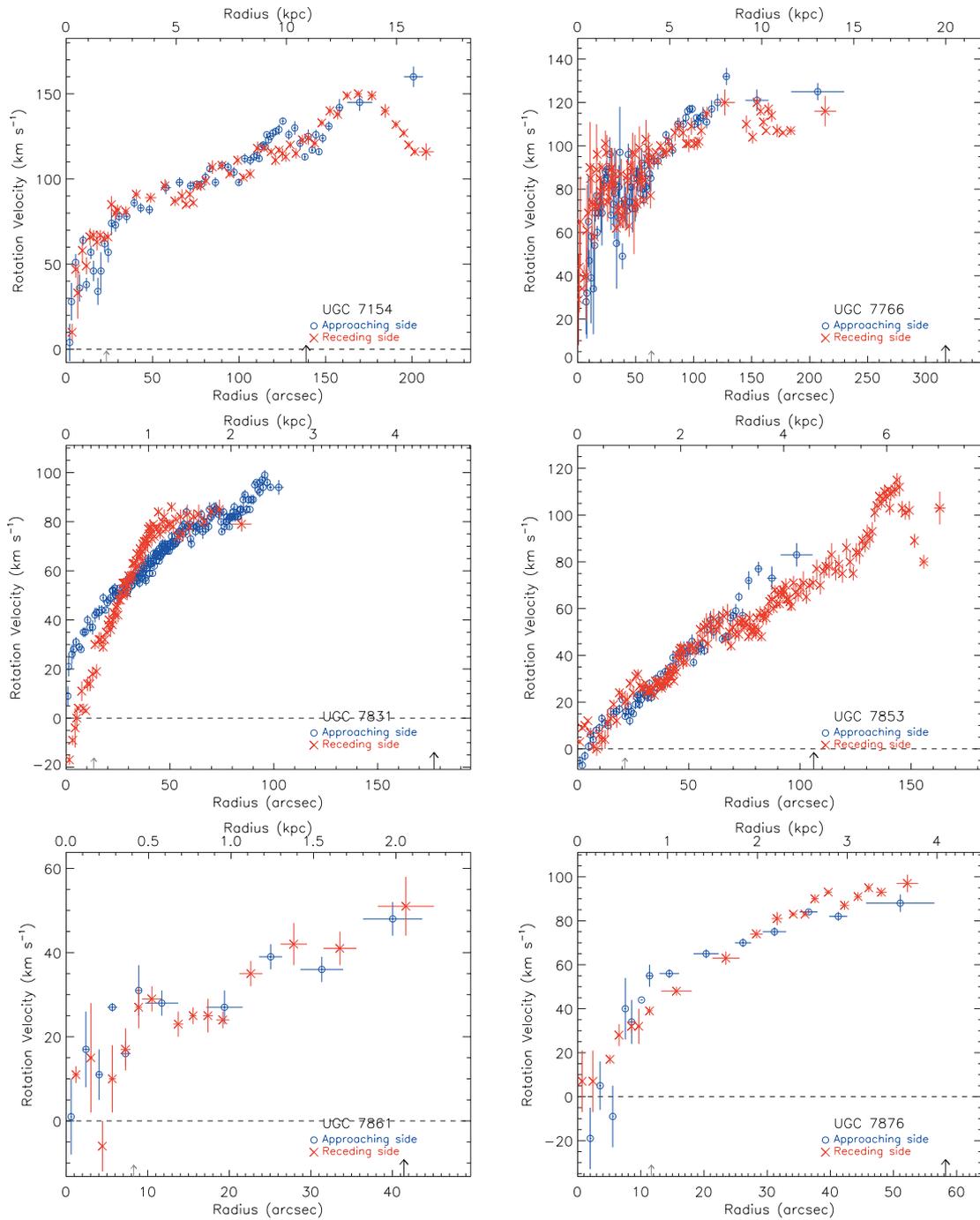
Figure E9. From the top left-hand panel to the bottom right-hand panel: Hα rotation curve of UGC 7154, UGC 7766, UGC 7831, UGC 7853, UGC 7861 and UGC 7876.
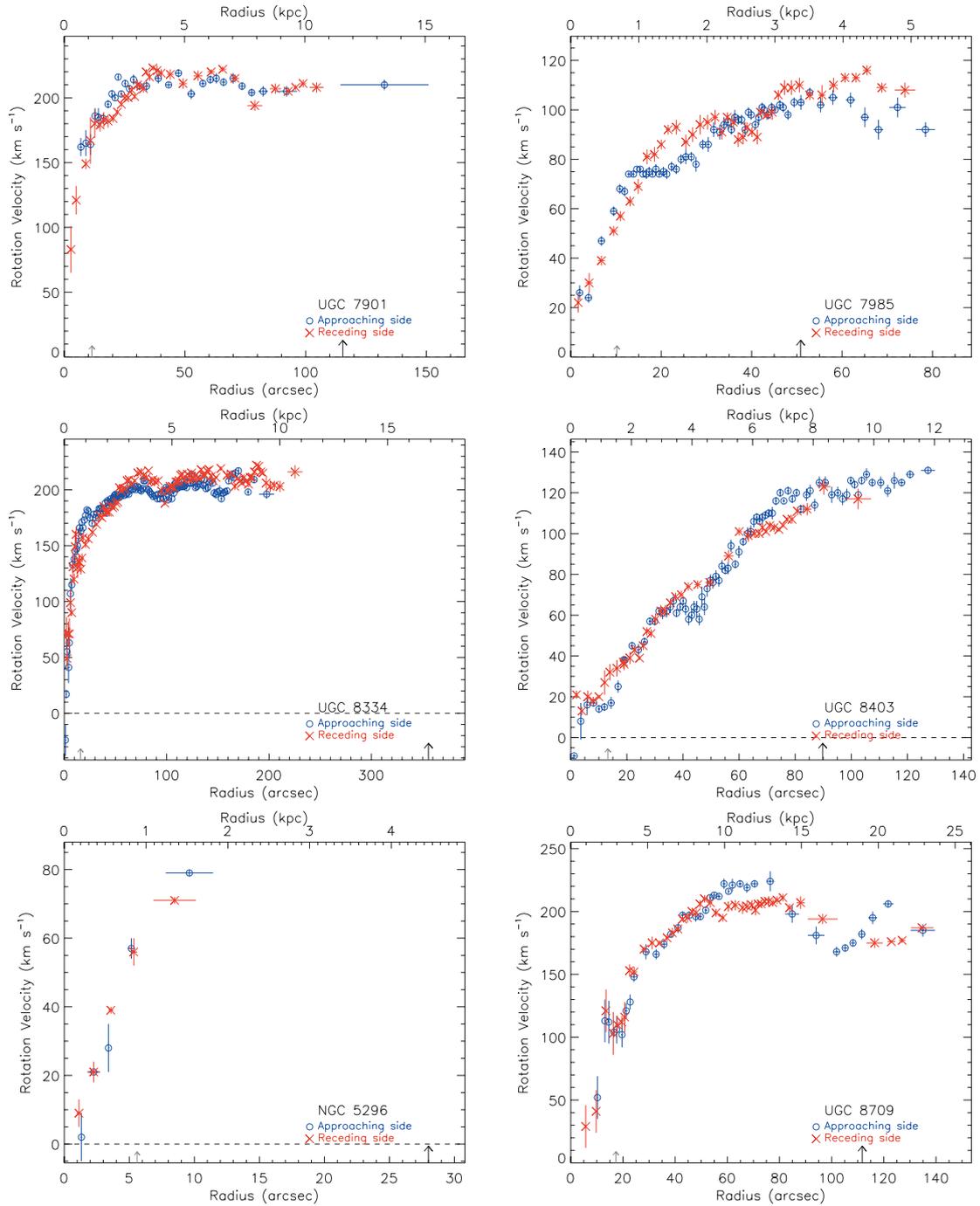
Figure E10. From the top left-hand panel to the bottom right-hand panel: Hα rotation curve of UGC 7901, UGC 7985, UGC 8334, UGC 8403, NGC 5296 and UGC 8709.
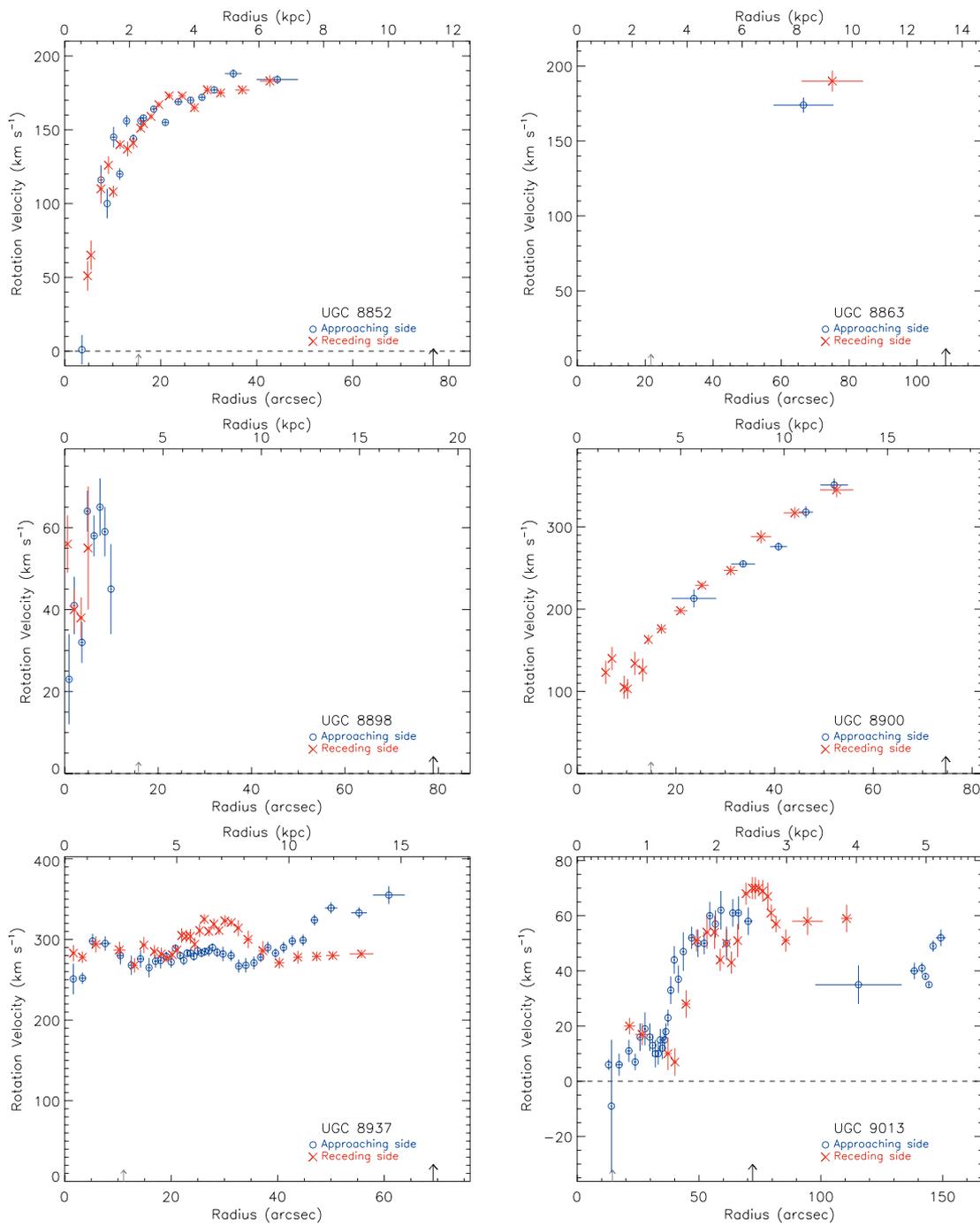
Figure E11. From the top left-hand panel to the bottom right-hand panel: Hα rotation curve of UGC 8852, UGC 8863, UGC 8898, UGC 8900, UGC 8937 and UGC 9013.
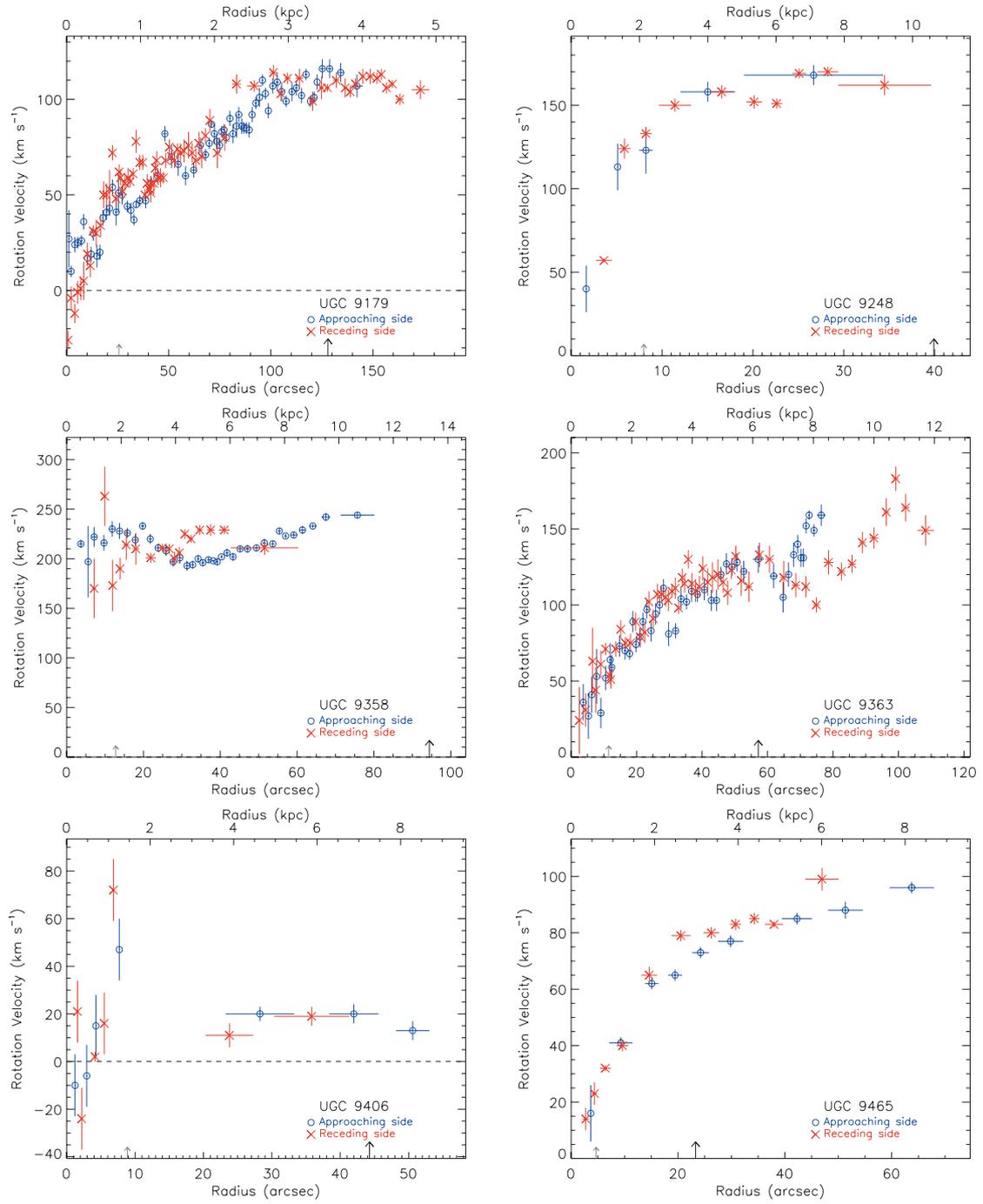
Figure E12. From the top left-hand panel to the bottom right-hand panel: Hα rotation curve of UGC 9179, UGC 9248, UGC 9358, UGC 9363, UGC 9406 and UGC 9465.
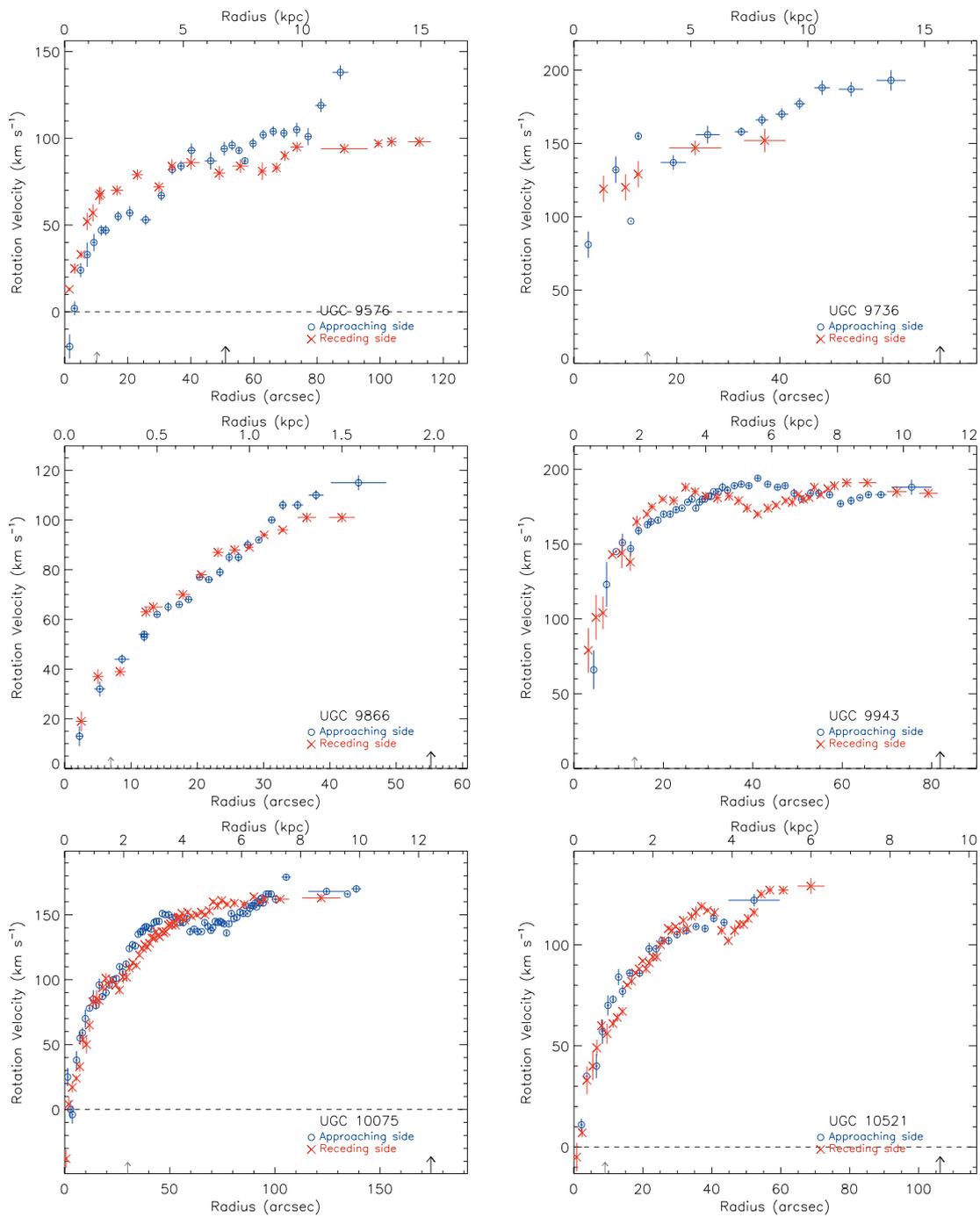
Figure E13. From the top left-hand panel to the bottom right-hand panel: Hα rotation curve of UGC 9576, UGC 9736, UGC 9866, UGC 9943, UGC 10075 and UGC 10521.
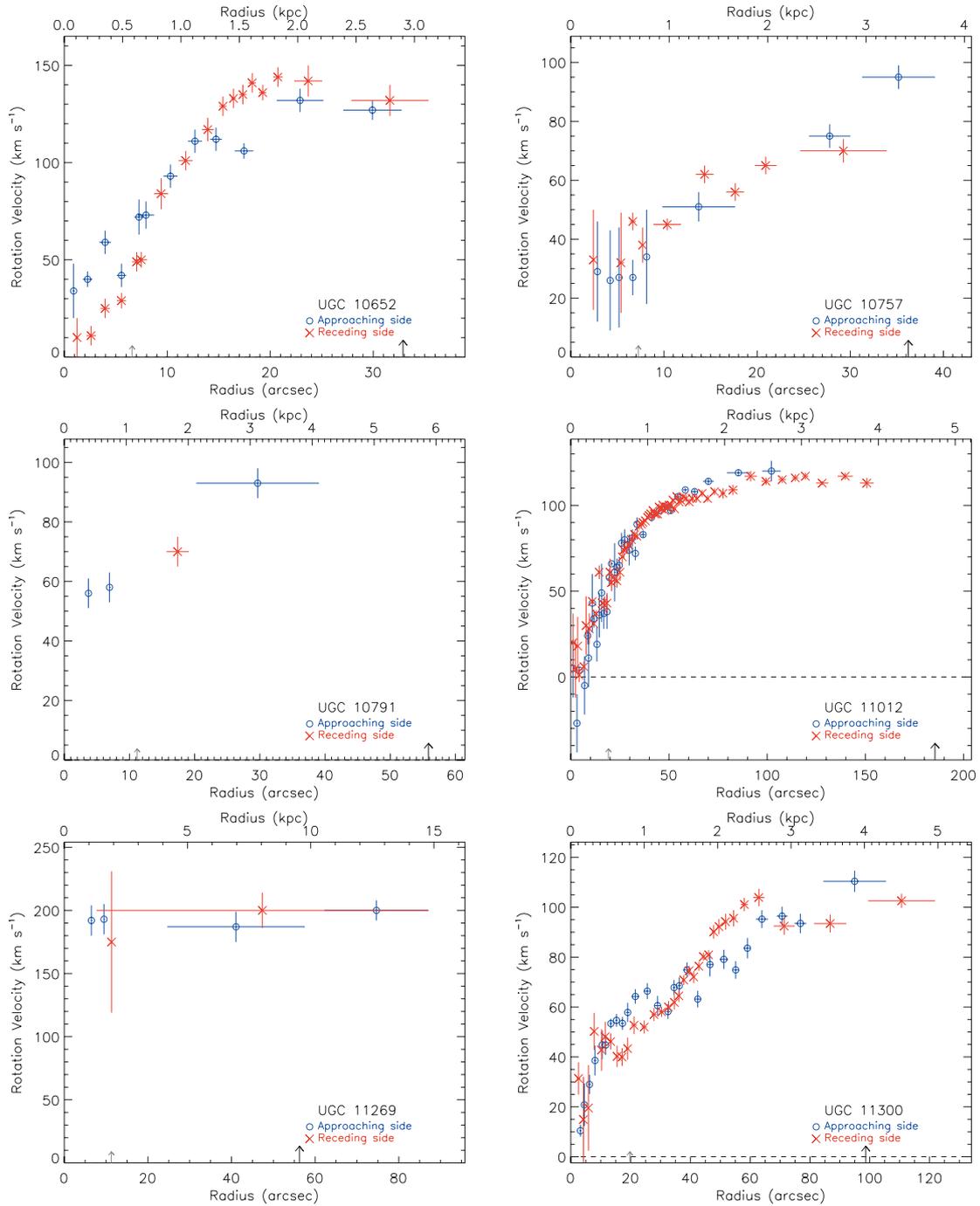
Figure E14. From the top left-hand panel to the bottom right-hand panel: Hα rotation curve of UGC 10652, UGC 10757, UGC 10791, UGC 11012, UGC 11269 and UGC 11300.
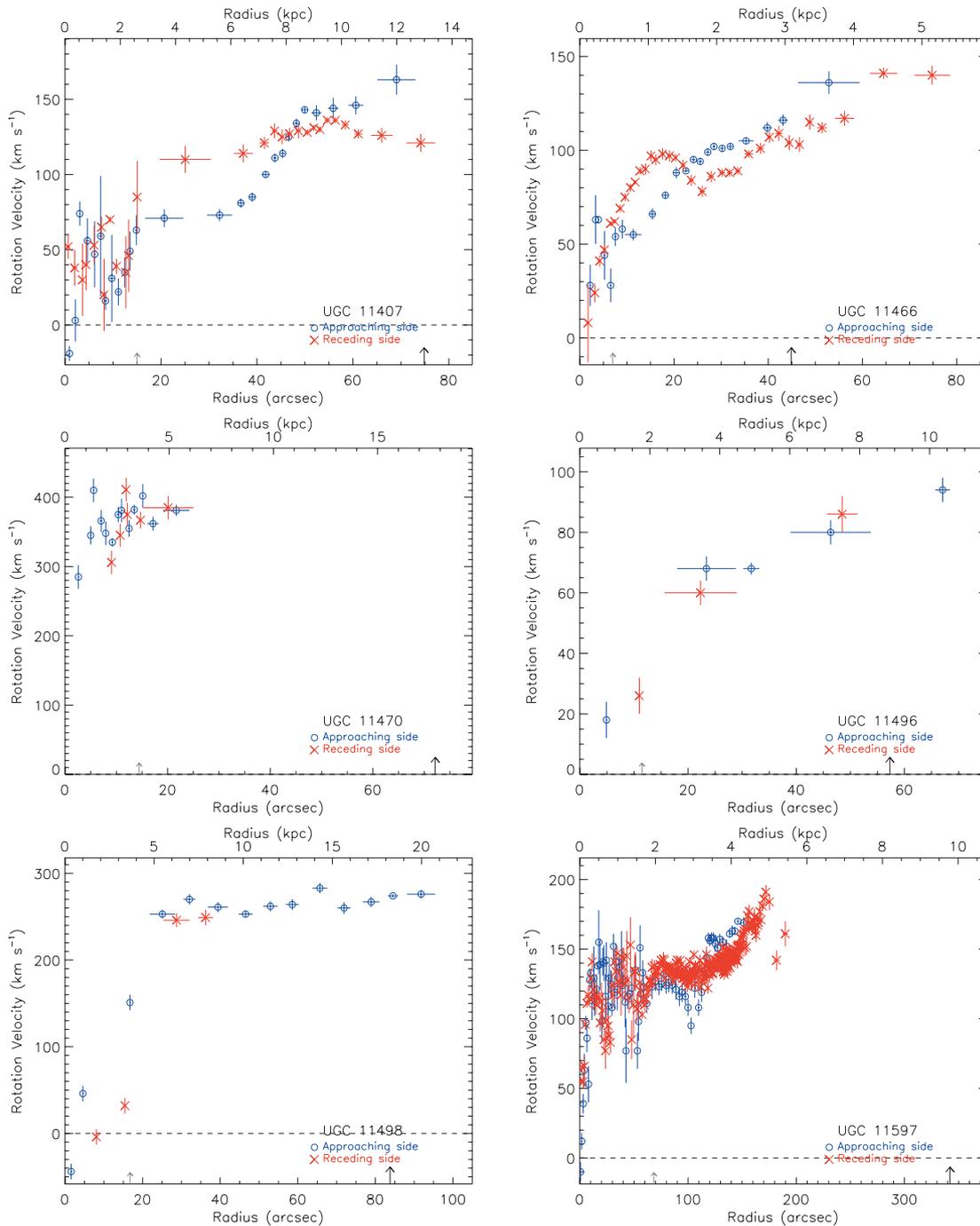
Figure E15. From the top left-hand panel to the bottom right-hand panel: Hα rotation curve of UGC 11407, UGC 11466, UGC 11470, UGC 11496, UGC 11498 and UGC 11597.
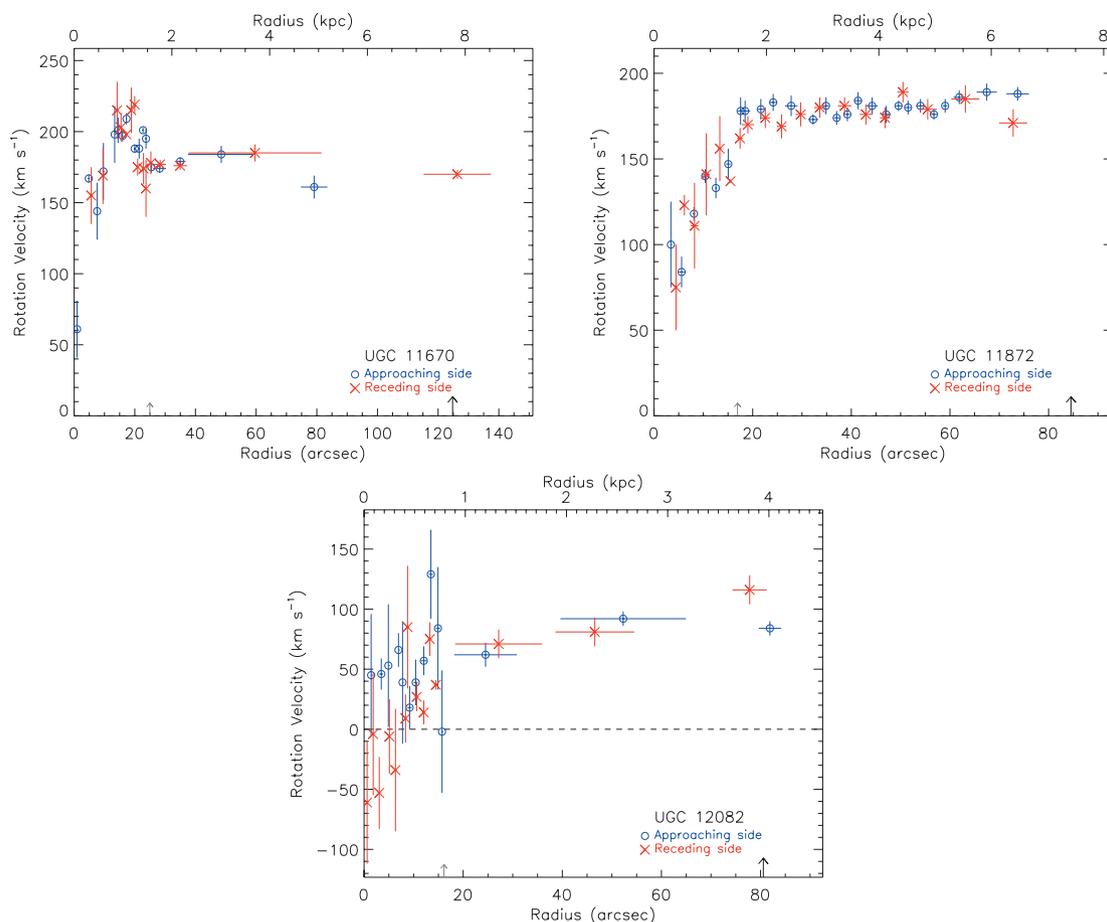
Figure E16. From the top left-hand panel to the bottom right-hand panel: Hα rotation curve of UGC 11670, UGC 11872 and UGC 12082.

APPENDIX F: ROTATION CURVE TABLES

Table F1. UGC 12893 rotation curve.

r (kpc) (1)	σ_r (kpc) (2)	r (arcsec) (3)	σ_r (arcsec) (4)	v (km s^{-1}) (5)	σ_v (km s^{-1}) (6)	N bins (7)	Side (8)
0.28	0.00	4.6	0.0	35	7	1	r
0.36	0.00	5.9	0.0	13	7	1	a
0.43	0.00	7.1	0.0	66	7	1	a
1.33	0.64	21.9	10.6	64	7	22	r
1.37	0.41	22.6	6.8	67	6	22	a
2.22	0.12	36.6	2.0	84	5	9	a

Columns (1) and (3): Galactic radius. Columns (2) and (4): dispersion around the galactic radius. Column (5): rotation velocity. Column (6): dispersion in the rotation velocity. Column (7): number of velocity bins. Column (8): receding – *r* – or approaching – *a* – side.

Table F2. UGC 89 rotation curve.

r (kpc)	σ_r (kpc)	r (arcsec)	σ_r (arcsec)	v (km s^{-1})	σ_v (km s^{-1})	N bins	Side
(1)	(2)	(3)	(4)	(5)	(6)	(7)	(8)
0.29	0.10	0.9	0.3	137	16	4	a
0.32	0.03	1.0	0.1	192	17	2	r
0.63	0.11	2.0	0.4	304	14	11	r
0.67	0.09	2.2	0.3	198	12	5	a
1.04	0.13	3.3	0.4	305	25	11	a
1.04	0.11	3.3	0.4	340	11	14	r
1.38	0.09	4.4	0.3	370	16	7	a
1.44	0.11	4.6	0.4	338	5	13	r
1.80	0.12	5.8	0.4	317	24	8	a
1.82	0.11	5.8	0.4	368	10	8	r
2.20	0.11	7.1	0.4	342	12	7	r
2.22	0.11	7.1	0.4	281	12	9	a
2.60	0.13	8.4	0.4	317	11	3	r
2.70	0.09	8.7	0.3	277	7	11	a
3.09	0.11	9.9	0.4	298	12	10	a
3.11	0.08	10.0	0.3	331	18	5	r
3.32	0.20	10.7	0.6	315	7	23	a
3.80	0.49	12.2	1.6	324	10	23	r
3.90	0.15	12.5	0.5	318	8	23	a
4.37	0.13	14.0	0.4	318	5	23	a
4.76	0.11	15.3	0.4	309	4	23	a
5.02	0.26	16.1	0.8	318	9	23	r
5.22	0.14	16.8	0.4	324	5	23	a
5.71	0.11	18.3	0.4	297	9	23	r
5.84	0.22	18.8	0.7	328	7	23	a
6.27	0.19	20.1	0.6	310	9	23	r
6.67	0.32	21.4	1.0	356	7	23	a
7.03	0.32	22.6	1.0	337	5	23	r
7.60	0.22	24.4	0.7	392	6	23	a
8.73	0.79	28.0	2.5	353	11	20	r
9.26	1.05	29.8	3.4	383	6	23	a

Columns (1) and (3): Galactic radius. Columns (2) and (4): dispersion around the galactic radius. Column (5): rotation velocity. Column (6): dispersion in the rotation velocity. Column (7): number of velocity bins. Column (8): receding – r – or approaching – a – side.

SUPPLEMENTARY MATERIAL

The following supplementary material is available for this article:

Appendix D. Individual maps and position–velocity diagrams.

Appendix F. Rotation curve tables.

This material is available as part of the online article from: http://www.blackwell-synergy.com/doi/abs/10.1111/j.1365-2966.2008.13422.x
(this link will take you to the article abstract).

Please note: Blackwell Publishing are not responsible for the content or functionality of any supplementary materials supplied by the authors. Any queries (other than missing material) should be directed to the corresponding author for the article.

This paper has been typeset from a TEX/LATEX file prepared by the author.